



# Recent advances in NMR crystallography and polymorphism

**Scott A. Southern and David L. Bryce**

Department of Chemistry and Biomolecular Sciences, University of Ottawa, Ottawa, ON, Canada

## Contents

1. Introduction	2
2. Theory	3
2.1 NMR interactions	3
2.2 Methodology	5
3. NMR crystallography and polymorphism	9
3.1 Polymorphism	9
3.2 Probing non-covalent bonding in solids	30
3.3 Dynamic processes	33
3.4 <sup>1</sup> H spin-lattice relaxation measurements	42
3.5 Sensitivity enhancement by paramagnetism	46
3.6 Dynamic nuclear polarization	47
3.7 Nuclear quadrupole resonance spectroscopy (NQR)	51
3.8 Crystal structure prediction	53
4. Concluding remarks	62
Acknowledgements	62
References	62

## Abstract

This chapter covers some recent developments in NMR crystallography with a focus on its application towards the identification and characterization of crystal structures and their polymorphs. NMR crystallography is a discipline that uses insights or constraints obtained from solid-state NMR spectroscopy and first-principles calculations to predict, identify, validate, or refine crystal structures. In recent years, there have been plenty of developments in the area of NMR crystallography as it applies to study polymorphism in organic and inorganic systems, the understanding of noncovalent bonding networks directing crystal growth, and the study of dynamic processes present within solids. We discuss these topics through the lens of solid-state NMR and consider some of the more innovative or unusual strategies being applied to these problems, such as

dynamic nuclear polarization (DNP) or nuclear quadrupole resonance (NQR) spectroscopy. The focus is on literature reports from 2016 to mid-2020.

**Keywords:** Solid-state NMR, Polymorphism, NMR crystallography, *In situ*, Non-covalent bonding, Dynamics, Nuclear quadrupole resonance spectroscopy



## 1. Introduction

Solid-state nuclear magnetic resonance (NMR) has long played a vital role in the characterization of solid materials. Solid-state NMR is suitable for many systems because it is non-invasive, and the required equipment is widely available. It can probe nuclei of interest, whose spectral responses are sensitive to even the most subtle changes in their local electronic environments.

Solid-state NMR can provide information about chemical bonds or help to characterize the chemical structure of a molecule or a complex system such as a protein. It may also provide new insights into the mechanisms of catalysis and biochemical reactions [1–4], or the formation of supramolecular structures such as zeolites or metal-organic frameworks (MOFs). However, NMR alone is not necessarily sufficient for studying such systems. The field of NMR crystallography employs various approaches for the study of crystal structures to either determine, validate, or select crystal structures and their polymorphs. Examples of this are crystal structure prediction or determination, or the validation of structural properties based on NMR data. In this context, NMR crystallography usually relies on the complementary use of *ab initio* calculations (usually density functional theory (DFT)) and X-ray diffraction methods to create a complete picture of the problem at hand. However, it should be stressed that while useful, these data are not always required. For example, protein structure solutions regularly make use of two- or three-dimensional NMR data without recourse to diffraction-based models. Alternatively, NMR data can often validate structural features seen in diffraction-based crystal structures in the absence of DFT calculations. Other analytical methods fall under the umbrella of NMR crystallography [5], such as powder X-ray diffraction, single-crystal X-ray diffraction, infrared spectroscopy, thermal analysis, and scanning electron microscopy.

There are many reasons to study crystal structures. There are a plethora of examples where crystal structures may adopt different phases, called polymorphs, because of the unique crystal growth medium or method used. It is essential to understand the nature of the differences between

polymorphs. Noncovalent interactions play a vital role in the formation of crystal structures, and solid-state NMR is used extensively to understand the nature of such interactions, including hydrogen bonds and  $\sigma$ -hole interactions, and how they play a role in guiding crystallization. Crystal structures may convert into other forms because of external effects (e.g. temperature, pressure) or, in the case of pharmaceuticals, the presence of excipients and other ingredients in a pharmaceutical formulation. Polymorphs are especially crucial in pharmaceutical sciences because each polymorph of an active pharmaceutical ingredient (API) generally behaves differently from another in terms of their bioavailability, but also because each polymorph can be subject to a patent.

This chapter covers many of the latest developments in NMR crystallography and polymorphism. Our main effort is to detail a variety of examples and applications from 2016 onwards that have shown solid-state NMR to be a handy and successful tool to understand polymorphism in both organic and inorganic systems. We also discuss NMR crystallography in the context of noncovalent interactions by featuring some of the latest developments from our group and others. We also discuss some new and exciting research into understanding dynamic processes in the solid state. We finalize our discussion by exploring some other approaches related to solid-state NMR for studying NMR crystallography. For an excellent recent summary of the developments of NMR crystallography of organic systems, we refer the reader to the 2020 review by Hodgkinson [6].



## 2. Theory

### 2.1 NMR interactions

It is worthwhile to provide a short overview of the nuclear spin interactions relevant to solid-state NMR and NMR crystallography. For an isolated spin-1/2 nucleus, a peak measured in an NMR spectrum is characterized by its chemical shift ( $\delta$ ) which originates from the magnetic shielding ( $\sigma$ ) interaction, given by the frequency  $\nu = (1 - \sigma) \frac{\gamma B_0}{2\pi}$ . The magnetic shielding tensor may be expressed in diagonal form such that the interaction is represented in its principal axis system (PAS) where  $\sigma_{11} \leq \sigma_{22} \leq \sigma_{33}$ . The shielding constant is manifested directly in the NMR spectrum in the form of a chemical shift  $\delta$ . The chemical shift (CS) is related to the magnetic shielding constant by  $\delta = \frac{\sigma_{\text{ref}} - \sigma}{1 - \sigma_{\text{ref}}}$  and the isotropic chemical shift,  $\delta_{\text{iso}}$ , is given as the average of the three chemical shift tensor components:  $\delta_{\text{iso}} = \frac{\delta_{11} + \delta_{22} + \delta_{33}}{3}$ . There are

multiple ways [7] of expressing the chemical shift anisotropy (CSA). In the Herzfeld-Berger convention [8], the span and skew of the tensor are given by  $\Omega = \delta_{11} - \delta_{33}$  and  $\kappa = \frac{3(\delta_{22} - \delta_{iso})}{\Omega}$ , whereas in the Haeblerlen convention [9], the chemical shift tensor is described in terms of its anisotropy and its asymmetry:  $\Delta\delta = \delta_{zz} - \frac{\delta_{xx} + \delta_{yy}}{2}$  and  $\eta = \frac{\delta_{yy} - \delta_{xx}}{\delta_{zz} - \delta_{iso}}$ .

For spin-1/2 nuclei, the CSA is the dominant interaction affecting the NMR spectrum. The situation changes for quadrupolar nuclei ( $I \geq 1$ ), which possess a non-spherical charge distribution. NMR spectra are therefore affected by the quadrupolar interaction between the electric field gradient (EFG) at the nucleus and the nuclear electric quadrupole moment ( $Q$ ). This interaction is described in terms of the quadrupolar coupling constant ( $C_Q = \frac{eV_{zz}Q}{h}$ ) and the quadrupolar asymmetry parameter ( $\eta_Q = \frac{V_{xx} - V_{yy}}{V_{zz}}$ ). The principal axis systems of the CS and EFG tensors are related by a set of Euler angles,  $\alpha$ ,  $\beta$ , and  $\gamma$ , which can give rise to important information about local symmetry at a particular nucleus, [10] and indeed about the overall crystallographic symmetry.

One must be cautious when interpreting solid-state NMR spectra of quadrupolar nuclei. These spectra are generally affected by second-order quadrupolar shifts, where the apparent isotropic shift is displaced from the true chemical shift by the second-order quadrupolar interaction. We direct the reader to a thorough account of this effect and how it can be modelled [11]. Besides second-order quadrupolar effects, some systems can exhibit the influence of higher-order quadrupole effects, which can manifest in the form of non-uniform frequency shifts of the spectrum and must be considered [12–15].

Dipolar coupling arises from the interaction of magnetic dipoles through space. The dipolar coupling constant is inversely related to the motionally-averaged inverse cube of the internuclear distance,  $r_{12}$ , between a pair of spins, and is given by:  $R_{DD} = \left(\frac{\mu_0}{4\pi}\right)\left(\frac{\gamma_1\gamma_2\hbar}{2\pi}\right)\langle r_{12}^{-3} \rangle$  where  $\mu_0$  is the vacuum permittivity,  $\gamma$  is the gyromagnetic ratio, and  $r$  is the distance between nuclei 1 and 2.

Dipolar coupling can manifest itself in several ways depending on the spin system under study. In general terms, the effects can be minimized by using higher magnetic fields and/or fast magic angle spinning. There are also several advanced radiofrequency schemes available for proton decoupling.

*J*-coupling between nuclear spins is mediated by the intervening electronic structure. While these couplings can be taken advantage of to gain information about molecular structures, they may often be overshadowed by other larger effects in the solid state. They are therefore relatively rarely measured directly in NMR crystallographic approaches, but when they are measured, *J*-couplings can provide useful information about the relative arrangement of NMR-active nuclei in the crystal structure. There are many recent examples of *J*-couplings having been measured in the solid state [16].  $^1J(^{13}\text{C}, ^{17}\text{O})$  couplings have been used to characterize O positions in naphthalaldehydic acid [17]. Also,  $(^1\text{H}, ^{17}\text{O})$  *J*-couplings were measured and compared to theoretical calculations in a series of oxygen-containing crystal structures [18]. Our group observed  $^1J(^{77}\text{Se}, ^{31}\text{P})$  couplings in halogen bonded  $\text{P}=\text{Se} - \text{I}$  motifs [19]. *J*-couplings between quadrupolar nuclei have been used to probe the electronic properties and dynamics of digallium [20] and diborane compounds [21].

## 2.2 Methodology

A detailed account of NMR methodology used to characterize organic crystals and their polymorphs is available in the recent review by Hodgkinson [6]. Below, we only touch on some of the key methods used in the applications discussed later in this chapter.

The homonuclear dipolar coupling has a broadening effect on the line shapes of  $^1\text{H}$  NMR spectra of organic solids. Much effort has been put into improving  $^1\text{H}$  solid-state NMR through the use of various pulse sequences and, because line narrowing is proportional to the spinning frequency, by using faster magic angle spinning. At the time of writing this chapter, to our knowledge, the fastest achieved magic angle spinning frequencies were 130 kHz, [22] 140 kHz, [23] and 150 kHz [24].

In combining MAS with sophisticated homonuclear dipolar decoupling sequences, such as  $^1\text{H}$  CRAMPS (combined rotation and multiple-pulse spectroscopy), it is possible to get high-resolution  $^1\text{H}$  solid-state NMR spectra because of the line narrowing resulting from the averaging of chemical shift anisotropy and the reduction of dipolar couplings. Examples of decoupling mechanisms are the Lee-Goldburg techniques [25–28], WAHUHA [29], MREV-8 [30,31], BR-24 [32], or the family of DUMBO sequences [33–35], which has become increasingly used in recent years (Fig. 1).

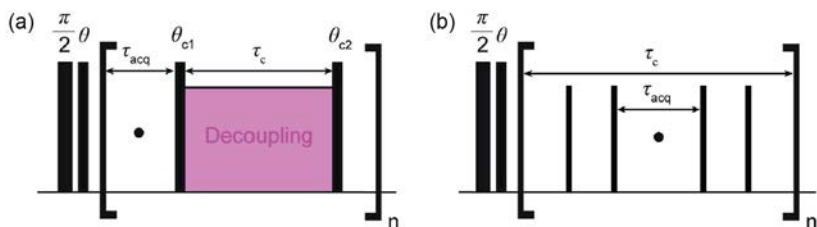


**Fig. 1** An example showing the pulse sequences for conventional (A) windowed and (B) windowless 1D  $^1\text{H}$  CRAMPS decoupling schemes. Adapted from F.M. Paruzzo, L. Emsley, High-resolution  $^1\text{H}$  NMR of powdered solids by homonuclear dipolar decoupling, *J. Magn. Reson.* 309 (2019) 106598. <https://doi.org/10.1016/j.jmr.2019.106598>. Used with permission.

High-resolution proton NMR is used alongside a variety of methods for NMR crystallography, including crystal structure prediction [36,37]. Experimental  $^1\text{H}$  NMR schemes routinely use a combination of ultrafast magic angle spinning, sophisticated pulse sequences, and homonuclear decoupling routines to average out dipolar couplings and thus enhance the resolution and sensitivity of  $^1\text{H}$  line shapes [38–40].

Using the dipolar interaction has been critical in NMR crystallography. Often, long-range interactions can be explored using NMR data, and the dipolar coupling can provide information about the internuclear distance between atom 1 and atom 2. Under MAS conditions, van Rossum et al. initially proposed a method of determining long-range heteronuclear  $^1\text{H}$ - $^{13}\text{C}$  distances using Lee-Goldburg (LG) cross-polarization and LG decoupling [41]. In this experiment,  $^1\text{H}$ - $^1\text{H}$  dipolar couplings are suppressed by tilting the magnetization to the LG-CP condition, allowing for the observation of weaker  $^1\text{H}$ - $^{13}\text{C}$  couplings absent of any effects because of homonuclear dipolar coupling. Here, a  $\text{COOH}\cdots\text{O}(\text{H})\text{C}$  hydrogen bond in tyrosine hydrochloride was measured to be  $2.47\text{ \AA}$ , in close agreement with previous neutron diffraction studies ( $2.521\text{ \AA}$ ), thereby confirming the robustness of this experiment.

Cross-polarization (CP) techniques, including the well-known CP/MAS experiment, are used extensively for structural studies.  $^1\text{H}$ - $^{13}\text{C}$  CP is more broadly applied to two-dimensional heteronuclear methods *via* through-space correlation (HETCOR), where, for example, the  $^1\text{H}$ - $^{13}\text{C}$  frequency swept LG heteronuclear correlation experiment (FSLG-HETCOR) [41] has been used to characterize solids from small organic molecules to complex pharmaceuticals. An extension to one-dimensional CRAMPS, two-dimensional double-quantum-single-quantum (DQ/SQ) experiments under magic angle

spinning can provide valuable information about the proximities between hydrogen atoms [42]. These correlations may be paired with  $^1\text{H}$ - $^{13}\text{C}$  HETCOR experiments to provide a complete description of the bonding within a chemical structure.

HETCOR can also be applied to half-integer quadrupolar nuclei. Cross-polarization efficiency under magic angle spinning from protons to quadrupolar nuclei is usually adversely affected by the difficulty of maintaining spin-locking in the presence of the quadrupolar interaction [43]. Numerous approaches have been developed to deal with these issues [44–49], including dipolar HMQC (D-HMQC) or D-RINEPT experiments, which are slightly better performing because of their ability to minimize the effects of proton relaxation on the spectrum. Recently, Venkatesh et al. proposed TONE D-HMQC sequences for eliminating  $t_1$  noise in proton detected D-HMQC spectra [50]. D-HMQC and D-RINEPT methods have been used in recent examples to detect quadrupolar nuclei through proton detection [18,51–54]. Other examples include REDOR [55] or the closely related REAPDOR [56,57] experiments for probing dipolar coupling interactions and measuring chemical bond distances to get structural constraints.

Recently, Perras et al. proposed a new strategy for reducing problems associated with the indirect detection of heavy spin-1/2 nuclei using D-HMQC, by combining it with magic angle turning (MAT) [58]. This two-dimensional technique uses broad-banded-MAT in the indirect dimension to fold the spinning sidebands in ultra-wide line D-HMQC MAS experiments to resolve ‘infinite-speed’ MAS spectra, meaning spectra are obtained with true solution-like line widths. In the study, a high-resolution  $^{195}\text{Pt}$  NMR spectrum was acquired for decomposed transplatin (Fig. 2) with sensitivity comparable to that which would be obtained by using dynamic nuclear polarization. The experiment enabled the authors to propose a hydrolysis decomposition pathway for transplatin, assigning resonances to five distinct Pt sites, including the amorphous transplatin (−2070 ppm), and the Pt(IV) coordination products resulting from the hydrolysis step. Notably, in this case, the sideband suppression enabled the detection of a previously hidden signal corresponding to  $[\text{PtCl}_6]^{2-}$  at 130 ppm, helping to confirm the proposed decomposition pathway.

Other experiments deal with the direct observation of quadrupolar nuclei. WURST-QCPMG [59–61] combines frequency-swept wideband uniform rate smooth truncation pulses (WURST) [62,63] with CPMG to give rise to a pulse sequence for improving the direct observation of

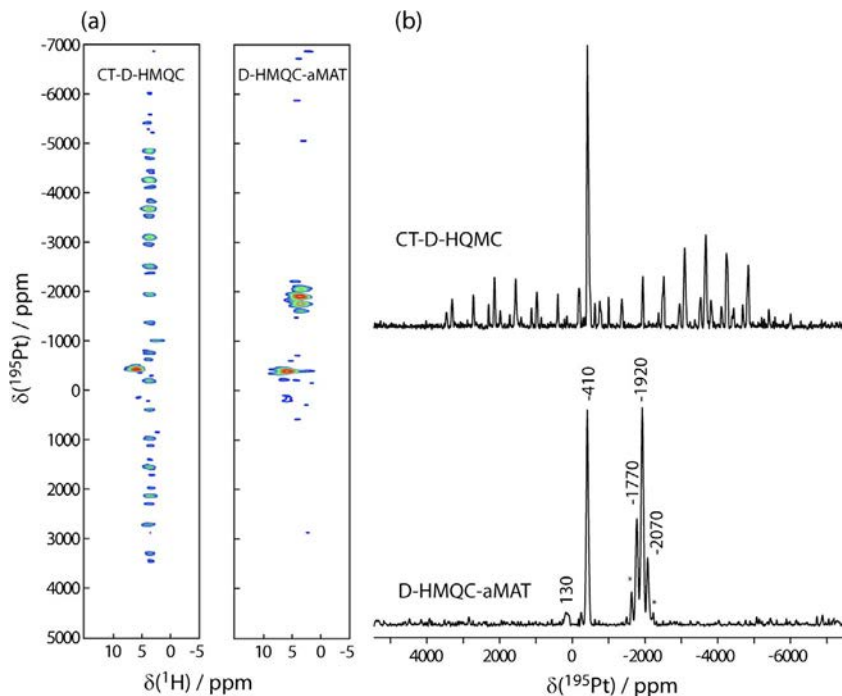


**Fig. 2** An illustrative example of the sideband-suppression from the magic angle spinning D-HMQC-aMAT pulse scheme used to observe a sample of decomposed transplatin. (A) Two-dimensional continuous-time (CT) D-HMQC and F-HMQC-aMAT spectra are shown next to each other for comparison. (B) The  $^{195}\text{Pt}$  projections are shown, demonstrating the elimination of sidebands by using MAT (bottom), even uncovering a previously undetected Pt(II) signal at 130 ppm. From F.A. Perras, A. Venkatesh, M.P. Hanrahan, T.W. Goh, W. Huang, A.J. Rossini, M. Pruski, *Indirect detection of infinite-speed MAS solid-state NMR spectra*, *J. Magn. Reson.* 276 (2017) 95–102. <https://doi.org/10.1016/j.jmr.2017.01.010>. Used with permission.

quadrupolar nuclei. BRAIN-CP [64] pulse schemes were subsequently devised to make use of broadband adiabatic inversion pulses to broaden the bandwidth of CP transfer. These methods have been used several times in recent years and surveyed by Leroy and Bryce [65]. Two-dimensional multiple-quantum MAS (MQMAS) experiments [66] allow for insight into the structural arrangement of quadrupolar species in disordered or amorphous samples, giving rise to higher resolution in these sorts of examples because of the minimization of the effects of the quadrupolar interaction on the NMR signals. We have employed MQMAS to study nepheline ( $\text{NaAlSiO}_4$ ) based glass-ceramics [67].



Theoretical calculations are often employed alongside solid-state NMR experiments [68] to rationalize the results obtained, for example, either for peak assignment or line shape analysis, and are applied frequently towards structural refinement in crystals [69–72]. Theoretical studies are often performed on their own to generate general understandings of the NMR response to various structural and crystal packing effects. Programs such as CASTEP/NMR [73–79], Quantum Espresso [80,81], ADF NMR [82–86] (which can account for relativistic effects [87–89]), ABINIT [90], and others have played essential roles in the calculation of energy minimized gas-phase or crystal structures and their corresponding NMR parameters.



## **3. NMR crystallography and polymorphism**

### **3.1 Polymorphism**

#### **3.1.1 Packing polymorphism**

Polymorphism is the ability of a substance to crystallize in more than one distinct crystal structure and forms the basis of many questions in NMR crystallography. Understanding polymorphism extant in solids of interest is essential because the arrangement of a crystal structure can affect the way it dissolves or, in the case of pharmaceuticals, their bioavailability. For example, a crystallization process can yield a kinetic or thermodynamic product, or multiple forms thereof, depending on the imposed conditions. Packing polymorphism occurs when the arrangement of molecules changes in the formation of a crystal structure, depending on the external conditions such as the crystallization solvent used, ambient temperatures or pressures.

The use of solid-state NMR for characterizing organic solids and APIs is well established. Solid-state NMR methods are used extensively to describe the structures and noncovalent bonding networks present in pharmaceutical solids. However, one of the biggest challenges to drug manufacturers is polymorphism, the possibility that a particular crystal structure alters its phase spontaneously or during manufacturing processes. Polymorphism can impact the function of an API's solvation properties or bioavailability [91]. Much effort has been put into establishing protocols whereby polymorphs can be identified either in pure phases or as pharmaceutical mixtures (including excipients and other ingredients).

One-dimensional solid-state NMR often suffices for detecting polymorphism. For example, one-dimensional  $^{13}\text{C}$  solid-state NMR is usually suitable for studying the significant differences from one polymorph to another.

$^{13}\text{C}$  CP/MAS has been used to study polymorphism in piracetam [92], an API related to the treatment of Alzheimer's and dementia. It exists in three stable forms at normal pressures obtained by recrystallization in different solvents, or by heating (form II and form III; and form I, respectively). The unambiguous assignment of carbon peaks in  $^{13}\text{C}$  CP/MAS spectra was used to study the differences between the three polymorphs, which can be done at moderate magnetic field strengths. However, molecules like piracetam feature many nitrogen atoms. So it is crucial to take into account broadening and splitting of the  $^{13}\text{C}$  signal due to residual dipolar coupling to  $^{14}\text{N}$ . The splitting should not be mistaken as overlapping  $^{13}\text{C}$  signals or  $J$ -coupling. This issue can often be resolved by running the experiments at higher magnetic field strengths. One goal of identifying polymorphs is to determine the constitution of pharmaceutical formulations. A comparison between the pure form of piracetam to a series of commercial formulations, which include excipients and other ingredients, shows that the form III polymorph is most often used in pharmaceutical formulations. DFT was further used in this paper to study the effects of temperature on the stability of the unique forms of the polymorph, giving insights into the processes by which the three forms can interconvert at different temperatures.

One-dimensional solid-state NMR may not be sufficient for characterizing polymorphs in a more complex pharmaceutical sample. Often, drug molecules are complex and exhibit overlapping chemical shifts. Two-dimensional methods such as HETCOR are very useful in these circumstances because they allow not only for the identification of a species through 'fingerprinting', but also structural elucidation based on heteronuclear through-space correlations. An example of this is the case of cefazolin sodium [93], a cephalosporin antibiotic that forms four distinct phases depending on the preparation method: the  $\alpha$ -form (pentahydrate),  $\beta$ -form (sesquihydrate),  $\gamma$ -form (methanol solvate) and the amorphous phase.  $^{13}\text{C}$  CP/MAS showed clearly that, in fact, among a series of commercial formulations prepared by different vendors, the  $\alpha$ -form is usually used. Nevertheless, between different pharmaceutical manufacturers, subtle differences between preparations, likely resulting from the manufacturing process, can even be probed. Solid-state NMR provides a clear picture of the differences between the cefazolin formulations prepared by three different vendors and reveals subtle differences in formulations containing the  $\alpha$ -form, specifically at the C19 and C14 sites. This conclusion was confirmed by two-dimensional  $^1\text{H}$ - $^{13}\text{C}$  HETCOR spectra and attributed to a phenomenon related to the unique arrangements of the molecules within

the unit cell. Here, theoretical calculations exploring the change in the shape of the C19 signal from one formulation to the next show that this is related to the formation of a hydrogen bond in conformation 2, while the signal at C14 is affected by the degree to which conformation 2 is present in the formulation. This study showed the power of solid-state NMR for detecting very subtle changes in the arrangements of atoms or side chains in a crystal structure, despite the unit cell parameters remaining largely the same.

Cimetidine is a marvellous example of a pharmaceutical solid that has been used for the development of solid-state NMR methodology related to NMR crystallography. One of the main problems with cimetidine has been the assignment of carbon peaks for all of its polymorphs. Multiple solid-state NMR studies have been applied to this drug, and in fact, the solid-state NMR analysis of cimetidine has also been proposed as a case study for educational purposes in advanced analytical laboratories [94].

Cimetidine polymorphism has been known since the 1970s [95–97]. It is known to crystallize into four anhydrous phases, a monohydrate, and several hydrochloride salts. While most forms of cimetidine have been characterized already, polymorph A has been difficult, and it is important because it usually makes up commercially available pharmaceutical formulations. Forms A–D and M1 of cimetidine were characterized by a  $^{13}\text{C}$  CP/MAS study ( $\nu(^{13}\text{C})=90.55\text{ MHz}$ ) in 1997 by Middleton et al., highlighting the differences between their  $^{13}\text{C}$  fingerprints in the presence of excipients [98]. Peaks were assigned by comparing solid-state chemical shifts to the spectra obtained *via* site-selective isotope labelling in solution NMR. Alternatively, spectral editing of methylene signals was applied in the solid state. Splittings were rationalized based on the presence of second-order quadrupolar effects or multiple molecules in the asymmetric unit, except for forms B and C, which did not have crystal structures available. In a follow-up paper,  $^{13}\text{C}$  CP/MAS, rotational resonance, and double quantum heteronuclear field (DQ-HLF) MAS NMR experiments were used to estimate distances and assign  $^{13}\text{C}$ – $^{13}\text{C}$  internuclear distances and C–H bond orientations in  $^{13}\text{C}$ -labelled forms A, B, C, and M1 [99]. Constant-time REDOR experiments were instrumental in obtaining structural restraints based on C– $^{15}\text{N}$  dipolar coupling in the crystal structure determination of singly  $^{15}\text{N}$ -labelled polymorph A [100]. From the observed dephasing curves at each carbon site,  $^{13}\text{C}$ – $^{15}\text{N}$  bond distances could be calculated to derive torsional constraints used for crystal structure determination by powder X-ray diffraction. Doubly-labelled cimetidine,

where  $^{13}\text{C}$  and  $^{15}\text{N}$  spins are several bonds apart, allowed for the measurement of torsional constraints by measuring  $^{13}\text{C}$ - $^{15}\text{N}$  dipolar couplings [101].

Spectral enhancements can be obtained by exploiting  $J$ -couplings and dipolar couplings between spin pairs. For example, in proton-detected double resonance (D-RINEPT) experiments, it has been demonstrated [18] that  $^{17}\text{O}$  signals can be enhanced and the overlapping resonances can be separated because of their correlated  $^1\text{H}$  chemical shifts. D-RINEPT experiments may be modified to be  $J$ -resolved or may incorporate separated local field blocks, allowing for the measurement of  $^1\text{H}$ - $^{17}\text{O}$  scalar and dipolar couplings, respectively. In this paper, measured dipolar couplings were used to probe bond lengths between H and other heteronuclei, elucidating distances in good agreement with geometries obtained both by DFT and X-ray crystallography. In another example, single-bond  $^{15}\text{N}$ - $^1\text{H}$   $J$ -couplings were used to distinguish between  $^{15}\text{N}$  sites with different numbers of covalently bonded hydrogen atoms [102]. While this approach is powerful, the downside to this method is that it usually requires isotopic labelling for optimal signal detection.

Homonuclear double-quantum (DQ) NMR methods make use of the homonuclear dipolar coupling present between spin pairs to generate double-quantum coherences. The DQ excitation is measured in the indirect dimension of a 2D double-quantum/single-quantum spectrum (DQ-SQ). While this approach is useful for measuring homonuclear correlations, it also serves a valuable purpose for distinguishing between polymorphs. For example, Maruyoshi et al. showed that  $^1\text{H}$  double-quantum MAS NMR spectroscopy can detect a minority phase of a polymorph present in a physical mixture [103]. Their work sought to determine the lower limit of detection by  $^1\text{H}$  DQ MAS NMR of the free form of cimetidine (polymorph A) in a sample of the anhydrous hydrochloride salt of cimetidine. These were distinguished by considering the  $^1\text{H}$  peaks corresponding to a short intramolecular correlation of protons (C-H to N-H) on imidazole rings (2.55 Å for the hydrochloride salt, and 2.57 Å for polymorph A). The  $^1\text{H}$  double quantum shifts were determined to be 24.4 ppm for the HCl salt, and 19.0 ppm for polymorph A. Using this information, it was determined through experimentation that polymorph A could be detected in quantity as low as 1% *w/w* (Fig. 3). The report suggests that  $^1\text{H}$  DQ MAS NMR spectroscopy can distinguish between two crystalline phases in a sample, even if one phase is present in a vast minority. However, two-dimensional DQ-SQ NMR can be time-consuming. To a similar end, Hong et al. recently proposed a new method for the selective  $^1\text{H}$  detection of APIs in tablet formulation using the

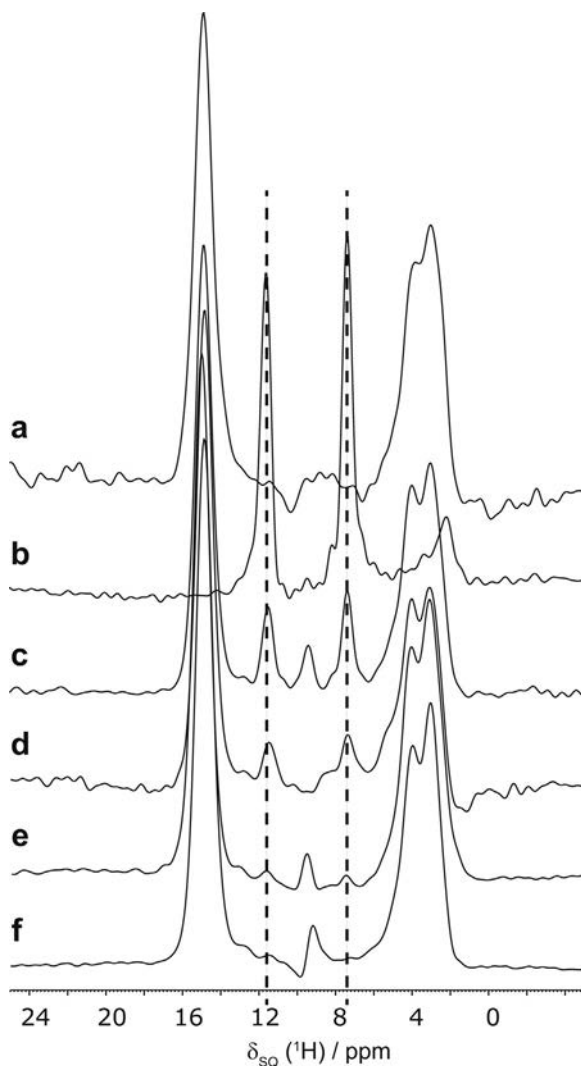


**Fig. 3** Slices of the  $^1\text{H}$  DQ frequency of 19.0 ppm, as extracted from two-dimensional  $^1\text{H}$  DQ MAS spectra of (A) the anhydrous HCl salt of cimetidine, (B) polymorph A of cimetidine, and (C–F) physical mixtures of polymorph A and the anhydrous HCl salt with (C) 10%, (D) 5%, (E) 1%, and (F) 0.5% w/w of polymorph A. From K. Maruyoshi, D. Iuga, A.E. Watts, C.E. Hughes, K.D.M. Harris, S.P. Brown, *Assessing the detection limit of a minority solid-state form of a pharmaceutical by  $^1\text{H}$  double-quantum magic-angle spinning nuclear magnetic resonance spectroscopy*, *J. Pharm. Sci.* 106 (2017) 3372–3377. <https://doi.org/10.1016/j.xphs.2017.07.014>. Used with permission.

$^1\text{H}\{^{14}\text{N}\}$  PM-S-RESPDOR-RFDR pulse sequences [104]. Their approach demonstrates enhancement of the desired narrow  $^1\text{H}$  signals resulting from the L-cysteine API in a pharmaceutical formulation.

Despite all the efforts put towards cimetidine, the explicit  $^{13}\text{C}$  chemical shift assignment has remained a problem. However, Holmes et al. proposed a different approach in a recent study, by exploiting the variations in the chemical shift tensors for each  $^{13}\text{C}$  resonance of cimetidine Form A. The chemical shift tensors for each crystallographically distinct carbon site are measured and compared to DFT calculations to assign the  $^{13}\text{C}$  chemical shifts [105]. The five- $\pi$  replicated magic angle turning (FIREMAT) [106] procedure was used at 14.1 T to obtain the principal components of the  $^{13}\text{C}$  shift tensors of cimetidine within an error of 0.7 ppm and compared with gauge including projector augmented wave density functional theory (GIPAW DFT) calculations using hybrid functionals. Spinning sidebands were analysed for each of the carbon sites to provide unambiguous differences associated with each of the resonances (Fig. 4). With this information, the resonances could be fully assigned, and the method offers an approach that is different but perhaps more effective for the assignment of  $^{13}\text{C}$  peaks. Finally, when calculated CSA tensors were compared to the experimental spectra, the peaks could be assigned.

The prediction of heteronuclear correlations by density functional theory calculations is crucial for the assignment of resonances leading to the validation of different crystal structures. Two-dimensional correlations can be predicted based on either the calculated dipolar or  $J$ -couplings obtained in CASTEP and plotted using software such as MagresView [107]. In a case study, homonuclear and heteronuclear correlation techniques were used to study metergoline, a relatively sizeable organic molecule and pharmaceutical ingredient. The results were analyzed alongside DFT calculations taking into account the influence of crystal-lattice effects on the chemical shifts [108]. This study shows that GIPAW DFT calculations, using the PBE or rPBE functionals on both monomers and crystal structures, can accurately predict the  $^1\text{H}$ - $^{13}\text{C}$  chemical shift correlations in metergoline with  $R^2$  values greater than 0.99. This paper showed the importance of first-principles calculations of NMR tensors for the verification of crystal structures. Along the same lines, in a follow-up paper [109], the authors described a procedure in depth whereby solid-state NMR and DFT calculations are applied to crystal structures of polymorphs of metergoline, Form I and Form II (MI and MII, respectively; the latter which had been studied previously by 2D NMR methods [110]). As opposed to Form I, Form II is

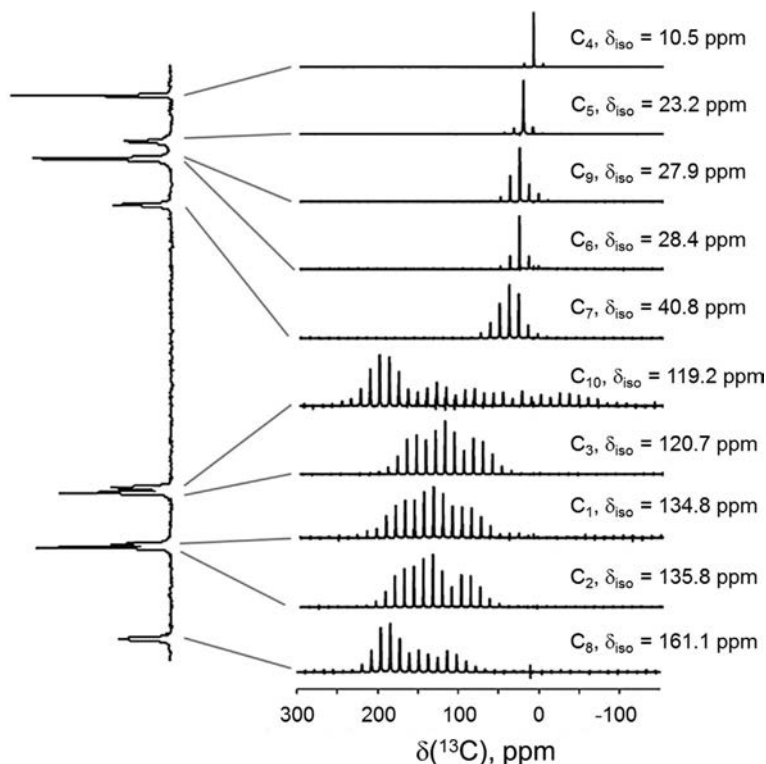


**Fig. 4**  $^{13}\text{C}$  FIREMAT spectrum of cimetidine Form A acquired at 14.1 T. The signals (left) are selectively analyzed to get the CSA tensor at each site (right). *Reprinted with permission from S.T. Holmes, O.G. Engl, M.N. Srnc, J.D. Madura, R. Quiñones, J.K. Harper, R.W. Schurko, R.J. Iulucci, Chemical shift tensors of cimetidine form a modeled with density functional theory calculations: implications for NMR crystallography, J. Phys. Chem. A 124 (2020) 3109–3119. <https://doi.org/10.1021/acs.jpca.0c00421>. Copyright 2020 American Chemical Society.*

more complicated because it contains two unique molecules in the unit cell, and so not all the individual  $^{13}\text{C}$  and  $^1\text{H}$  resonances could be assigned by traditional correlation methods, and  $^{13}\text{C}$ - $^{13}\text{C}$  CP-INADEQUATE experiments could not predict the backbone of the structure because of the presence of several heteroatoms. With MII, the previously described automated approach of using GIPAW DFT methods to predict  $^1\text{H}$ - $^{13}\text{C}$  correlations carefully was adopted [111]. The resulting assignment of peaks was considered to be unambiguous, measured by the covariance between the calculated and experimentally obtained NMR signals. It should be noted that in the same paper the authors also explored the comparisons

of computationally predicted crystal structures to the NMR correlational data and found that the observed  $^{13}\text{C}$  chemical shift tensor information could be compared to the calculated tensors from predicted crystal structures to identify the correct polymorph.

In a similar example, Zilka et al. reported the combined use of solid-state NMR and GIPAW DFT in the study of three polymorphs of furosemide (form I, form II, and form III) and rationalized the differences between them in terms of their packing characteristics as determined through the experimental data [112]. Chemical shifts were assigned based on the NMR data collected from GIPAW DFT calculations on geometry optimized crystal structures compared with both  $^{13}\text{C}$  CP/MAS, and 2D refocused INEPT (12.5 kHz MAS) experiments showing one-bond  $^1\text{H}$ - $^{13}\text{C}$  correlations. A representative spectrum in Fig. 5A shows the chemical shift assignments for both molecules of furosemide present in the unit cell of form I. The calculated  $^{13}\text{C}$  resonances are correlated with calculated  $^1\text{H}$  resonances and overlaid on the 2D INEPT spectrum as shown as crosses in Fig. 5B.

In this paper, several solutions to the crystal structures deposited in the CSD were geometry optimized to determine the best crystal structure to use for the calculation of both NMR shieldings and nucleus-independent chemical shifts (NICS). Three crystal structures were indistinguishable from each other after optimizations with relaxed unit cells. GIPAW DFT was used to analyze the difference between the chemical shifts of the three polymorphs with a focus on intermolecular bonding and ring currents. In the procedure used, a crystal structure is first geometry optimized, and then the magnetic shielding values are calculated from full periodic crystals (Crys) and later as single isolated molecules in the unit cell (Mol). The difference (Crys-Mol) quantifies the effects from the crystal lattice on the shielding tensors. The NICS value at each  $^1\text{H}$  site is computed in CASTEP and extracted. Regarding the isolated molecules, the only difference seen between each of the three polymorphs is the  $^1\text{H}$  chemical shift ( $>1$  ppm) at H8, setting form III apart from the other configurations. This chemical shift change results from differences in the torsion angle at the N-C bond in the furan ring. When compared to the calculations on the full crystal structures, further variations are attributed to intermolecular hydrogen bonds and long-range crystal effects. These results nicely show that differences in NMR responses in polymorphs are likely more related to molecular packing in the crystal structure, rather than molecular geometries—but the authors conceded that one is not exclusive of the other. Concurrently, the calculated NICS values gave rise to useful information



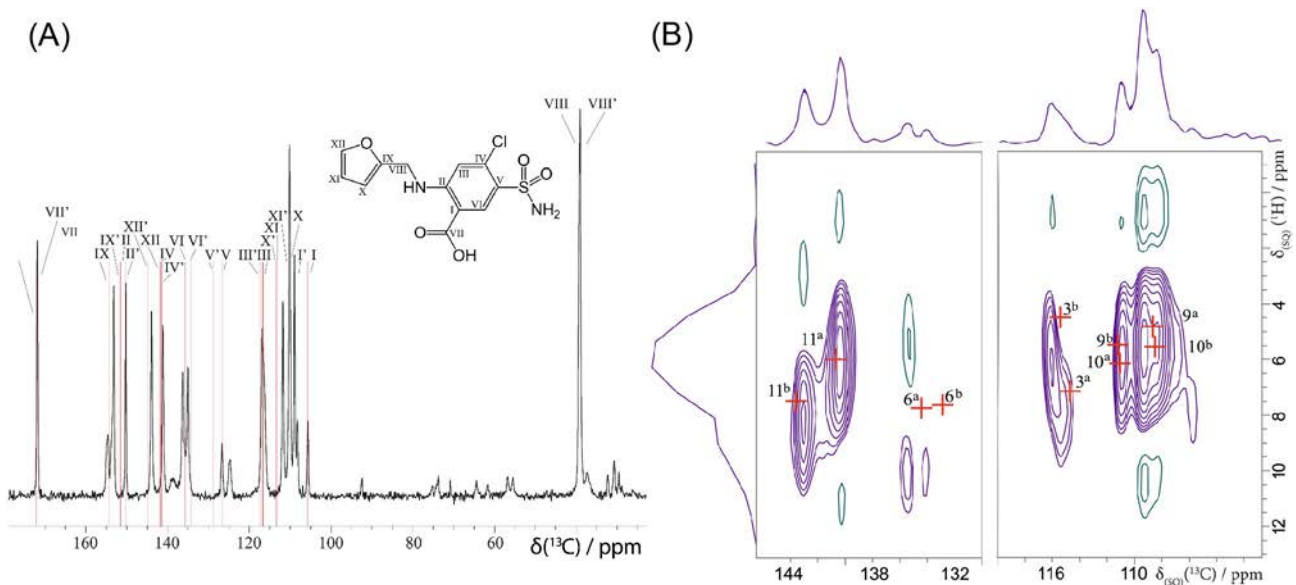


**Fig. 5** (A)  $^1\text{H}$ - $^{13}\text{C}$  CP/MAS spectrum of furosemide (form I) with GIPAW DFT calculated chemical shifts shown by red lines. (B) Two-dimensional  $^1\text{H}$ - $^{13}\text{C}$  refocused INEPT spectrum of furosemide (form I) with GIPAW DFT calculated correlations overlaid in red. Adapted from M. Zilka, J.R. Yates, S.P. Brown, *An NMR crystallography investigation of furosemide*, *Magn. Reson. Chem.* 57 (2018) 191–199. <https://doi.org/10.1002/mrc.4789>. Used with permission.

about which hydrogen atom is interacting with the ring. In each of the polymorphs, a different hydrogen atom interacts with the rings and this is visualized in Fig. 6 in the form of magnetic shielding contribution maps [113]. Overall, the results of the study demonstrated that the differences in the

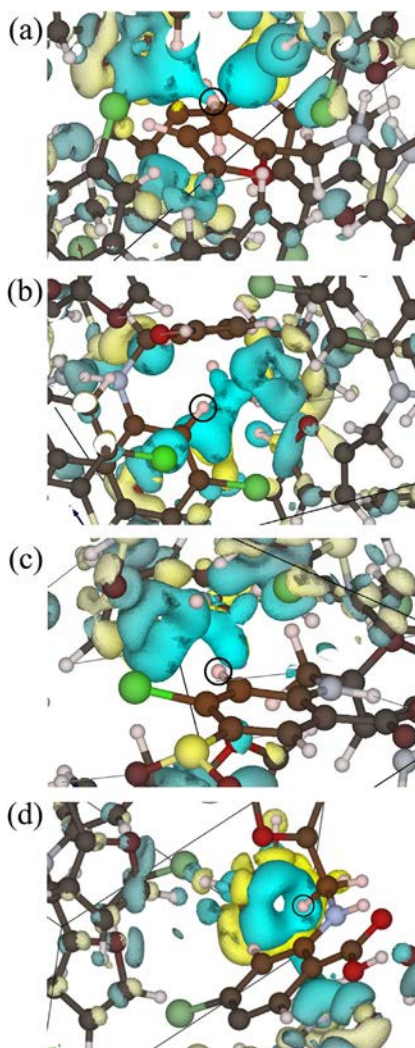


**Fig. 6** Visualization of the effects of ring currents on  $^1\text{H}$  chemical shifts of hydrogen atoms in furosemide polymorphs: (A) molecule A of form I, (B) molecule B of form I, (C) form II, and (D) form III. The diagrams are constructed from Magnetic Shielding Contribution Field (MSCF) maps obtained by theoretical calculations. From M. Zilka, J.R. Yates, S.P. Brown, *An NMR crystallography investigation of furosemide*, *Magn. Reson. Chem.* 57 (2018) 191–199. <https://doi.org/10.1002/mrc.4789>. Used with permission.

NMR response between the three polymorphs are directly a result of the interactions arising in the crystal structure because of long-range effects such as packing, a conclusion only revealed thanks to the help of GIPAW DFT calculations.

In a traditional approach to NMR crystallography, Sene et al. combined experimental results with theoretical calculations to study the crystal structures of benzoxaboroles, which are hemiesters of aryl boronic acids [114]. In their work, they looked at two benzoxaboroles: the antifungal drug AN2690 and its non-fluorinated analogue, BBzx. By definition, they are not polymorphs because their chemical structures differ by the fluorination of AN2690—however, analogues such as these are of interest in pharmacology because the halogenation seems to play an important role in rational drug design due to the importance of halogen bonding in ligand bonding affinity [115–120], and serves as a useful example for this discussion.

Both AN2690 and BBzx share very similar traits in that they both possess P-1 space groups and have similar unit cell angles and lengths, except for  $c$ , where that of BBzx is almost double the length, giving rise to double the unit cell volume. They are also similar in that they form benzoxaborole dimers *via* hydrogen-bonding networks. Unsurprisingly, however, the addition of the fluorine atom in AN2690 leads to an additional C-H $\cdots$ F hydrogen bond. Both crystal structures undergo some thermal expansion, with AN2690 being considerably more affected than BBzx. Because of the strong similarities between the two structures, there is an interest in characterizing them by solid-state NMR.  $^1\text{H}$ ,  $^{13}\text{C}$ , and  $^{11}\text{B}$  solid-state NMR experiments were conducted on both AN2690 and BBzx for full characterization. The downside of this compound, along with a vast number of other APIs, is a hydrogen bond to fluorine, which means  $^1\text{H}$  NMR is challenging. Because of strong  $^{19}\text{F}$ - $^1\text{H}$  dipolar couplings, resolution in the  $^1\text{H}$  DUMBO spectrum of N2690 was very poor and did not allow for much of a comparison with BBzx. Concurrently, the  $^{11}\text{B}$  MAS NMR spectrum shows similar line shapes between both compounds because of the similarities in the bonding environments between both compounds. Both have very close  $C_Q$  values: 2.8 MHz (AN2690) and 2.9 MHz (BBzx), and both with  $\eta \sim 0.5$ , which is unsurprising given that both crystal structures feature nearly identical  $^{11}\text{B}$  environments. The most significant difference was observed in the  $^{13}\text{C}$  CP/MAS spectrum. The peak corresponding to AN2690 features a reasonably large splitting, which the authors attribute to  $^{19}\text{F}$ - $^{13}\text{C}$   $J$ -coupling. On the other hand, the crystal structure of BBzx is complicated because it contains two crystallographically distinct molecules in the unit cell and thus features some resonances which 1D NMR techniques cannot be used to

resolve because of peak overlap. This example serves to illustrate that sometimes, NMR experiments on various heteronuclei may not always be useful in differentiating polymorphs and that  $^{13}\text{C}$  CP/MAS is always an excellent starting point.

In a theoretical study, Marín-Luna et al. studied polymorphism in azoles and benzazoles [121]. The  $^{15}\text{N}$  and  $^{13}\text{C}$  chemical shifts of two azoles and one benzazole were studied by GIPAW DFT. 3(5)-Phenyl-4-bromo-1*H*-pyrazole (2) and 3-phenyl-1*H*(2*H*)-indazole were of interest because they are known to form tautomer crystal polymorphs of one another. The magnetic shieldings for these polymorphs were calculated using GIPAW DFT methods in CASTEP and converted to isotropic chemical shifts by linear regression formulae based on previous literature results. In each case, a noticeable difference was detected in both the  $^{13}\text{C}$  and  $^{15}\text{N}$  chemical shifts between the polymorphs. For example, a peak difference is correlated to position C4' in 3(5)-phenyl-4-bromo-1*H*-pyrazole (5.9 ppm) and for 3-phenyl-1*H*(2*H*)-indazole, a maximum difference is seen at positions C2' and C6' (6.1 ppm). The computed chemical shifts were compared to experimental ones. However, an insufficient agreement between the two meant that the utility of CASTEP with polymorphism resulting from tautomerization was not entirely conclusive. B3LYP/6-311++G(d,p) data were shown to correlate better to the NMR results, showing that periodic calculations, while robust, are more useful when compared to complimentary isolated-molecule predictions.

NMR crystallographic methods inform debates about whether certain polymorphs exist. Frelek et al. employed solid-state NMR methods to characterize the polymorphic forms of finasteride [122], which was suggested to crystallize in up to four different forms, all having been previously described by several different methods. Interestingly, it was suggested by Othman et al. that after storing form I at room temperature for several years, a phase transformation occurs towards a mixture containing form II as well as perhaps an unknown form designated as form X, in addition to form I [123]. It was suggested, at the time, that evidence for form X was manifested through powder X-ray and  $^{13}\text{C}$  CP/MAS, where the X-ray results are similar to form III, but the NMR data differed significantly from the other polymorphs and showed it was unique in that form X only has one molecule of finasteride in the asymmetric unit. Though no isolation of form X was attempted, and little characterization was presented. Frelek et al. employed  $^{13}\text{C}$  and  $^{15}\text{N}$  CP/MAS NMR to describe the elusive polymorph X. However, when form X was extracted from an old sample of form I,

the NMR signals corresponded to form III, which is most likely to contain one molecule of finasteride in its asymmetric unit. Based on their spectral results, it was argued that, in fact, form I does not change its phase to form II and form X, and the unknown polymorph does not exist. Instead, Frelek et al. suggested that the results obtained by Othman were mistakenly attributed due to a signal present at 40.3 ppm resulting from C10 of trace amounts of form I or form II.

### 3.1.2 Conformational polymorphism

Traditional polymorphism has been studied extensively by solid-state NMR, and while this chapter generally only covers a few examples over the last few years, the literature is saturated with examples and approaches to studying polymorphism. A newer area of focus is conformational polymorphism. When the same molecule adopts different conformations in crystal structures, as opposed to different arrangements in crystal packing, it is referred to as conformational polymorphism. Conformational polymorphism is the study of how conformational changes in a molecular structure (e.g. rotations) are related to the stability of a crystal structure [124–126]. Packing polymorphism, on the other hand, is related to molecules that possess high rotational energy barriers and may display only slight differences in their molecular structure geometries from one polymorph to the other, only because of the forces which are generated by the crystal structure. Solid-state NMR spectroscopy is a useful tool for studying conformational polymorphs.

In a comprehensive study, three forms of 4,4'-azobis(3,5-dimethyl-1H-pyrazole) ( $H_2azbpz$ ) (polymorphs I and II and the hemihydrate) were synthesized and analysed by various methods, where NMR was used as a technique for conformational polymorph detection [127]. This set of crystal phases exhibits polymorphism because the molecule tends to adopt different conformers. Azo-bipyrazoles sometimes display *azo-peddling*, which describes the rotation of substituents about the C–N bond or a double proton transfer from N1 to N2, the process proceeding with an activation energy of roughly 10–60 kJ/mol in the solid state. The  $^1H$  NMR data showed similarities between both dehydrated polymorphs, with broad signals appearing at 1.4 and 13.2 ppm; these data alone did not distinguish between the two polymorphs to the level of specificity required. The hemihydrate was differentiated based on the appearance of five distinct signals in the NMR spectrum.  $^1H$ - $^{13}C$  CP/MAS spectra showed a significant difference between the two non-hydrated polymorphs in the region of 120–150 ppm resulting from the slight difference in packing adopted because of the conformational

differences between H<sub>2</sub>azbpz-I and H<sub>2</sub>azbpz-II. The authors measured the hydrogen exchange process in the hemihydrate using <sup>1</sup>H EXSY to yield a rate constant, *k*, of  $342 \pm 34 \text{ s}^{-1}$ .

In another example of conformational polymorphism, solid-state NMR provides critical insights into the nature of the conformational polymorphs of carvedilol (CAR). In an NMR study, Rezende et al. showed the utility of GIPAW DFT as a necessary tool to study these sorts of pharmaceutical polymorphs [128]. CAR is a nonselective beta-blocker that exists in four phases: three anhydrous forms and one hydrous form. The three polymorphs were studied previously in their tablet formulations [129], but the focus here was to characterize CAR II and CAR III. The crystal structures of the known polymorphs of CAR indicate that they are conformational polymorphs, differing only substantially by the conformation of the carbazole-4-yloxy groups of the *S*-enantiomers (see figure 7 of reference [130]). CAR II and CAR III both crystallize in centrosymmetric monoclinic structures with two pairs of enantiomeric molecules in their unit cells. The hydrate comprises two independent molecules of CAR along with a water molecule. <sup>13</sup>C and <sup>15</sup>N MAS NMR experiments were performed alongside GIPAW DFT calculations to assess the differences between the polymorphs and assign their chemical shifts. As it turns out, the quality of the NMR data alone allows for polymorphs II and III to be distinguished, the former featuring a higher degree of crystallinity and easily distinguishable resonances from form III.

Conversely, the hydrate shows higher amorphicity, with some signals broadened and overlapping. The <sup>15</sup>N data shows two distinct molecules of CAR in the unit cell of the hydrate, as evidenced by two pairs of peaks in the  $-348$  and  $-265$  ppm range, resulting from the fact that each nitrogen environment takes part in uniquely defined hydrogen bonds to water. GIPAW DFT aided in unambiguously assigning the solid-state NMR peaks such that this study corrected the previous assignments for 11 peaks in CAR II as compared to the earlier report [129].

### 3.1.3 Detecting polymorphs in pharmaceutical formulations

An important application of solid-state NMR is to identify polymorphs present within a manufactured API formulation. NMR crystallography of Clopidogrel Hydrogensulfate (HSCL), an antiplatelet agent, shows the effectiveness of solid-state NMR for addressing this issue. Pindelska et al. [131] verified the crystal structures of two polymorphs of HSCL (I and II) and performed solid-state NMR analysis on commercially available solid formulations to identify which of the two polymorphs were present in the

drug sample. Dipolar dephased spectra were used to assign  $^{13}\text{C}$  peaks in the CP/MAS spectra though the suppression of signals corresponding to carbons engaged in dipolar interactions with  $^1\text{H}$ . Although dipolar dephasing experiments can successfully pick out specific carbons (such as quaternary carbons) in NMR crystallography [132,133],  $^{13}\text{C}$  spectra can be complicated because of signals that are too broad or overlapped, particularly as the complexity of the crystal structure increases, hindering the utility of dipolar dephasing experiments in peak assignment for complicated molecules. The authors found GIPAW DFT to be more useful in the peak assignment. The critical difference between both polymorphs is the number of molecules in the unit cell where for HSCL 1,  $Z' = 2$ , and for HSCL 2,  $Z' = 1$ , making the identification of each polymorph by  $^{13}\text{C}$  CP/MAS relatively straightforward. It is important to note, however, that the crystal structure of HSCL 1 was of inferior quality, and the calculated results did not agree with the experimental values. The results show that the deposited crystal structure of HSCL 1 is of lower quality than HSCL 2, although the  $R$  factor of HSCL1 is 2.5%, lower than that of HSCL2 at 4.73%, which could imply that its crystal structure is superior. The authors note that the  $R$  factor should be taken as a measure of precision and not accuracy. Therefore, caution is essential when comparing DFT calculated shieldings to experimental results. The experimental results were compared to a series of commercially available pharmaceutical forms of HSCL, and it was determined that in each case, the HSCL 1 polymorph is present, except in PLAVIX<sup>®</sup>, where HSCL 2 is used. This was supported by the fact that they observe the same chemical shifts for the pure forms and the pharmaceutical forms, and also because no phase transitions occur upon the addition of the excipients or the pressurization into the pill form. Interestingly, the excipient content could be verified by  $^{13}\text{C}$  CP/MAS, and the results show that there is a variation of the ingredients that make up the formulations provided by each manufacturer. To summarize, these results indicated that solid-state NMR spectroscopy can quickly determine polymorphs of a particular drug present in a solid dosage, and the authors further suggested that the  $^{13}\text{C}$  CP/MAS spectra could help detect counterfeit pharmaceutical based on the excipient signature present in the spectrum, or by whether phase transitions have occurred.

### 3.1.4 Other examples

An unusual case of polymorphism involves the interconversion of some substances between a salt and a cocrystal [134]. These situations are rare: there are only a few known cases where the same chemical species can crystallize as



one or the other at the same temperature, and in the last couple of years has there been an increase in interest in these peculiar compounds [135–138]. Bernasconi et al. recently discussed one of these examples comprising an adduct of ethionamide and salicylic acid [139] where either liquid-assisted grinding or rapid evaporation selectively produced the salt or cocrystal, respectively. X-ray diffraction results showed that the salt crystallized in a  $P2_1/c$  space group, with one unit each of the cation and anion in the asymmetric unit, whereas the cocrystal crystallized in the  $P2_1/n$  space group with one unit of both molecules present in the asymmetric unit.  $^{15}\text{N}$  CP/MAS provides evidence as to the ionic or neutral charge nature of the compounds. For the salt, N1 exhibited a shift of 211.9 ppm as compared to 309.0 ppm for pure ethionamide, vs a shift to only 273.4 ppm for the cocrystal. The authors noted that based on prior studies [140], these results are consistent with proton transfer and neutral hydrogen bonding, respectively. Bridging N–H distances were extracted from  $^1\text{H}\{^{14}\text{N}\}$  PM-S-RESPDOR experiments, resulting in values of 1.07 Å for the salt and 1.50 Å for the cocrystal, in excellent agreement with a CSD survey of various pyridine–carboxylic acid interactions. The results were supported by DFT calculations, thermal analysis and dissolution kinetic tests, where the thermodynamic phase is the salt, and the kinetic phase is the cocrystal. This study successfully demonstrated that solid-state NMR is useful alongside X-ray diffractions and several other techniques to detect salt–cocrystal polymorphism easily.

One of the biggest problems with drug formulations is excipients, which can hinder the detection of  $^{13}\text{C}$  or  $^1\text{H}$  signals. Typically, nuclei that are not present in an excipient may be utilized to confirm the phase of the API present in a formulation—these include  $^{14}\text{N}$ ,  $^{15}\text{N}$ ,  $^{19}\text{F}$ ,  $^{35}\text{Cl}$ —but more time or specialized equipment may be needed to acquire these spectra, which are also often more challenging to decipher. There has been a significant amount of work put into developing methods of signal detection to efficiently observe NMR signals to detect and determine which API is present in a particular drug formulation.

While spin-1/2 nuclei have been used widely in NMR crystallography and to study polymorphism, quadrupolar nuclei have been used less frequently. Nevertheless, they have the potential to be very useful in differentiating or validating crystal structures because of the high sensitivity of the quadrupolar interaction to the local chemical environment. To this end, the quadrupolar coupling constant and the quadrupolar asymmetry parameter are sensitive probes of polymorphism. Nuclei such as  $^{14}\text{N}$ ,  $^{35}\text{Cl}$ ,  $^{23}\text{Na}$ ,  $^{17}\text{O}$ , and others, have been applied to solid-state NMR investigations of various materials, including glasses, metal–organic frameworks and other solids [141].



$^{43}\text{Ca}$  ( $I = 7/2$ ) has been used often in efforts related to NMR crystallography [142–147] due to the sensitivity of its central transition line to the crystal structure. Ca is also highly abundant on earth and is found in the makeup of geological materials, is used in catalysis, and in some biological processes. A 2014 paper by Widdifield et al. [142] demonstrated the utility  $^{43}\text{Ca}$  NMR experiments as a probe for distinguishing between polymorphs containing  $^{43}\text{Ca}$ . A summary of the GIPAW DFT calculated NMR parameters is shown in Table 1.

A real test of the utility of  $^{43}\text{Ca}$  NMR in NMR crystallography was provided by Burgess and Bryce, whereby the correct space group of the vaterite polymorph of  $\text{CaCO}_3$  was narrowed down from an extensive list of proposed crystal structures with different space groups, suggesting vaterite as being either the  $P3_221$  or  $C2$  structures [145].  $^{43}\text{Ca}$  NMR has also been used to study the structures of  $\text{CaC}_2\text{O}_4 \cdot \text{H}_2\text{O}$  [148],  $\text{Ca}_{10}(\text{PO}_4)_6(\text{OH})_2$  [143], calcium benzoate trihydrate [144] and others (a full account on the subject can be read in a 2017 review by Widdifield [147]).

A recent paper by Holmes et al. proposed a new  $^{43}\text{Ca}$  NMR method for determining the local calcium structure by studying atorvastatin calcium trihydrate form I (ATC-1), an API used in the treatment of high cholesterol [149]. This is a follow-up to a previous report detailing the solid-state NMR of ATC-1 by  $^{13}\text{C}$ ,  $^{19}\text{F}$  and  $^{15}\text{N}$  NMR [146]. They found that ATC-1 contains a single  $^{43}\text{Ca}$  site with  $C_Q = 1.81 \pm 0.15 \text{ MHz}$  and  $\eta = 0.44 \pm 0.13$ . From the EFG and CS tensor magnitudes along with the Euler angles, the authors derived information about the local Ca environment including its coordination number and the various bond angles based on an assumption that the Ca centre will have a chemical environment similar to those found in the CSD, grouped into 14 distinct motifs. The structures found in the CSD served as models with which to compare the experimental NMR data. The coordination environment can be further optimized by simulating the effects of changing the Euler angles. A visualization of the proposed Ca centre of ATC-1 and the dependence of the  $^{43}\text{Ca}$  line shape on the EFG tensor parameters are shown in Fig. 7. This research showed that the NMR parameters can be used to establish structural constraints at the  $^{43}\text{Ca}$  nucleus to gain information about the conformational nature of a polymorph. The method gave rise to information that can be used to generate crystal structures predicted *via* computational approaches.

Metal squarates, incorporating oxocarbon 3,4-dihydroxy-3-cyclobutene-1,2-dione (squaric acid), occur when  $\text{C}_4\text{O}_4^{2-}$  acts as a bridging molecule between metal centres in these structures.  $\text{Pb}^{\text{II}}$  can form several squarate polymorphs that differ in the arrangement of the  $\text{C}_4\text{O}_4^{2-}$  coordinating

**Table 1** GIPAW DFT computed  $^{43}\text{Ca}$  EFG and chemical shift tensor parameters for various calcium-containing systems.

Compound	$ C_Q(^{43}\text{Ca}) /\text{MHz}$	$\eta_Q$	$\delta_{\text{iso}}/\text{ppm}$	$\Omega/\text{ppm}$	$\kappa$	$\alpha, \beta, \gamma/^\circ$
$\text{Ca}(\text{OH})_2$	2.28	0.000	71.9	38.5	-0.998	30.1, 90.0, 0.1
$\alpha$ -Calcium formate	1.41	0.899	14.1	29.6	-0.190	97.7, 74.9, 251.1
$\beta$ -Calcium formate	2.86	0.342	-1.6	40.8	0.094	270.0, 65.3, 0.0
Calcium tartrate $\cdot 3\text{H}_2\text{O}$	1.73	0.499	25.5	36.5	-0.072	174.9, 5.1, 290.9
(+)-Calcium tartrate $\cdot 4\text{H}_2\text{O}$	1.14	0.628	5.4	30.0	-0.205	121.4, 75.2, 298.7
( $\pm$ )-Calcium tartrate $\cdot 4\text{H}_2\text{O}$	0.99	0.713	4.4	17.0	0.497	245.8, 67.9, 62.6
Calcium acetate $\cdot \text{H}_2\text{O}$ (1984)	1.92	0.366	-7.0	38.7	-0.666	280.1, 87.2, 345.2
	1.35	0.080	17.7	22.7	-0.367	99.5, 88.9, 184.4
$\text{CaCl}_2$	0.98	0.541	67.7	52.7	-0.24	90.0, 89.4, 0.0
$\text{CaCl}_2 \cdot 2\text{H}_2\text{O}$	3.34	0.187	63.6	25.5	0.296	180.0, 84.6, 180.0
$\text{CaCl}_2 \cdot 6\text{H}_2\text{O}$	0.32	0.000	-27.3	9.2	-0.999	29.8, 90.0, 178.7
$\text{CaCO}_3$ , calcite	1.47	0.00	22.7	10.8	1.00	0.0, 0.0, 0.0
$\text{CaCO}_3$ , aragonite	0.32	0.58	-27.1	52.2	0.49	0.0, 15.0, 90.0
$\text{CaSO}_4 \cdot 2\text{H}_2\text{O}$	1.45	0.999	-19.8	57.6	-0.441	270.0, 89.7, 180.0
$\text{CaCrO}_4$	1.35	0.000	-62.7	85.8	-1.000	90.0, 90.0, 180.0
$\text{CaTiO}_3$	1.97	0.683	19.3	69.6	0.420	90.0, 3.4, 0.0
$\text{Ca}(\text{NO}_3)_2$ (original)	3.48	0.000	-49.3	39.4	1.000	2.9, 0.0, 90.1
$\text{Ca}(\text{NO}_3)_2$ (N, O optimized)	2.72	0.000	-61.0	27.6	1.000	1.8, 0.0, 180.0
$\text{CaH}_2$	1.14	0.849	120.1	35.3	0.449	270.0, 13.6, 180.0

C.M. Widdifield, I. Moudrakovski, D.L. Bryce, Calcium-43 chemical shift and electric field gradient tensor interplay: a sensitive probe of structure, polymorphism, and hydration, Phys. Chem. Chem. Phys. 16 (2014) 13340–13359. <https://doi.org/10.1039/C4CP01180E>.

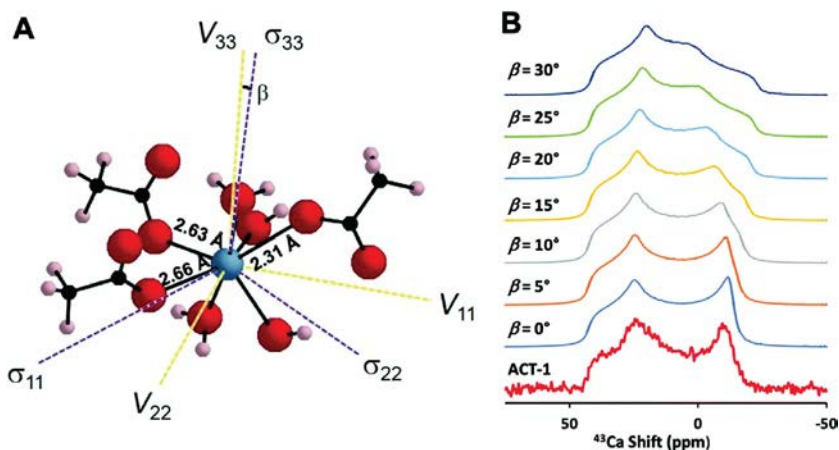


**Fig. 7** (A) The proposed structure of ATC-I. (B) Variation of crystallographic parameters of ATC changes the  $^{43}\text{Ca}$  line shapes considerably in comparison to the experimental  $^{43}\text{Ca}$  pattern obtained at 19.97 T (red). From S.T. Holmes, W.D. Wang, G. Hou, C. Dybowski, W. Wang, S. Bai, A new NMR crystallographic approach to reveal the calcium local structure of atorvastatin calcium, *Phys. Chem. Chem. Phys.* 21 (2019) 6319–6326. <https://doi.org/10.1039/C8CP07673A>. Used with permission.

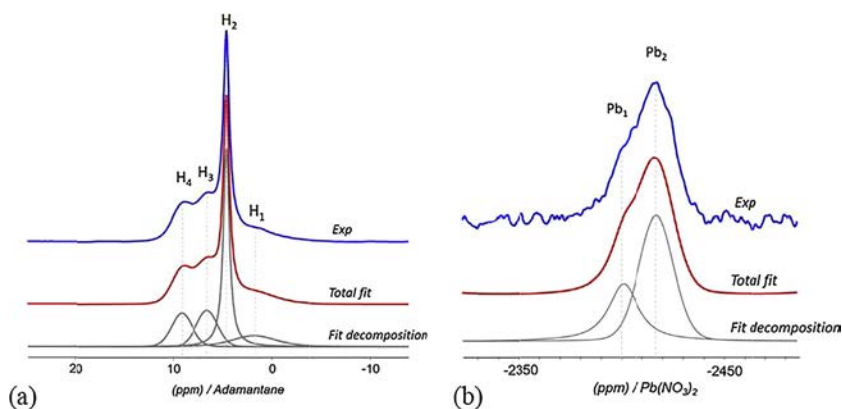


**Fig. 8**  $^1\text{H}$  (A) and  $^{207}\text{Pb}$  (B) NMR spectra, including fits (the main fit is shown in red, and the deconvolution in grey), of  $\text{Pb}(\text{H}_2\text{O})(\text{C}_4\text{O}_4)$ . From T. Bataille, A. Bouhali, C. Kouvas, C. Trifa, N. Audebrand, C. Boudaren, Hydrates and polymorphs of lead squarate  $\text{Pb}(\text{C}_4\text{O}_4)$ : structural transformations studied by in situ X-ray powder diffraction and solid state NMR, *Polyhedron* 164 (2019) 123–131. <https://doi.org/10.1016/j.poly.2019.02.047>. Used with permission.

the lead centres. Solid-state NMR provides a suitable method for exploring the coordination of these  $\text{Pb}^{\text{II}}$  sites, as presented by Bataille et al. in a 2019 study [150]. In this work,  $^1\text{H}$  and  $^{207}\text{Pb}$  solid-state NMR experiments were performed on a new polymorph of lead squarate (Fig. 8),  $\text{Pb}(\text{H}_2\text{O})(\text{C}_4\text{O}_4)$ .

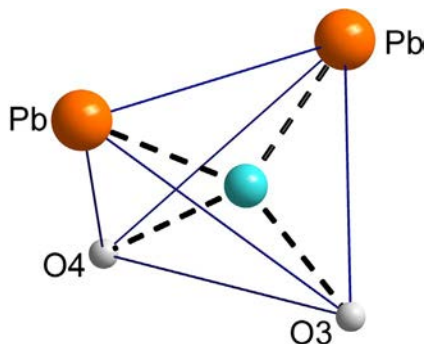


**Fig. 9** Tetrahedral environment of the water ( $O_w$ ) atom. Each corner oxygen atom is situated at two different distances from their related corner Pb atoms, leading to four Pb-O distances to form the tetrahedron. As a result, each water H atom between  $O_w$  and O3 and  $O_w$  and O4 should be sensitive to two Pb environments, giving rise to four  $^1\text{H}$  NMR signals. From T. Bataille, A. Bouhali, C. Kouvas, C. Trifa, N. Audebrand, C. Boudaren, *Hydrates and polymorphs of lead squarate  $\text{Pb}(\text{C}_4\text{O}_4)$ : structural transformations studied by in situ X-ray powder diffraction and solid state NMR*, *Polyhedron* 164 (2019) 123–131. <https://doi.org/10.1016/j.poly.2019.02.047>. Used with permission.

The  $^1\text{H}$  data showed four isotropic signals at 1.75, 4.56, 6.53 and 9.10 ppm, suggesting four inequivalent  $^1\text{H}$  sites. However, the picture is completed when the  $^{207}\text{Pb}$  NMR spectra are taken into account. Here, two distinct sites ( $\delta_{\text{iso}} = -2401$  and  $-2417$  ppm) were observed with a ratio of 70:30 in terms of their integrated intensities, which shows two discrete  $\text{Pb}^{\text{II}}$  sites coordinating each differently to water and the oxygen in squarate (Fig. 9). This difference in the shift data corresponds to a Pb–O length difference of  $0.0018 \text{ \AA}$ , which would not be apparent in X-ray crystallography, but is clearly discernable by solid-state NMR. The data corroborated the  $^1\text{H}$  data, suggesting four different Pb–H distances. The data enabled the calculation of Pb–O and Pb–H distances existing in the crystal structure, which cannot always be obtained easily using X-ray data.

Our laboratory studied  $\text{Pb}^{\text{II}}$  isonicotinoyl hydrazone solvates in the context of their  $\text{Pb}^{\text{II}}$  coordination environment and their ability to form tetrel bonds [151]. The primary purpose of this paper was related to the utility of solid-state NMR spectroscopy for studying noncovalent interactions with Pb. It does, however, also serve as an example where different species can be differentiated based on specific signatures related to bonding environments at sites where nuclei are particularly susceptible to minor changes not always evident in X-ray crystallographically determined structures. In the paper, 2-pyridinecarbaldehyde isonicotinoyl hydrazine (L1) and 2-acetylpyridine

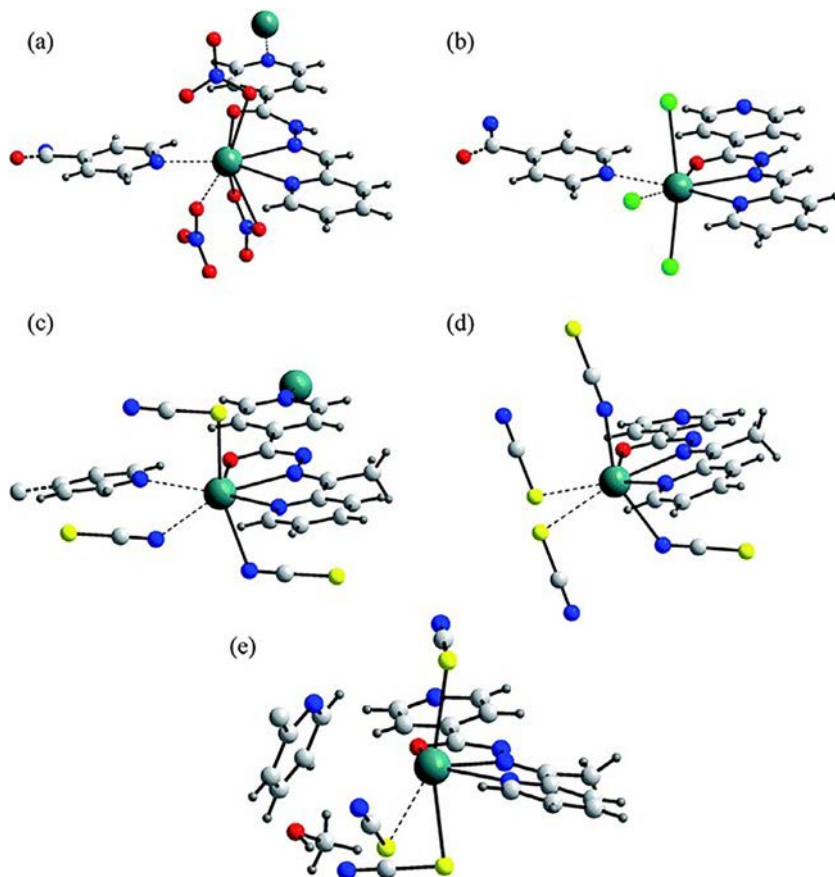


**Fig. 10** Models of the  $\text{Pb}^{\text{II}}$  isonicotinoyl hydrazone compounds studied showing the acceptor molecules adjacent to the open face of the hemidirected  $\text{Pb}(\text{II})$  centres. (A and B) L1-containing compounds, (C–E) L3-containing compounds. Reproduced from S.A. Southern, D. Errulat, J.M. Frost, B. Gabidullin, D.L. Bryce, *Prospects for  $^{207}\text{Pb}$  solid-state NMR studies of lead tetrel bonds*, *Faraday Discuss.* 203 (2017) 165–186. <https://doi.org/10.1039/C7FD00087A>, with permission from The Royal Society of Chemistry.

isonicotinoyl hydrazone (L3) were subjected to recrystallization in the presence of  $\text{Pb}(\text{NO}_3)_2$  and  $\text{PbCl}_2$ , resulting in two crystal structures featuring L1, or  $\text{Pb}(\text{SCN})_2$  in the presence of different solvents resulting in three polymorphs including L3 (Fig. 10). In all five compounds, a consistent pattern of five bonds to lead is observed and differentiated based on the Pb–N, Pb–O, or Pb–S bond distances.  $^{207}\text{Pb}$  NMR provides key information about the local environments surrounding the  $\text{Pb}^{\text{II}}$  centres, particularly about whether the

geometries are hemidirected (open on one face), holodirected (spherically coordinated) or somewhere in between. Spans of roughly 1000 ppm correspond to holodirected geometry, whereas spans >2000 ppm reflect hemidirected geometry. The skews provide more information about each geometry showing some structures falling within the ranges observed for holodirected geometries (<0.55) or hemidirected geometry (>0.6). Compounds c and d (Fig. 10) are interesting in that they feature spans consistent with hemidirected geometry, but skews more consistent with holodirected geometry. Compounds that have NMR responses consistent with holodirected geometry (a and b) were concluded to possess strong tetrel bonds to  $\text{Pb}^{\text{II}}$  where the bond length is less than the sum of their van der Waals radii. In contrast, compounds with NMR responses strictly associated with hemidirected geometry (c and e) were presumed to feature weak tetrel bonds. The NMR data can also indicate an intermediate situation (d) when a mixture of signatures for both geometries were observed (Fig. 11).

### 3.2 Probing non-covalent bonding in solids

Another important aspect of NMR crystallography is the study of non-covalent interactions. Understanding inter- and intramolecular interactions is a fundamental practice of NMR crystallography because they influence the formation of a periodic crystal structure to varying degrees depending on their bond strengths. Conversely, understanding bonding is equally vital as it contributes directly to the understanding of conformational polymorphism and dynamics. Solid-state NMR provides observables that can be related to the electronic properties of nuclei as they interact with other atoms. The chemical shift, the quadrupolar interaction, dipolar coupling, and  $J$ -coupling may be used to understand the nature of bonding and noncovalent interactions. For example, an effort will be made here to summarize the relationship between NMR crystallography and noncovalent interactions, but we direct the reader to other manuscripts that discuss this subject at length [152,153].

Hydrogen bonds [154] are likely the most studied of the noncovalent interactions by NMR spectroscopy as they are probably the most well-known and are important in several applications such as crystal engineering, biological process, catalysis and materials science. Interactions such as  $\pi$ - $\pi$ , cation- $\pi$  and anion- $\pi$  play an essential role in guiding crystallization (for an exciting look at the role of  $\pi$ - $\pi$  stacking in crystal engineering, see a recent virtual issue of Crystal Growth and Design [155]). Beyond that, an effort has

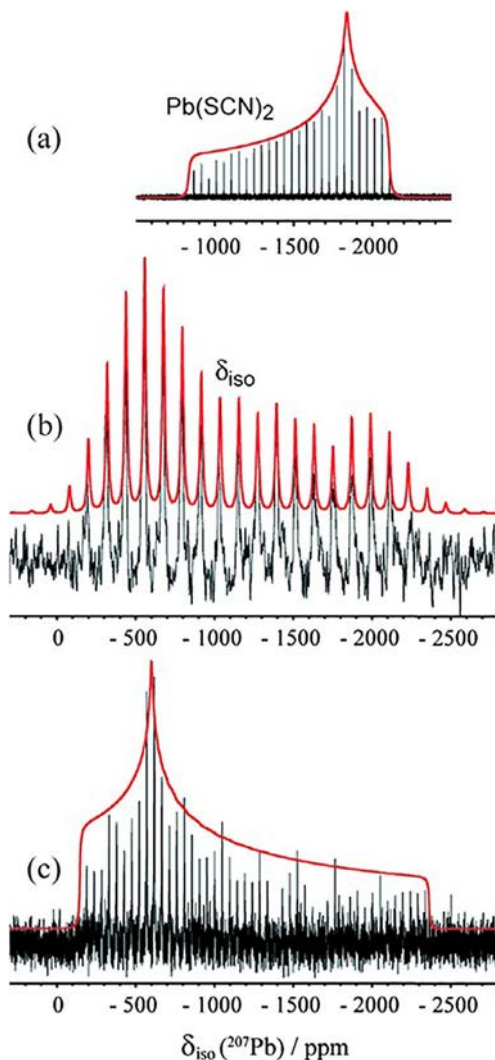


**Fig. 11** (A)  $^{207}\text{Pb}$  static CPMG spectrum of the starting material  $\text{Pb}(\text{SCN})_2$ . (B and C) MAS (5000 Hz) and stationary  $^{207}\text{Pb}$  CPMG spectra of  $\text{Pb}(\text{L3})(\text{SCN})_2$ . The spectrum implies an intermediate case between hemidirected and holodirected geometry because the chemical shift falls between those typical of both. *Reproduced from S.A. Southern, D. Errulat, J.M. Frost, B. Gabidullin, D.L. Bryce, Prospects for  $^{207}\text{Pb}$  solid-state NMR studies of lead tetrel bonds, Faraday Discuss. 203 (2017) 165–186. <https://doi.org/10.1039/C7FD00087A>, with permission from The Royal Society of Chemistry.*

been made to understand the hydrogen bond and its effect on NMR chemical shifts [156–159]. X-ray crystallography can play an essential role in identifying hydrogen bonds and their geometries, but cannot always determine hydrogen atom positions with high accuracy. Solid-state NMR alongside GIPAW DFT methods can confirm hydrogen bond lengths using dipolar coupling measurements (described in Section 2.2).

Analogous to hydrogen bonds are  $\sigma$ -hole interactions. These involve the attractive interaction between the electrophilic region of a donor atom ( $\sigma$ -hole) and an electron-rich acceptor [160]. These sorts of interactions are named after the group in the periodic table (groups 14–17) to which the electrophilic atom belongs [161]. Examples of  $\sigma$ -hole interactions include halogen (XB) [162], chalcogen (ChB) [163], pnictogen (PnB) [164], and tetrel (TB) [165] bonds. Even the term ‘aerogen bond’ [166] has been coined for the noble gases.

In a computational study, Lu and Scheiner [167] suggested that the NMR signal for donor nuclei involved in noncovalent interactions exhibit consistent spectroscopic changes: first, the covalent bond is weakened and shows an IR redshift because of the bond stretching; second, the magnetic shielding of the electrophile increases while that of the electron donor decreases; third, the relative magnitude of the changes follow periodic trends. In a recent advance on the understanding of chalcogen bonding, Kumar et al. showed the utility of both solid-state NMR and vibrational spectroscopy for studying chalcogen bonds [168]. In their work,  $^{77}\text{Se}$  CP/MAS spectroscopy was performed at 9.4 T ( $\nu_{\text{L}}(^{77}\text{Se}) = 76.311$  MHz). They showed the Se chemical shift tensor to be connected to the geometry at the site of the chalcogen bond. On cocrystal formation, they found the isotropic chemical shift to generally decrease. In particular,  $\delta_{11}$  of  $^{77}\text{Se}$  increases for nitrogen-based donors (increase in span), but decreases when the donor is a halide ion (reduction in span).  $\delta_{33}$  was found to decrease generally. Notably, the authors also reported some  $^{125}\text{Te}$  CP/MAS data; however, because of the stability of the complexes, the NMR data could not be obtained for all the cocrystals. In a related study, Kumar et al. probed double chalcogen bonds present in a series of 12 cocrystals [169].  $^{77}\text{Se}$  and  $^{125}\text{Te}$  NMR confirmed the correlation between chalcogen bond geometry and chemical shift tensor data. This can be measured by the span and arises because of the contribution of the Ch–N bonding orbitals to the chemical shift tensor. Along with chalcogen bonding, solid-state NMR has provided useful contributions to understanding pnictogen bonding via  $^{209}\text{Bi}$ – $^{31}\text{P}$   $J$ -coupling [170].



Single-crystal solid-state NMR studies have been useful but under-used in providing critical insights into noncovalent bonding. For these studies, suitably sized crystals are grown and mounted on a goniometer fixed in a solid-state NMR probe. Throughout the NMR analysis, the sample is rotated stepwise to record the magnitude of the NMR interaction tensors and their orientation with respect to the molecular frame. The information obtained from these experiments can give rise to a greater understanding of the nature of noncovalent interactions, translating to a greater appreciation of the guiding forces in crystallization processes.

Past single-crystal NMR studies have looked at hydrogen bonding, both directly [171–173] and indirectly [174–176]. Recently, the method was used to study halogen bonds [177] by  $^{31}\text{P}$  and  $^{17}\text{O}$  NMR at 9.4 T ( $\nu_{\text{L}}(^{31}\text{P}) = 161.976\text{ MHz}$ , ( $\nu_{\text{L}}(^{17}\text{O}) = 54.243\text{ MHz}$ ). Three cocrystals that feature halogen bonds involving  $^{17}\text{O}$ -enriched  $\text{Ph}_3\text{P}^{17}\text{O}$  acceptors were studied. The single-crystal NMR data were used to obtain exact measurements of the  $^{17}\text{O}$  and  $^{31}\text{P}$  chemical shift and EFG tensors to be related to structural features across the halogen bond (Fig. 12). It was found that the direction of both the unique components of the  $^{31}\text{P}$  and  $^{17}\text{O}$  CS tensors and the  $^{17}\text{O}$  quadrupolar coupling tensor were dependent on the linearity of the halogen bond, while the magnitude of these interactions is also sensitive to the halogen bond formation. The spectra further revealed that upon halogen bond formation,  $\mathbf{J}(^{31}\text{P}, ^{17}\text{O})$  tensor asymmetry increases from 0.43 to 0.47, while the magnitude of anisotropy of  $\mathbf{J}$  decreases from  $-512$  to  $-281\text{ Hz}$ . The study provides insights into the NMR response upon halogen-bond induced cocrystallization.

### 3.3 Dynamic processes

#### 3.3.1 *In situ monitoring of crystallization processes*

Much interest has been directed towards monitoring crystallization processes *in situ*. Up to recently, it has been challenging to watch the dynamics of crystallization directly while it occurs. To this end, techniques have been developed to overcome this challenge. Inferences are usually made based on observations before and after crystallization. One challenge with *in situ* monitoring of reactions is that it is difficult to sample the progress uniformly. Often, reactions are stopped momentarily to be analyzed by X-ray diffraction or NMR, then resumed. A variety of techniques for monitoring reactions *in situ* by NMR using non-uniform sampling have emerged to help



ease the challenges of time-resolved NMR spectroscopy [178]. However, *in situ*, solid-state NMR is a technique that has shown great potential for monitoring crystallization processes in real-time.

Recently, Friščić et al. have made much progress in monitoring the crystallization of organic molecules and metal-organic frameworks *in situ* by diffraction methods [179–185] or Raman spectroscopy [186,187]. Batzdorf et al. combined both methods in a 2014 paper monitoring several milling reactions [188]. Several studies were successful in demonstrating the usefulness of this approach. Harris et al. were particularly successful in this endeavour, where they described *in situ* monitoring of the crystallization of glycine from solution, the crystallization of a cocrystal of caffeine and malonic acid [189], the discovery of new polymorphs [190], and the development of methods for dealing with *in situ* monitoring of crystallization [191,192]. An excellent summary of their work dealing with *in situ* monitoring of crystallization processes by solid-state NMR can be read in a 2015 review [193].

In a more recent study, Cerreia-Vioglio et al. characterized the crystallographic evolution process of glycine dihydrate, discovered by Xu et al. [194], by *in situ* solid-state NMR to further understand the evolution of this elusive phase of glycine [195]. In their study, aqueous glycine is quenched, frozen, then warmed to 209 K inside the NMR spectrometer to yield glycine dihydrate (GDH), in a procedure similar to the benchtop.  $^1\text{H}$ - $^{13}\text{C}$  CPMAS spectra recorded as a function of temperature shows the conversion of an aqueous glassy phase of glycine to a phase with a chemical shift of 173.5 ppm (Fig. 13A), which differs from the  $\alpha$ -,  $\beta$ - or  $\gamma$ - polymorphs of glycine (which over time end up converting to the  $\beta$  phase). They also observed this result *via* a  $^1\text{H}$ - $^{15}\text{N}$  CP/MAS measurement. Two-dimensional  $^1\text{H}$ - $^{13}\text{C}$

**Fig. 12**  $^{31}\text{P}$  (Top, (A)) and  $^{17}\text{O}$  (middle, (B)) single-crystal NMR spectrum of  $(\text{Ph}_3\text{PO}) (\text{p-C}_6\text{F}_4\text{I}_2)$  obtained following rotations in  $9^\circ$  increments about the X, Y, and Z axes and showing only every other spectrum. (Bottom, (C)) Visualization of the crystal structure of the starting material in different orientations (a,c) and its halogen-bonded cocrystal (b,d). The  $^{31}\text{P}$  CS principal components are indicated by dark green vector lines in the top panel, and the  $^{17}\text{O}$  CS components are illustrated as dark green vectors in the bottom panel. The quadrupolar coupling tensors are indicated as pink vectors in the molecular frame. The green and orange arrows indicate the direction of  $\delta_{33}(^{31}\text{P})$ ,  $\delta_{11}(^{17}\text{O})$ , and  $Q_{33}$  movement, respectively, when the XB interaction is present. Illustrating the change of direction of the vectors, the insets show the projection of the structures when the  $\text{P}=\text{O}$  bond is in the plane. Adapted with permission from Y. Xu, B. Gabidullin, D.L. Bryce, *Single-crystal NMR characterization of halogen bonds*, *J. Phys. Chem. A* 123 (2019) 6194–6209. <https://doi.org/10.1021/acs.jpca.9b03587>. Copyright 2019 American Chemical Society.

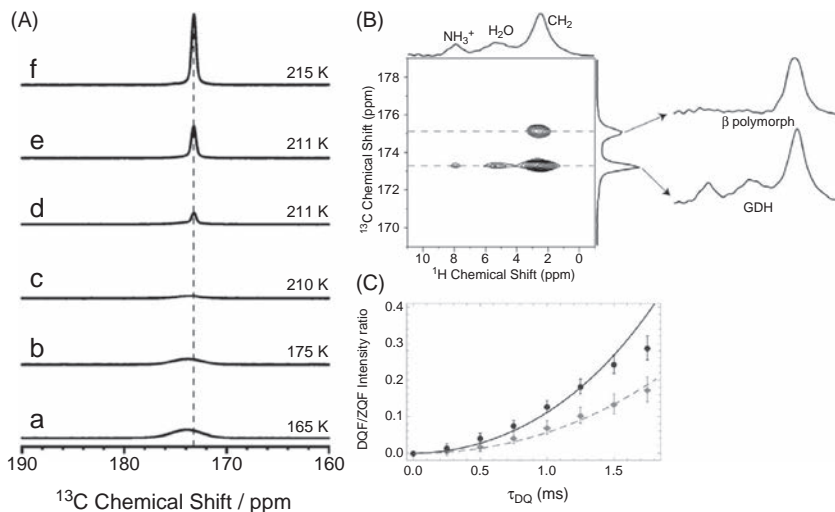


**Fig. 13** (A) Stacked  $^1\text{H}$ - $^{13}\text{C}$  CP/MAS NMR spectra for a solution of  $1\text{-}^{13}\text{C}$ -glycine, increasing in temperature from 145 to 215 K. The figure shows the formation of glycine dihydrate as the solution warms (B)  $^1\text{H}$ - $^{13}\text{C}$  HETCOR spectrum recorded at 212 K following a flash cooling. The spectrum shows a correlation to water, indicating the formation of glycine hydrate. Also, some transformation to  $\beta$  polymorph is seen to have occurred. (C)  $^{13}\text{C}$ - $^{13}\text{C}$  DQF/ZQF dipolar build-up curves for  $^{13}\text{C}$  labelled glycine dihydrate ( $\blacklozenge$ ) and the labelled  $\alpha$  polymorph ( $\bullet$ ). The curves are plotted in comparison to the theoretical DQF/ZQF dipolar build-up curves calculated for the crystal structures of glycine dihydrate (grey dashed line) and the  $\alpha$  polymorph (black line). From P. Cerreia Vioglio, G. Mollica, M. Juramy, C.E. Hughes, P.A. Williams, F. Ziarelli, S. Viel, P. Thureau, K.D.M. Harris, *Insights into the crystallization and structural evolution of glycine dihydrate by in situ solid-state NMR spectroscopy*, *Angew. Chem. Int. Ed.* 57 (2018) 6619–6623. <https://doi.org/10.1002/anie.201801114>. Used with permission.

and  $^1\text{H}$ - $^{15}\text{N}$  HETCOR experiments were used to investigate the hydrogen bonding network of glycine dihydrate. In the  $^{13}\text{C}$  HETCOR spectrum, correlations were observed between water and the  $\text{CO}_2^-$  group of glycine, whereas none was observed for the  $\beta$  phase (Fig. 13B). The  $^1\text{H}$ - $^{15}\text{N}$  HETCOR spectrum shows evidence of water correlating with the  $\text{NH}_3^+$  group of glycine.  $^{13}\text{C}$ - $^{13}\text{C}$  dipolar coupling of  $1\text{-}^{13}\text{C}$ -glycine was measured using a build-up curve in comparison with that of  $\alpha$ -glycine (Fig. 13C), showing that the intermolecular  $^{13}\text{C}$ - $^{13}\text{C}$  dipolar coupling depends on the particular chemical structure of the hydrate because of an intervening water molecule. The results definitively confirmed the structural characteristics of glycine dihydrate that were identified previously.

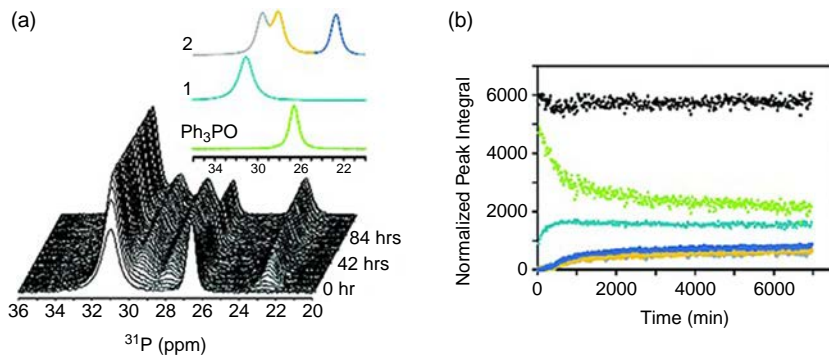


**Fig. 14** (A) *In situ*  $^{31}\text{P}$  CP/MAS (10 kHz) SSNMR spectra of  $\text{Ph}_3\text{PO}$  and  $p\text{-C}_6\text{F}_4\text{I}_2$  reacting in the MAS rotor at a measured temperature of 308 K at 9.4 T. (B) A better visualization of the data is obtained when the peak integrals are integrated, normalized and plotted against time. The colour code is shown on the inset in panel (A), and the black is the sum of the integrations showing that no other species are produced. Reproduced from Y. Xu, L. Champion, B. Gabidullin, D.L. Bryce, *A kinetic study of mechanochemical halogen bond formation by *in situ*  $^{31}\text{P}$  solid-state NMR spectroscopy*, *Chem. Commun.* 53 (2017) 9930–9933. <https://doi.org/10.1039/C7CC05051H>, with permission from The Royal Society of Chemistry.

In another interesting example of *in situ* monitoring of crystallization, a 2017 paper by Xu et al. presented an *in situ* kinetic analysis of the mechanochemical formation of halogen bonded cocrystals of triphenylphosphine oxide ( $\text{Ph}_3\text{PO}$ ) and *para*-diiodotetrafluorobenzene ( $p\text{-C}_6\text{F}_4\text{I}_2$ ) using  $^{31}\text{P}$  solid-state NMR [196]. Here, the mechanochemical reaction occurs in the NMR sample holder while subjected to cross-polarization magic angle spinning. Spectra were recorded every 16 min with eight scans over a few days. The results shown in Fig. 14 illustrate the formation of the cocrystals 1 and 2 occurring in the first 2000 min. These data were simulated with a kinetic model to produce rate constants associated with the reaction at different spinning speeds ranging from  $(0.193 \pm 0.003) \times 10^{-3} \text{ min}^{-1}$  at 8 kHz MAS to  $(0.263 \pm 0.00) \times 10^{-3} \text{ min}^{-1}$  at 12 kHz MAS, showing that the reaction is diffusion controlled.

In a related approach, Ivanova et al. [197] provided a fascinating study of the nucleation and growth of zeolite BEA by *in situ*  $^{13}\text{C}$ ,  $^{29}\text{Si}$ ,  $^{23}\text{Na}$  and  $^{27}\text{Al}$  MAS NMR. The data provide insights into how  $\text{TEA}^+$  is involved in the nucleation and crystallization of zeolite BEA in two synthesis pathways that were tested in this study.  $^{29}\text{Si}$  and  $^{27}\text{Al}$  NMR provide information about how silicate and aluminosilicate species, along with Al cations,

transform into the zeolite, while  $^{13}\text{C}$  data provided insight into how the organic structure-directing agent is involved in the zeolite's crystallization. Their study demonstrates the power of solid-state NMR spectroscopy for monitoring zeolite formation and for the elucidation of its step-by-step mechanism, and could be extended to similar species such as metal-organic frameworks.

### 3.3.2 Mechanochemistry

Mechanochemistry is the study of solid-state chemical changes resulting from energy input derived from mechanical processes. The benefit of mechanochemistry is that often chemical reactions can proceed in the absence of excess solvents or heating, making this a key component in the recent uptick of interest in green chemistry. Solid-state NMR studies of mechanochemically formed cocrystals have been popular in the last number of years. The formation of a bulk powder of racemic praziquantel hemihydrate in a vibrational mill was investigated in an elaborate study by Zanolla et al. [5], showing how mechanochemistry can be practical for, and sometimes the only way, to access new polymorphs. For example, Xu et al. observed the formation of mechanochemically induced halogen bonded solids featuring  $\text{P}=\text{O}-\text{I}-\text{C}$  motifs by observing  $^{31}\text{P}-^{17}\text{O}$   $J$ -coupling [198]. In another example by Peach et al. [199], co-crystals of fluoxetine hydrochloride and benzoic acid, fumaric acid and succinic acid were prepared by liquid-assisted and neat grinding and analyzed by  $^{35}\text{Cl}$  solid-state NMR. Their study showed that grinding can yield API co-crystals with higher purity, and that  $^{35}\text{Cl}$  is particularly well suited for detecting the differences between the cocrystals and the respective starting materials due to the high sensitivity of  $^{35}\text{Cl}$  to the hydrogen bonding environment surrounding the chloride ion. Mechanochemistry was also used to prepare anion coordinated architectures based on 3-iodoethynyl pyridine and 3-iodoethynylbenzoic acid and subsequently studied by solid-state NMR to characterize their presence [259].

An interesting use of mechanochemistry in NMR crystallography is the isotropic labelling of compounds. Laurencin et al. have been active in this area, having demonstrated the feasibility of  $^{17}\text{O}$  labelling by mechanochemical methods [200,201]. One of the significant problems associated with  $^{17}\text{O}$  labelling is the high cost of  $^{17}\text{O}$ -enriched water. Métro et al. successfully demonstrated fast and low-cost ( $\sim 135\text{€}$ ) approaches for  $^{17}\text{O}$  enrichment of metal hydroxides, carboxylic acids, and other important compounds [200]. For example, ibuprofen was  $^{17}\text{O}$ -enriched for the first time in the

presence of only 1.5 equivalents of  $\text{H}_2^{17}\text{O}$ , and under ball milling for 5 min, resulting in approximately 8% enrichment per carboxylic acid oxygen. The  $^{17}\text{O}$  MAS spectrum was obtained in <2 h of acquisition. The impact of this work is that  $^{17}\text{O}$  NMR becomes more accessible for just about any organic or inorganic compound of interest due to the low cost of enrichment. In their recent paper, Chen et al. reported new and easy ways to  $^{17}\text{O}$  label metal oxides [201].

Over several years, metal-organic frameworks have become a popular topic of research due to their versatile applicability in areas such as gas absorption or catalysis [202–208]. The goal is to produce clean technologies using MOFs but one of the biggest challenges is the clean synthesis of MOFs themselves [209,210]. O’Keefe et al. recently combined mechanochemical synthesis and multinuclear NMR crystallography to fully characterize cadmium-based MOFs [211]. Their method makes use of accelerated aging, that is, to promote spontaneous formation of the MOF using minimum amounts or reagents under moderate conditions, such as ball milling.

Mechanochemistry can also be applied to crystalline samples to induce phase changes in the crystal structure. Most times, particular polymorphs of solid samples can only crystallize under the conditions provided through mechanochemistry. Acting like an ‘on/off’ switch, it is even possible to get different polymorphs at distinct time points during a mechanochemical reaction. One example of such a process is by mechanical grinding. In one case, barbituric acid in its trioxo form (polymorph II) was ground, solvent-free, in a mechanochemical mill for 24 h to isolate a previously unidentified phase known as a trihydroxyl isomer. The new trihydroxyl barbituric acid phased was confirmed and characterized by CP/MAS,  $^1\text{H}$ - $^{13}\text{C}$  FSLG-HETCOR, showing significant differences in the chemical shifts owing to changes in the hybridization and the hydrogen bonding network present at various  $^{13}\text{C}$  sites in the molecule because of keto-enol conversions [212]. Indeed,  $^{13}\text{C}$  and  $^{15}\text{N}$  CP/MAS can be used to identify further differences in the other known polymorphs of the related crystal structures of thiobarbituric acid [213] and barbital [214].

### 3.3.3 Dynamic processes

There are many examples in the literature where dynamic processes are monitored by solid-state NMR. For instance, Szell et al. recently investigated a case in which a halogen bonding can affect the methyl group dynamics of 2,3,5,6-tetramethylpyrazine (TMP) [3]. In their study, they analyzed



the  $^2\text{H}$  solid-state NMR spectra of eight compounds featuring TMP in participating in halogen bonds or hydrogen bonds with various donor molecules.  $^2\text{H}$  NMR is useful because the spectrum is profoundly affected by dynamic motion and can probe the changes in methyl group rotations located next to the sites of the non-covalent interactions.  $^2\text{H}$   $T_1$  relaxation time constants were measured for each of the compounds and plotted as a function of inverse temperature to obtain the activation energies associated with the methyl group rotations. It was found that the activation energies associated with cocrystals featuring halogen bonds were lower than that of pure TMP and those featuring hydrogen bonds showing that these non-covalent interactions have a catalytic effect on the methyl group rotations. DFT calculations suggested that the catalytic activity results from the stabilization of the gauche conformation and the destabilization of the staggered conformation of the methyl groups.

Sometimes, dynamic disorder can hide the true nature of the symmetry at a particular nucleus. Wong et al. detailed a solid-state NMR study that monitored the dynamic disorder associated with several hexacyanodiborate(6) salts [21]. The study made use of the  $J(^{11}\text{B}, ^{11}\text{B})$  coupling constants measured using  $^{11}\text{B}$  double-quantum filtered  $J$ -resolved solid-state NMR experiments [215,216]. The doublet splitting observed in these spectra are directly related to the magnetic equivalence of the two boron atoms. A splitting of  $J$  is observed when both boron nuclei are magnetically inequivalent, and  $3J$  indicates magnetic equivalence. In situations where dynamic disorder is relevant, two nuclei that are crystallographically inequivalent may appear to be magnetically equivalent if their molecular motion is fast on the NMR timescale. Over a series of five compounds studied, two were found to have crystallographically inequivalent boron nuclei ( $[\text{B}_2(\text{CN})_6]$   $[\text{nBu}_4\text{N}]_2$  and  $[\text{B}_2(\text{CN})_6][\text{BMPL}]_2$ ), but to also exhibit dynamic motion. This was confirmed *via* the DQF  $J$ -resolved spectra, which showed splittings of  $3J$  for all compounds studied, including the preceding two compounds (Fig. 15).

Recently, d'Agostino et al. applied NMR crystallography to the study of dynamics in the supramolecular salt formed from 12-crown-4, DABCO- $\text{CH}_2$ , and halide ions. In an extension to previous solid-state NMR work completed on DABCO, solid-state NMR indicates a dynamic process in DABCO- $\text{CH}_2$ , besides the known rotation along the pseudo-three-fold axis of DABCO [217]. By lowering the temperature of isomorphous compounds of (12-crown-4)(DABCO- $\text{CH}_2$ )X (where X =  $\text{Cl}_2$ ,  $\text{Br}_2$  or  $\text{ClBr}$ ), two resonances appear at 44.0 and 46.2 ppm in the  $^{13}\text{C}$  NMR spectrum (Fig. 16). The activation energies of these dynamic processes were measured



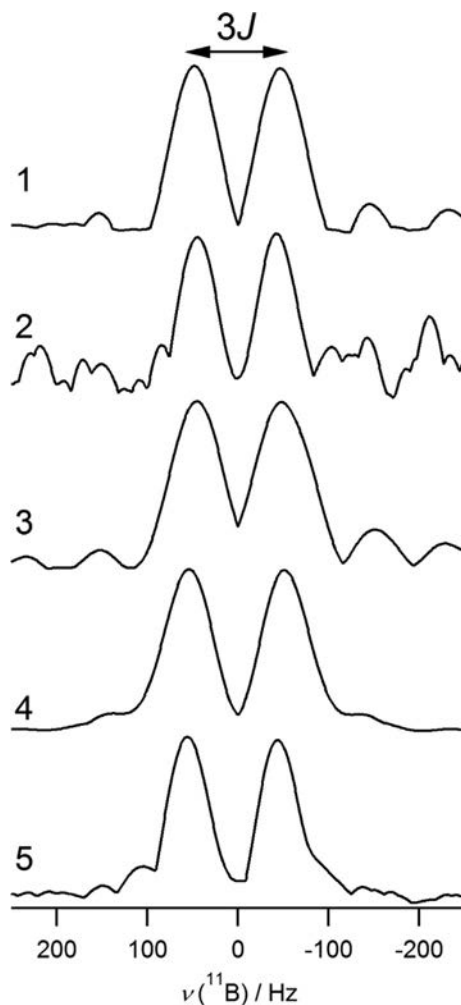


**Fig. 15**  $^{11}\text{B}$  NMR spectra obtained from the indirect dimension of DQF  $J$ -resolved solid-state NMR spectra of a series of diborane compounds featuring crystallographically equivalent boron atoms (1–3) and inequivalent boron atoms that feature dynamic disorder (4–5).  $J(^{11}\text{B}, ^{11}\text{B})$  for the compounds are all approximately 30–35 Hz. From Y.T.A. Wong, J. Landmann, M. Finze, D.L. Bryce, *Dynamic disorder and electronic structures of electron-precise dianionic diboranes: insights from solid-state multinuclear magnetic resonance spectroscopy*, *J. Am. Chem. Soc.* 139 (2017) 8200–8211. <https://doi.org/10.1021/jacs.7b01783>. Used with permission.

to be 52.7 and 50.6 kJ/mol for the  $\text{Br}_2$  and the  $\text{Cl}_2/\text{ClBr}$  salts, respectively. This dynamic process is related to the reversible enantiotropic loss of symmetry of DABCO- $\text{CH}_2$  at low temperatures induced by the surrounding halide ions and 12-crown-4.

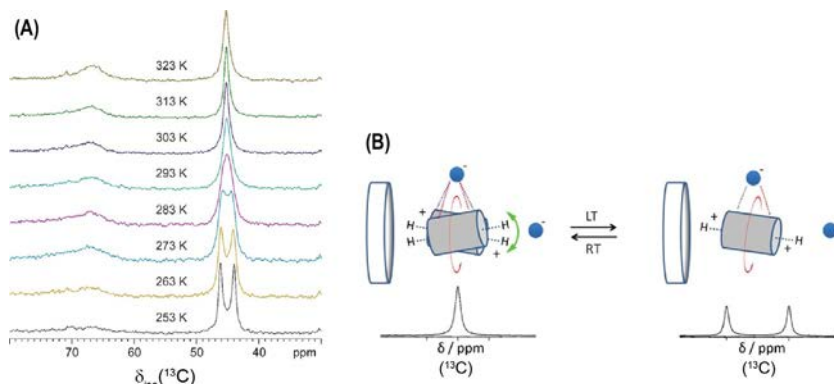


**Fig. 16** (A)  $^{13}\text{C}$  MAS solid-state NMR spectra of  $(\text{DABCOH}_2)\text{Cl}_2$ , acquired increasing temperatures. (B) Representation of the dynamic model solid-state NMR experiments showing the precession motion that accompanies the rotation of the  $(\text{DABCOH}_2)^{2+}$ . From S. d'Agostino, L. Fornasari, F. Grepioni, D. Braga, F. Rossi, M.R. Chierotti, R. Gobetto, *Precessional motion in crystalline solid solutions of ionic rotors*, *Chem. A Eur. J.* 24 (2018) 15059–15066. <https://doi.org/10.1002/chem.201803071>. Adapted with permission.

### 3.4 $^1\text{H}$ spin-lattice relaxation measurements

$^1\text{H}$  spin-lattice relaxation time constants,  $T_1$ , can provide valuable information when studying polymorphs. The  $T_1$  time is influenced by the molecular motions (vibrational, rotational, translational) in a sample and thus provides a way of differentiating between polymorphs. Prior to an NMR experiment, including radiofrequency pulses, the net magnetization,  $M_0$ , is aligned along the magnetic field,  $B_0$ . Following a radiofrequency pulse, the magnetization is forced away from the magnetic field axis,  $Z$ , into the  $XY$ -plane. As time goes on, the component of  $M_0$  that is on the  $z$ -axis,  $M_Z$ , gradually grows to where  $M_0 = M_Z$ .  $T_1$  is the measure of how fast  $M_Z$  returns to  $M_0$  and follows the form  $M_Z = M_0(1 - e^{-\tau/T_1})$ , where  $\tau$  is the time (s). In an inversion recovery experiment,  $T_1$  is measured by applying a 180-degree pulse, followed by a variable time  $\tau$ , then applying a 90-degree pulse. A signal is obtained when the time  $\tau$  is long enough for  $M_Z$  to have returned to  $M_0$ .  $M_Z$  is plotted as a function of  $\tau$  using the function  $M_Z = M_0(1 - 2e^{-\tau/T_1})$  to determine  $T_1$ .

The dominant mechanism contributing to relaxation must be slow enough to be relevant to the NMR timescale. Therefore, the relaxation rate is typically dependent on motions such as methyl group rotations.

A recent study by Apih et al. illustrated the utility of the measurement of  $^1\text{H}$  spin-lattice relaxation times for studying polymorphs. In their work, the polymorphs of carbamazepine were studied by solid-state NMR alongside

$^{14}\text{N}$  NQR (discussed later in this text) [218]. Carbamazepine, a mood-stabilizing drug, is of interest because it is known to form four different anhydrous polymorphs, with form III being the commercially available one. The polymorphs adopt three unique space groups: form I is triclinic, form II is trigonal, form III is monoclinic, and form IV is monoclinic. Each structure features hydrogen-bonded dimers in the unit cell.

The  $T_1$  measurements showed that each form of carbamazepine has unique relaxation characteristics and therefore exhibits different spin-lattice relaxation times between the polymorphs at different temperatures. Form I has a long  $T_1$  at 298 K ( $195 \pm 20$  s), roughly halving at 165 K. Here, the change in the relaxation time was attributed to the slowing of molecular fluctuations. Form III has a long  $T_1$  ( $100 \pm 10$  s) at room temperature, halving at 165 K ( $55 \pm 5$  s) due to conformational changes, likely— $\text{NH}_2$  rotations, slowing down at lower temperatures. In contrast, form II features a very short relaxation time at 298 K ( $0.52 \pm 0.05$  s) because the crystal structure is more ‘open’ and likely allows more significant molecular motions than do the ‘tight’ structures of form I and form III. Interestingly, form IV, unlike the other three polymorphs, undergoes a significant change in  $T_1$  between 295 and 165 K, jumping from  $0.40 \pm 0.05$  s to  $25 \pm 3$  s. This was attributed to a slow exchange at room temperature ( $E_a = 300$  meV), possibly associated with disorder of the amide groups.

Form II also exhibited a peculiar behaviour, which was measured by relaxation techniques. Two samples were produced, where one was subjected to magnetic field cycling experiments, and the other was used to measure the  $^1\text{H}$   $T_1$ . In both cases, a change in the  $^1\text{H}$  signal was observed where the signal became two-component. The transverse relaxation time constant ( $T_2$ ) was measured for both signals, and it was found that one signal had a  $T_2$  of 20  $\mu\text{s}$  (typical of solids) and the other of 600  $\mu\text{s}$ . 600  $\mu\text{s}$  is long for solids and not generally seen because  $^1\text{H}$ – $^1\text{H}$  dipolar interactions typically limit  $T_2$  in solids. As no liquid was visually detected in the sample, they attributed the signal corresponding to this long  $T_2$  to an intermediate ‘plastic phase’ where the molecules undergo spontaneous rearrangement. In fact, after having been left for months, the sample was re-analyzed and was found to contain form III. The authors concluded that a spontaneous transition from phase II to phase III can occur and can be measured dynamically by relaxation experiments.

In the case of 2,6-di-*tert*-butylnaphthalene,  $^1\text{H}$  spin-lattice relaxation times were demonstrated to be useful in the detection of two polymorphs (A and E) [219,220]. The two polymorphs are structurally similar, with

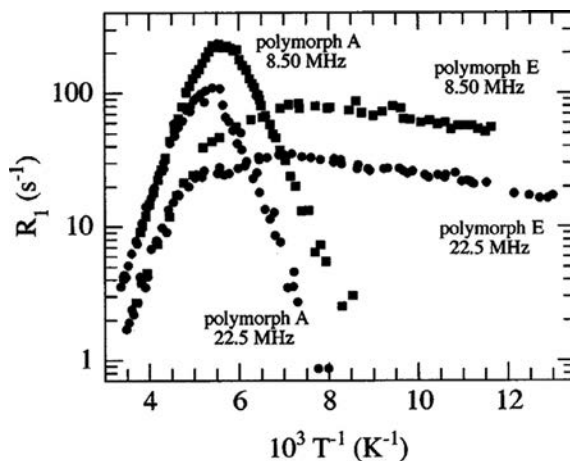


**Fig. 17** Proton spin-lattice relaxation rate shown for polymorphs A and E as a function of inverse temperature,  $T^{-1}$ . From P.A. Beckmann, K.S. Burbank, K.M. Clemons, E.N. Slonaker, K. Averill, C. Dybowski, J.S. Figueroa, A. Glatfelter, S. Koch, L.M. Liable-Sands, A.L. Rheingold,  $^1\text{H}$  nuclear magnetic resonance spin-lattice relaxation,  $^{13}\text{C}$  magic-angle-spinning nuclear magnetic resonance spectroscopy, differential scanning calorimetry, and x-ray diffraction of two polymorphs of 2,6-di-*tert*-butylnaphthalene, *J. Chem. Phys.* 113 (2000) 1958–1965. <https://doi.org/10.1063/1.482000>. Used with permission.

the exception that E has 12 independent *tert*-butyl groups, which  $^{13}\text{C}$  MAS NMR cannot resolve. The temperature dependant  $^1\text{H}$   $T_1$  relaxation analysis measured the relaxation rates,  $R_1 (=1/T_1)$ , at two different NMR frequencies (Fig. 17). The data showed different  $T_1$  relaxation properties for polymorphs A and E, indicating that the  $^1\text{H}$  spin-lattice relaxation rate is an excellent tool to differentiate between two similar polymorphs. The data were further analyzed to show that for polymorph A, the relaxation model is consistent with the presence of a single *tert*-butyl group, and for polymorph E, the data must be modelled while taking into account significantly more complex dynamics. The data were fit taking into account the X-ray crystallographic analysis showing 12 unique *tert*-butyl sites.

In a more recent study by Beckmann et al. [221], multiple analytical methods come together with  $^1\text{H}$  spin-lattice relaxation to study solid samples of 2-ethylanthracene (EA) and 2-ethylanthraquinone (EAQ) and the concomitance of their polymorphs [222] present in the samples when prepared in different ways, where concomitance refers to a sample that may contain more than one polymorphic crystal in the powder. In their study, the dominant effects on  $T_1$  of methyl group rotation modulating  $^1\text{H}$ - $^1\text{H}$  dipolar interactions at high temperatures were taken advantage of to study

the anisotropy of methyl group rotations in the different samples of EA and EAQ prepared by different means. Measurement of the  $^1\text{H}$   $T_1$  times yielded some exciting results. The first is that the  $T_1$  of a sample was inhomogeneous on a microscopic scale, in that methyl group rotations near imperfections in the crystal structure, or at the surface of a crystallite, may be faster than in the bulk. In a typical crystallite, methyl group rotations have an activation energy of  $E_a = 18\text{ kJ/mol}$  in EA and  $16\text{ kJ/mol}$  in EAQ. The author's modelling suggests that a significant proportion of the methyl groups in a sample of EA or EAQ (20%) have an activation energy that is  $<90\%$  of the value for the ideal crystal. For EA, the anomalies in  $T_1$  time measurements can be attributed to this feature alone. In the three samples of EAQ, there was evidence to suggest further structural inhomogeneity because the NMR relaxation mechanism is fitted with a double exponential, implying that the relaxation depends on molecules with more than one chemical environment that do not communicate with each other through dipolar interactions. Through sophisticated modelling of the relaxation mechanisms at low temperatures (Fig. 18), the evidence suggests that in EAQ1,  $90 \pm 5\%$  of the sample is composed of 'region 1' ( $R_1$ ) corresponding to the pure polymorph of EAQ, in EAQ2, the proportion is  $50 \pm 15\%$ , and in

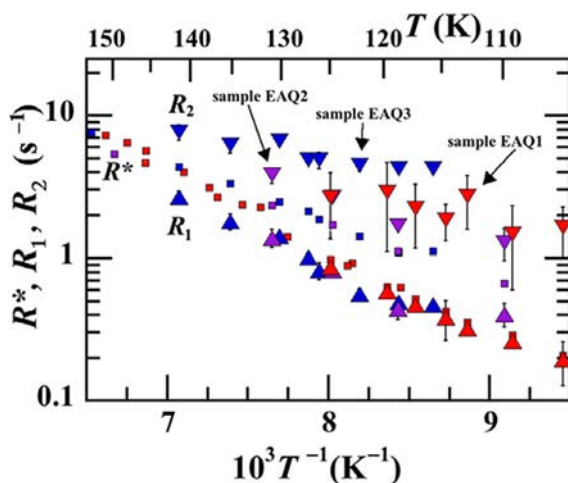


**Fig. 18** Chart showing the specific relaxation rates  $R_1$  ( $\blacktriangle$ ) and  $R_2$  ( $\blacktriangledown$ ) in a double exponential relaxation process as a function of the reciprocal of temperature. From P.A. Beckmann, J. Ford, W.P. Malachowski, A.R. McGhie, C.E. Moore, A.L. Rheingold, G.J. Sloan, S.T. Szewczyk, Proton spin-lattice relaxation in organic molecular solids: polymorphism and the dependence on sample preparation, *ChemPhysChem* 19 (2018) 2423–2436. <https://doi.org/10.1002/cphc.201800237>. Used with permission.

sample EAQ3,  $50 \pm 10\%$ . In the model, ‘region 2’ ( $R_2$ ) reflects one or more crystallite with much faster relaxation, indicating one or more different polymorphs present in the sample, in differing amounts depending on the process of crystallization.

In a 2019 paper by Beckmann et al. [223], the method was explored further. It was demonstrated that  $^1\text{H}$  spin-lattice relaxation experiments can be used jointly alongside X-ray diffraction techniques to study concomitant polymorphism. In this paper, three samples of 2-(*tert*-butyl)-9-(4-(*tert*-butyl)phenyl)anthracene prepared by different mechanisms (sample A: slow evaporation in 1,2-dichloroethane; sample B: recrystallization in diethyl ether; sample C: commercially obtained) were characterized by  $^1\text{H}$  spin-lattice relaxation experiments, taking advantage of the fact that the  $^1\text{H}$ - $^1\text{H}$  spin-spin interactions depend on rotations of the *tert*-butyl groups and their constituent methyl groups. Powder X-ray data suggested that these samples are composed of more than one of the known polymorphs 1, 2, or 3. *Ab initio* modelling of the intramolecular energy cost related to the dihedral angle between the *tert*-butyl phenyl group and the anthracene suggests that a very low energy barrier exists for a range of over 60 degrees. Therefore, this compound may easily form different polymorphs within a single sample upon recrystallization. Modelling of the relaxation rates, dependent on both temperature and NMR frequencies, suggested that the *tert*-butyl groups in all the samples are dynamically equivalent and possess NMR activation energies of  $15.0 \pm 1.5$  kJ/mol. The picture changed somewhat at low temperature when these *tert*-butyl groups become stationary on an NMR timescale. At this point, the out-of-plane methyl groups are subjected to more intermolecular interactions (because of slower motion) and thus experience different rotational activation energies. The reality over the samples reflects a distribution of activation energies of 7–15 kJ/mol resulting from either the additive or subtractive effects of the intermolecular component of the activation energy related to the out-of-plane methyl groups. For each sample, the activation energies were unique, based on the extent to which concomitance is present.

### 3.5 Sensitivity enhancement by paramagnetism

As discussed, the  $T_1$  relaxation time can be long in solids because molecular motions present in the sample are typically much slower than in liquids, where rapid molecular tumbling is usually the dominant contribution to spin-lattice relaxation rates.  $T_1$  relaxation can have a significant effect on

the time and effort required to record solid-state NMR spectra of organic polymorphs. Long spin-lattice relaxation times often result in long experimental times to obtain good quality spectra, especially if only small amounts of the compound of interest are available. Multidimensional NMR is also hampered by long  $T_1$  values; measuring 2D data such as heteronuclear correlation spectra can be impractical. Consequently, efforts to reduce  $T_1$  are of significant interest in the NMR literature.

Adding paramagnetic reagents to a sample of interest is one way that has been shown to reduce the  $T_1$  times. This method takes advantage of the fact that electronic spins relax more rapidly than nuclear spins. A 2018 paper by Quiñones et al. [224] nicely demonstrated this with examples where paramagnetic reagents, such as nickel (II) and chromium (III) acetylacetonates, were added to a series of polymorphic drugs, such as acetaminophen, nabumetone, four phases of carbamazepine, and two forms of cimetidine. Upon introducing the paramagnetic reagents, it was shown by  $^{13}\text{C}$  CP/MAS and powder X-ray diffraction that there was no appreciable change in the crystallinity of the drugs, a factor that is always of concern when using paramagnetic species (Fig. 19).  $^1\text{H}$ - $^{13}\text{C}$  cross-polarization inversion recovery experiments were conducted to measure the  $^1\text{H}$  spin-lattice relaxation times. It was found that by introducing the paramagnetic species, the proton  $T_1$  times are reduced significantly (Fig. 20) except for the hydrate, which already features a relatively short  $T_1$  because of the effect of water dynamics on the crystal lattice. This study therefore provided two excellent examples of paramagnetic species that can be added to organic powders to shorten  $^1\text{H}$   $T_1$  times without the risk of damaging the crystal lattice.

### 3.6 Dynamic nuclear polarization

One of the significant problems that solid-state NMR spectroscopists have to deal with are issues around the sensitivity of NMR-active nuclei, limiting the scope of various projects. While there continue to be recent examples of techniques developed and applied with sensitivity enhancement in mind [225–227], a predominant current method is dynamic nuclear polarization (DNP). DNP is a method applied to solid-state NMR spectroscopy to enhance the sensitivity of nuclei that are frequently challenging by several orders of magnitude. In short, DNP involves the microwave-induced transfer of spin polarization from unpaired electrons to NMR-active nuclei. Sensitivity enhancements are proportional to the ratio of gyromagnetic ratios of the spins involved in the polarization transfer. Recent accounts

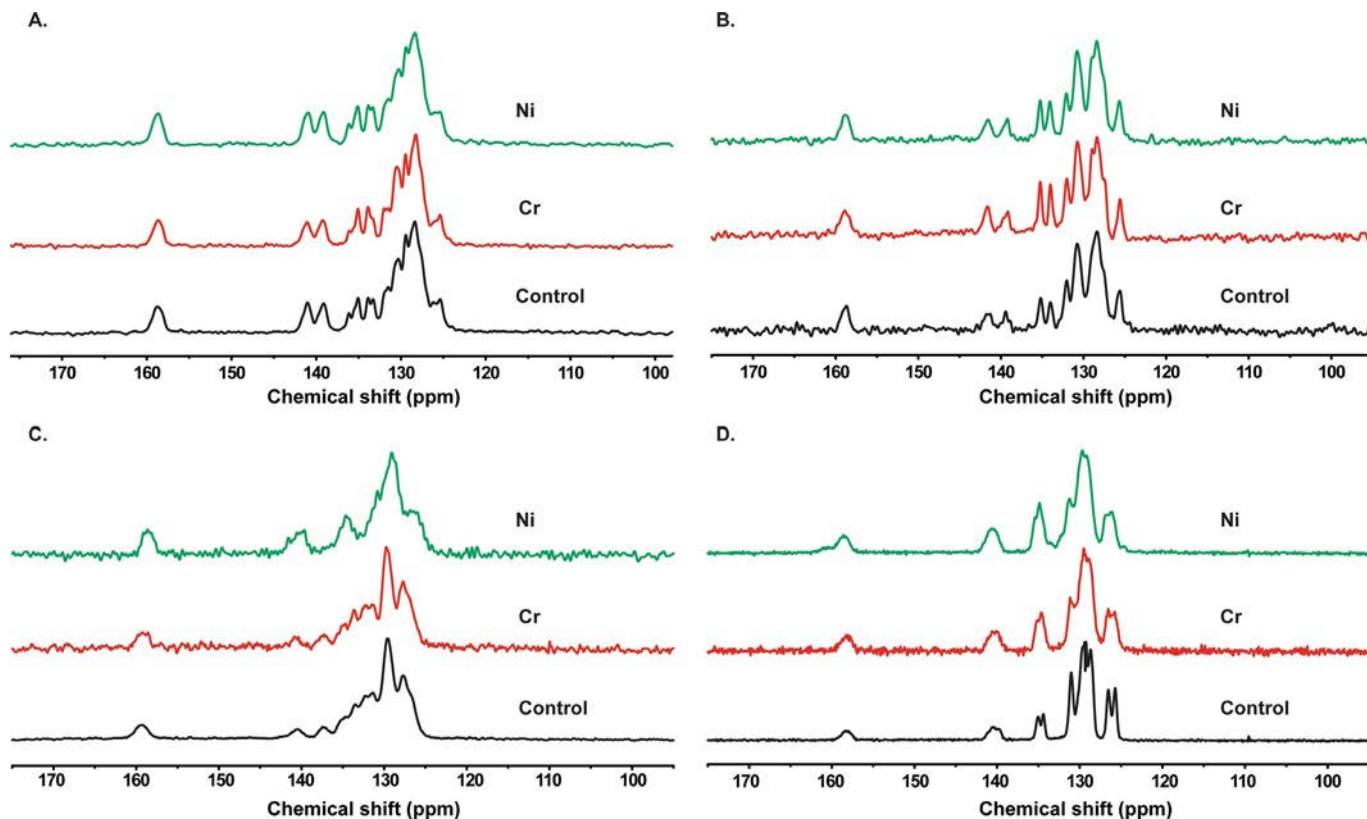


**Fig. 19**  $^{13}\text{C}$  CP/MAS spectra of multiple forms of carbamazepine showing the effects of introducing metal complexing agents (red/green spectra as indicated). (A) Form I, (B) Form II, (C) Form III, and (D) dihydrate. From R. Quiñones, R.J. Iuliucci, G. Behnke, R. Brown, D. Shoup, T.M. Riedel, C. Plavchak, B.E. Lininger, J.M. Spehar, Moving towards fast characterization of polymorphic drugs by solid-state NMR spectroscopy, *J. Pharm. Biomed. Anal.* 148 (2018) 163–169. <https://doi.org/10.1016/j.jpba.2017.09.027>. Used with permission.



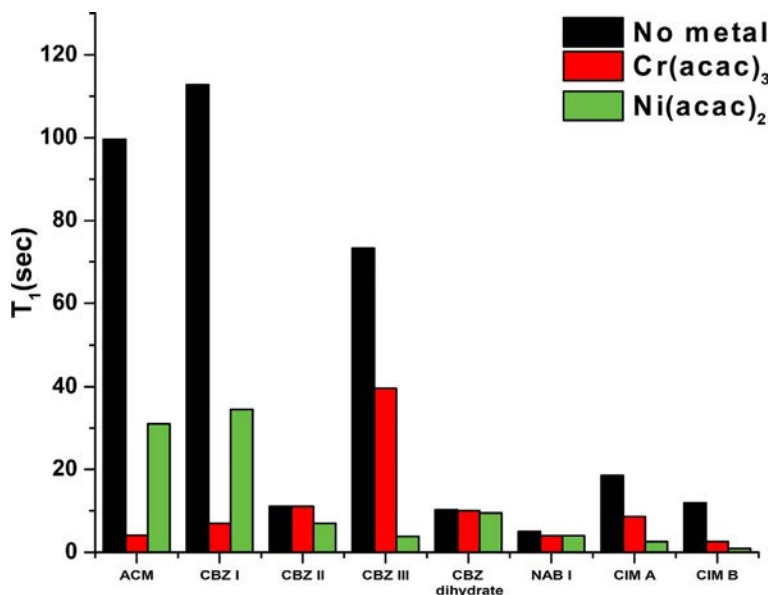


**Fig. 20**  $^1\text{H}$   $T_1$  relaxation times measured for acetaminophen form I (ACM) and carbamazepine (CBZ), nabumetone form I (NAB), and cimetidine forms A and B (CIM). The red bars indicate the relaxation times of the products recrystallized in the presence of 5% w/w of the chromium compound, and the green bars show the same in the presence of the same amount of the nickel compound. The results are compared to the pure recrystallization products (black), typically showing much longer  $T_1$  times. From R. Quiñones, R.J. Iulucci, G. Behnke, R. Brown, D. Shoup, T.M. Riedel, C. Plavchak, B.E. Lininger, J.M. Spehar, Moving towards fast characterization of polymorphic drugs by solid-state NMR spectroscopy, *J. Pharm. Biomed. Anal.* 148 (2018) 163–169. <https://doi.org/10.1016/j.jpba.2017.09.027>. Used with permission.

thoroughly describe the physical concepts and several examples of its success [228–232], so we describe here only a few recent examples of DNP in its application to NMR crystallography.

Often, DNP can vastly reduce experimental times associated with studying pharmaceutical cocrystals and salts. In a 2018 paper, Zhao et al. explored the sensitivity gains of DNP when applied to a series of solid-state NMR experiments to classify a set of solids as either cocrystals or salts, based on the N–H internuclear distances present between the two molecules [233]. The idea behind this was discussed briefly in Section 3.1, where traditional solid-state NMR methods were used to assess compounds that crystallize as either a salt or a cocrystal [139]. DNP, however, can improve the time needed to study these problems and allows for the quick acquisition of one- and two-dimensional NMR spectra that can aid in the detection of

hydrogen bond distances. Their study made use of DNP enhanced  $^{13}\text{C}$  and  $^{15}\text{N}$  CP/MAS,  $^1\text{H}$ - $^{15}\text{N}$  HETCOR,  $^{15}\text{N}\{^1\text{H}\}$   $J$ -resolved,  $^1\text{H}$ - $^{15}\text{N}$  DIPSHIFT, and  $^1\text{H}$ - $^{15}\text{N}$  PRESTO experiments to characterize  $^1\text{H}$ - $^{15}\text{N}$  bonds in an API crystallized with phosphoric acid (A1), fumaric acid (A2) or tosylic acid (A3) by extracting dipolar evolution times and distinguishing salts from cocrystals. The DNP-enhanced variable contact time  $^1\text{H}$ - $^{15}\text{N}$  CP/MAS experiments, typically prohibitively long by means of normal solid-state NMR, showed correlations between nitrogen atoms and directly bonded protons. Two-dimensional HETCOR experiments enabled the proximity between  $^1\text{H}$  and  $^{15}\text{N}$  to be confirmed. DNP-enhanced  $^{15}\text{N}\{^1\text{H}\}$   $J$ -resolved experiments differentiating between salts and cocrystals were shortened from 5 days [52] to 4h. DNP-enhanced  $^{13}\text{C}$ - $^1\text{H}$  and  $^{15}\text{N}$ - $^1\text{H}$  DIPSHIFT and PRESTO-II experiments allowed for the measurement of internuclear C-H and N-H distances. The results were consistent with compounds A1 and A2 being cocrystals because of the N-H distances being longer, suggesting hydrogen bonding (1.43 and 1.55 Å, respectively) while sample A1 had an N-H bond length of only 1.01 Å, consistent with salt formation. This work showed the power of DNP to quickly and reliably enhance traditional NMR approaches to get accurate information about the bonding environment in cocrystals and salts.

A 2019 study by Viger-Gravel et al. [234] demonstrated the utility of DNP-enhanced  $^{19}\text{F}$  NMR by direct hyperpolarization to generate signal enhancements well over 100 using AMUPol and TEKPol as polarizing agents.  $^{19}\text{F}$  is a nucleus that is attractive as an NMR probe because it is spin-1/2, 100% abundant, and commonly found in APIs and other interesting organic molecules. Their strategy was to develop a protocol for signal enhancement and apply it to record enhanced  $^{19}\text{F}$  and  $^{19}\text{F}$ - $^{13}\text{C}$  CP/MAS spectra of 5-fluorouracil. The downside to this nucleus is that it frequently requires long recycle delays to afford a proper return to equilibrium. In their study, recycle delays of 200 and 60 s were required for  $^{19}\text{F}$  and  $^{19}\text{F}$ -CP/MAS experiments, respectively, which helps make a case for DNP to be a useful method in this area. In both modes, a significant enhancement was observed in spectra where hyperpolarization was used as opposed to when it was not. When only a small amount of the API (0.293 mg) was mixed with 30.8 mg of cellulose (to mimic excipients), direct observation of hyperpolarized  $^{19}\text{F}$  yielded the expected line shape with spinning sidebands, as opposed to when the microwaves were off, and only a baseline blob could be observed (Fig. 21A). Signal enhancements were also observed in a  $^{19}\text{F}$ - $^{13}\text{C}$  CP/MAS experiment, showing the detection of all carbons in the molecule using a contact time of 1 ms at 12 kHz MAS (Fig. 21B).

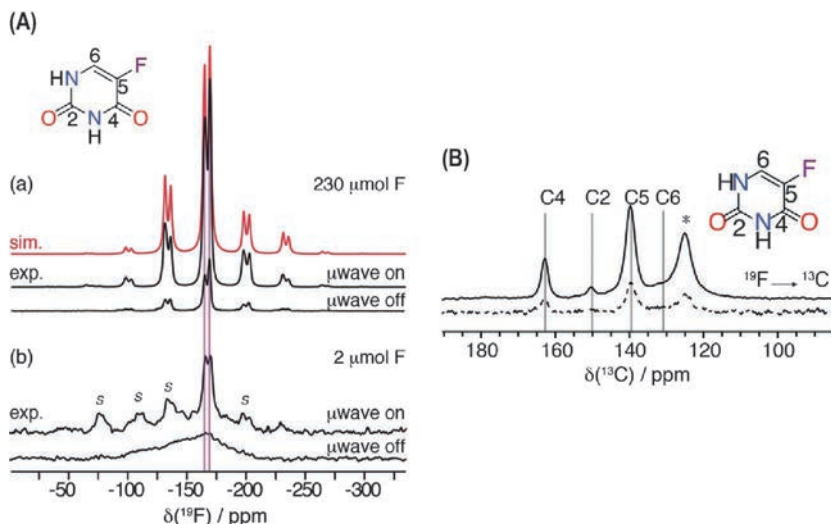


**Fig. 21** (Left, (A))  $^{19}\text{F}$  Hahn echo MAS spectra of 5-fluorouracil acquired with or without microwave irradiation and impregnated with AMUPol in either the pure API form (a) or diluted with cellulose (b). (Right, (B))  $^{19}\text{F}$ - $^{13}\text{C}$  CPMAS DNP spectra of 5-fluorouracil impregnated with AMUPol with (black trace) and without (dotted line) microwave irradiation. From J. Viger-Gravel, C.E. Avalos, D.J. Kubicki, D. Gajan, M. Lelli, O. Ouari, A. Lesage, L. Emsley,  $^{19}\text{F}$  magic angle spinning dynamic nuclear polarization enhanced NMR spectroscopy, *Angew. Chem. Int. Ed.* 58 (2019) 7249–7253. <https://doi.org/10.1002/anie.201814416>. Used with permission.

### 3.7 Nuclear quadrupole resonance spectroscopy (NQR)

Nuclear Quadrupole Resonance (NQR) spectroscopy is a viable alternative for studying nuclei with large quadrupolar interactions because of substantial NMR spectral broadening. Using the same equipment as solid-state NMR, but in the absence of a magnetic field, sharp resonances can be obtained at frequencies in the NQR spectrum that are related to the quadrupolar interaction. A detailed description of the technique can be found in reference [235].

$^{14}\text{N}$  is a quadrupolar nucleus ( $I = 1$ ), which has a history of being a ‘troublesome’ nucleus for solid-state NMR. Although  $^{14}\text{N}$  is 99.63% abundant, it has a moderate electric quadrupole moment ( $Q = 20.44$  mbarn) but a low gyromagnetic ratio ( $\gamma = 1.934 \times 10^7$  rad  $\text{T}^{-1}$   $\text{s}^{-1}$ ). The lack of a central transition results in broad  $^{14}\text{N}$  powder patterns, often requiring specialized techniques to record the full spectra. On the other hand,  $^{15}\text{N}$  ( $I = 1/2$ ) has been studied to a greater extent, but often requires isotopic enrichment because of its low natural abundance (<1%). Nitrogen is an important element for the study of organic polymorphs, especially pharmaceutical ingredients

because it is one of the most commonly found elements in organic chemical structures. Famotidine is an excellent candidate for the study of polymorphism by NQR [236]. This molecule, a histamine H2 receptor antagonist, contains seven nitrogen sites and crystallizes in two polymorphic forms, with the same number of molecules in their unit cells (8) and belonging to monoclinic crystal systems but with varying unit cell dimensions. The study of this molecule by  $^{14}\text{N}$  or even  $^{15}\text{N}$  solid-state NMR would prove challenging because of the complexity of overlapping powder patterns but also because the quadrupolar interaction could significantly broaden some sites. In their paper, Lužnik et al. used  $^{14}\text{N}$  NQR spectroscopy to characterize both polymorphs fully. In the absence of a magnetic field,  $^{14}\text{N}$  has three non-degenerate energy levels with corresponding resonance frequencies dependent on the quadrupolar coupling constant and the asymmetry parameter. The resonances were measured using both pure NQR and NQR in the presence of weak magnetic fields to find all the NQR signals. The signals were then assigned according to both the similarity of the NQR frequencies with other structures and the correlation of  $^{14}\text{N}$  resonance pairs with structurally similar but known molecules. Complete NQR spectra were obtained for both forms A and B, allowing for the complete assignment of  $^{14}\text{N}$  resonances in both polymorphs. While the two polymorphs were structurally similar, crystallographic differences, including different unit cell dimensions, are manifested in differences in the NQR frequencies for most of the nitrogen sites. Each polymorph has its own set of distinct  $^{14}\text{N}$  NQR frequencies which allowed for the identification of form B in a commercially available formulation. Interestingly, their work also demonstrated a dependence of the  $^{14}\text{N}$  NQR linewidths on the compacting pressure during applied during tablet preparation. API linewidths for the tablet formulation are relatively wider than those for the pure compound.

$^{14}\text{N}$  NQR spectroscopy was also used to observe polymorphs of carbamazepine. All four known polymorphs of carbamazepine were previously studied by  $^{13}\text{C}$  MAS solid-state NMR [237,238]. In each case, the  $^{13}\text{C}$  CP/MAS NMR spectra were of low resolution but distinct from one another, showing that they may be used as a 'fingerprint'. The spectra also provide information on the unit cell and whether one full molecule, a half molecule or many molecules are present in the asymmetric unit. All forms have one formula unit in the asymmetric unit except the triclinic form, which has four. The dihydrate form was determined to be monoclinic rather than disordered orthorhombic, as had been previously proposed. To understand the importance of geometrical configurations in polymorphs, a closer look

at the calculated magnetic shielding information yields information about the effect of geometry and intermolecular interaction angles. Ultimately, each polymorph of carbamazepine could be identified and distinguished based on its  $^{13}\text{C}$  NMR spectra. NQR provides a complementary approach to studying carbamazepine by studying differences at  $^{14}\text{N}$  sites rather than  $^{13}\text{C}$ . Here,  $^{14}\text{N}$  NQR confirms the crystal structures of the polymorphs, the number of unique molecules within the unit cells, and provides a robust and straightforward way of discerning between each of the polymorphs.  $^{14}\text{N}$  NQR results, used alongside quantum chemical calculations, also provides information about bonding to the amides themselves. For instance, the observed quadrupolar coupling constants can be correlated to the number of  $\text{N-H}\cdots\text{O}$  hydrogen bonds present at that site.

### 3.8 Crystal structure prediction

Crystal structure prediction algorithms have gained traction in NMR crystallography over the past few years because of their ability to predict crystal structures and the most likely polymorphs based on the user input of a simple molecule. Typically, *ab initio* calculations are performed to find the most likely crystal structures of a compound of interest. This information can then complement the current practices of NMR crystallography to validate or even determine crystal structures by comparing the magnetic shielding values obtained from the theoretical calculations to the experimental chemical shifts obtained in the lab. This strategy is potentially very useful, particularly in cases where single crystals cannot be grown because of problems attributed to stability or kinetics.

Crystal structure prediction has sparked interest in those studying polymorphism for some time. Modifications to a crystal structure because of polymorphism can affect properties such as its dissolution rate, which interests drug manufacturers. Finding the best polymorph of an API is vital in maximizing the efficiency of getting the drug into the body. Crystal structure prediction algorithms also has a part to play in the solution of the crystal structures of new polymorphs of materials [239].

To this end, crystal structure prediction is a powerful tool in the prediction of various simple crystal structures. While there is a long history in crystal structure prediction going back decades, more recent examples of success include small molecules such as phenobarbital [240], alpha-amino acids [241], aspirin [242] and others through a series of blind tests performed by an international consortium hosted by the Cambridge Crystallographic Data Centre (CCDC) [243–248].

In the context of NMR crystallography, crystal structure prediction is a tool that can help to confirm the identity of a particular crystal structure. For example, solid-state NMR spectroscopy can help select for crystal structures based on their molecular conformations instead of their lattice structures [249]. In the last few years, several studies have attempted to combine the two methods to determine new polymorphs and new crystal structures.

A simple example of this is the case of catechin, a molecule that possesses potent antioxidant properties, among other biological activities. There are three known phases of the (+)-catechin hydrate: the  $\alpha$ - and  $\beta$ -monohydrates and the 4.5-hydrate (form I). In a paper by Dudek et al. [250], the three phases of catechin were studied by  $^1\text{H}$ ,  $^2\text{H}$ , and  $^{13}\text{C}$  NMR in combination with theoretical calculations. In particular, the  $^{13}\text{C}$  CP/MAS spectrum obtained corresponding to form I showed a highly crystalline phase. Storage of form I over time will result in additional narrow resonances corresponding to either the  $\alpha$ - and  $\beta$ -monohydrates. As the structure of (+)-catechin loses water, the resonances become very broad, indicating an amorphous phase of the compound (form III). Following this, the authors studied the dehydration process by partially dehydrating each of the crystal structures. To determine the crystal structures of these distinct forms, polymorph structure prediction was used to generate a few low-energy candidates, which were then used to calculate dehydration dynamics and the  $^1\text{H}$  and  $^{13}\text{C}$  isotropic chemical shifts to be compared to the experimental results. The  $^1\text{H}$ - $^{13}\text{C}$  FSLG-HETCOR experiment clearly shows the effects of dehydration at the OH-13 proton site, resulting from a stronger hydrogen bond in form II than in form III. The theoretical calculations help rationalize the NMR results by indicating that upon dehydration, the crystal structure of (+)-catechin collapses, reorganizes, or stays the same, depending on the degree of dehydration. The experimental results show that partially dehydrated (+)-catechin contains 2–2.5 molecules of water, but the crystal structure converts to form II when there are fewer than 1.5 molecules of water present (indicating a discontinuous phase-change process). The hydrogen bonding network is affected most by the dehydration.

One challenge of crystal structure prediction is the calculation of low energy structures, taking into account a high degree of conformational flexibility. Dudek et al. successfully used a combination of crystal structure prediction and solid-state NMR to validate the structure of procyanidin A-2 dihydrate (PA-2) [251]. This highly conformationally flexible and large

natural product readily forms solvates and belongs to a class of molecules that do not readily form crystals for diffraction studies, PA-2 being the exception. The molecule is challenging from a crystal structure prediction standpoint because it contains 72 atoms and exhibits two bonds where torsion is possible. Stable conformers were calculated and subjected to an algorithm that predicted 67 crystal packing arrangements. GIPAW DFT NMR parameters were calculated for each of the 67 structures using the PBE-TS functional.  $^{13}\text{C}$  CP/MAS of PA-2 revealed a sophisticated structure with 20 well-defined resonances, implying a high level of crystallinity. Two  $^1\text{H}$ - $^{13}\text{C}$  INEPT spectra were run with contact times of 75 and 500  $\mu\text{s}$  with a spinning frequency of 60 kHz to obtain proton chemical shifts. Determining both  $^{13}\text{C}$  and  $^1\text{H}$  chemical shifts is important for crystal structure prediction in NMR crystallography, as they are compared to the theoretically obtained chemical shift tensors. Correlation coefficients were calculated by comparing the experimental chemical shifts to the theoretical shielding constants for each of the 67 structures. The conclusions are interesting. The authors stress that because  $^1\text{H}$  chemical shifts are most sensitive to changes in the crystal structure, they must be taken into account and that  $^{13}\text{C}$  resonances alone are not enough to confirm a crystal structure adequately. The authors suggest, in agreement with other literature [37], that because the comparison between theoretical and experimental  $^{13}\text{C}$  chemical shifts always shows an almost perfect correlation over the 67 structures, they are not sensitive enough to use alone in detecting variability between crystal structures. At the very least, the principal components of the  $^{13}\text{C}$  shielding tensors must be used if  $^1\text{H}$  data are not available. Taking into account all the  $^1\text{H}$  shielding data, the authors conclude that conformer 6 with a  $\text{P}2_12_12_1$  space group most closely matches the experimental NMR data. However, because the same conformer in a  $\text{P}2_1$  space group was also in good agreement, powder X-ray diffraction was used to refine the space group because the NMR data alone could not select for the right one with enough confidence. The simulated pattern corresponding to conformer 6 in the  $\text{P}2_12_12_1$  space group was determined to be a match. The crystal structure was overlaid with the known crystal structure, showing almost perfect agreement except for some hydroxyl group orientations (Fig. 22). This paper indicates correctly that crystal structure prediction can be used alongside solid-state NMR, GIPAW DFT calculations and powder X-ray crystallography to determine the crystal structure of unknown solid-state samples as long as the identity of the molecule is known, even those who display a higher degree of complexity.



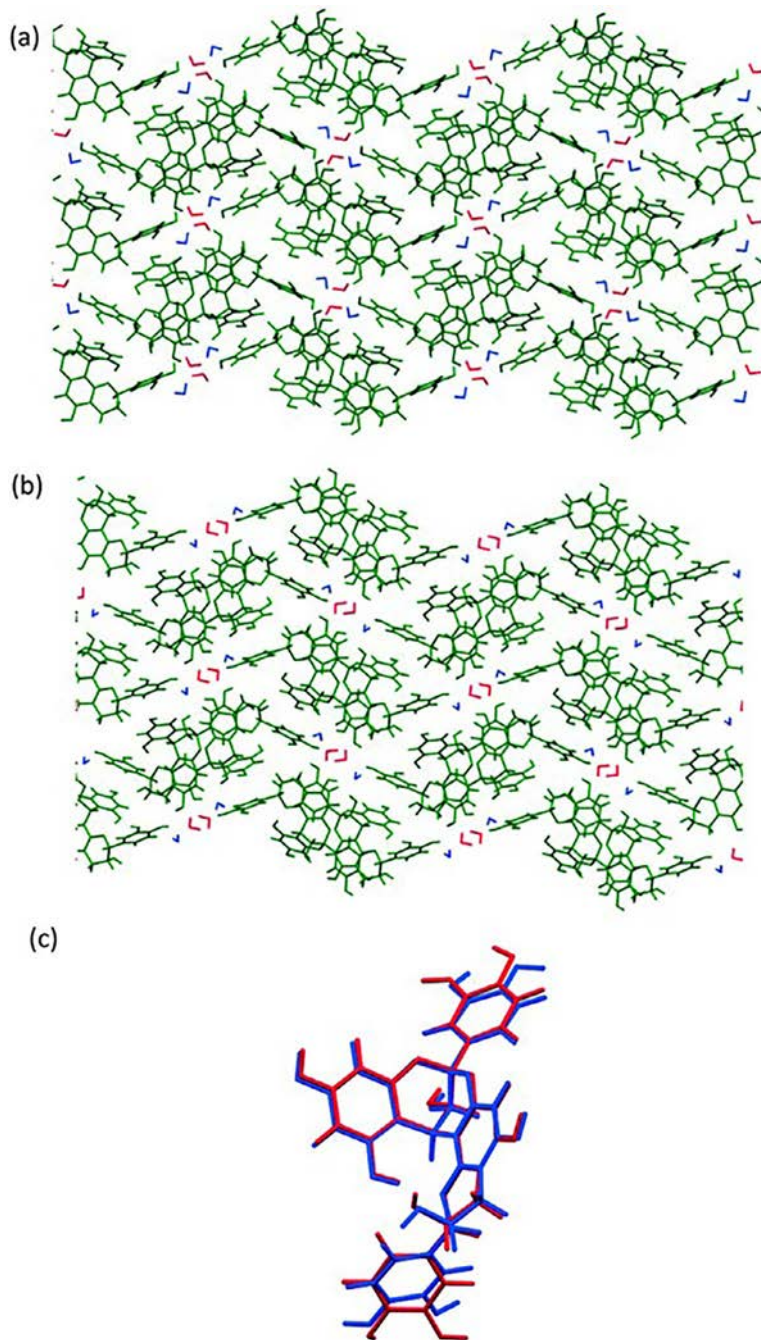


**Fig. 22** Crystal structure of PA-2. (A) The form of the most likely predicted crystal structure, (B) the experimentally determined crystal structure, and (C) and overlay of the predicted (red) and experimental (blue) molecular structures obtained from the crystal structures. From M.K. Dudek, G. Bujacz, M.J. Potrzebowski, *Experimental tests for quality validation of computationally predicted crystal structures—a case of a conformationally flexible procyanidin A-2 dihydrate*, *CrystEngComm* 19 (2017) 2903–2913. <https://doi.org/10.1039/C7CE00618G>. Used with permission.



One goal of NMR crystallography is the *de novo* determination of crystal structures. In a 2013 paper, Baías et al. combined crystal structure prediction with  $^1\text{H}$  solid-state NMR spectroscopy to determine the crystal structure of form 4 of 4-[4-(2-adamantylcarbamoyl)-5-*tert*-butylpyrazol-1-yl]benzoic acid (AZD8329), a hydroxysteroid dehydrogenase inhibitor with potential for the treatment of Type 2 diabetes [252]. This paper described the first attempt at crystal structure determination using this approach. Carbon chemical shifts were assigned using the  $^{13}\text{C}$ - $^{13}\text{C}$  INADEQUATE experiment, which has the bonus of providing connectivities between carbons, except for the adamantane group.  $^1\text{H}$ - $^{13}\text{C}$  HETCOR experiments were employed to determine  $^1\text{H}$  chemical shifts (Fig. 23).

Crystal structure prediction yielded 34 structures (20 *trans* and 14 *cis* configurations) with low enough energy to be considered further. The experimental chemical shifts were compared to the calculated shieldings for each of the proposed crystal structures. The analysis showed that only one structure with *cis* configuration matched the experimental NMR data within the experimental chemical shift error, and that this structure also has the lowest predicted energy (Fig. 24). The combination of crystal structure prediction and NMR data provided a *de novo* determined crystal structure, with the correct space group (P1) and positions of hydrogens in the hydrogen bonds present at the carboxylic acids. This paper nicely illustrates the power of NMR spectroscopy in not only determining unknown crystal structures, but also in refining the atomic positions of  $^1\text{H}$  atoms, which typical single-crystal X-ray methods cannot achieve.

In contrast to most approaches, where a set of crystal structures are predicted before comparing to experimental NMR data, Hofstetter et al. illustrated an approach to crystal structure prediction whereby the NMR data is used to introduce constraints to conformer selection [253]. Crystal structure prediction is typically limited by the substantial computational resources required, which scales rapidly with the degrees of freedom present in a molecule. So far, geometric constraints obtained from solid-state NMR are applied to crystal structure prediction only after viable low-energy candidates are selected. However, the authors present the case that prior knowledge of geometric constraints from NMR data can significantly improve crystal structure prediction.

In their approach, experimentally measured constraints satisfy both the crystal structure and the gas phase conformations, such that they can

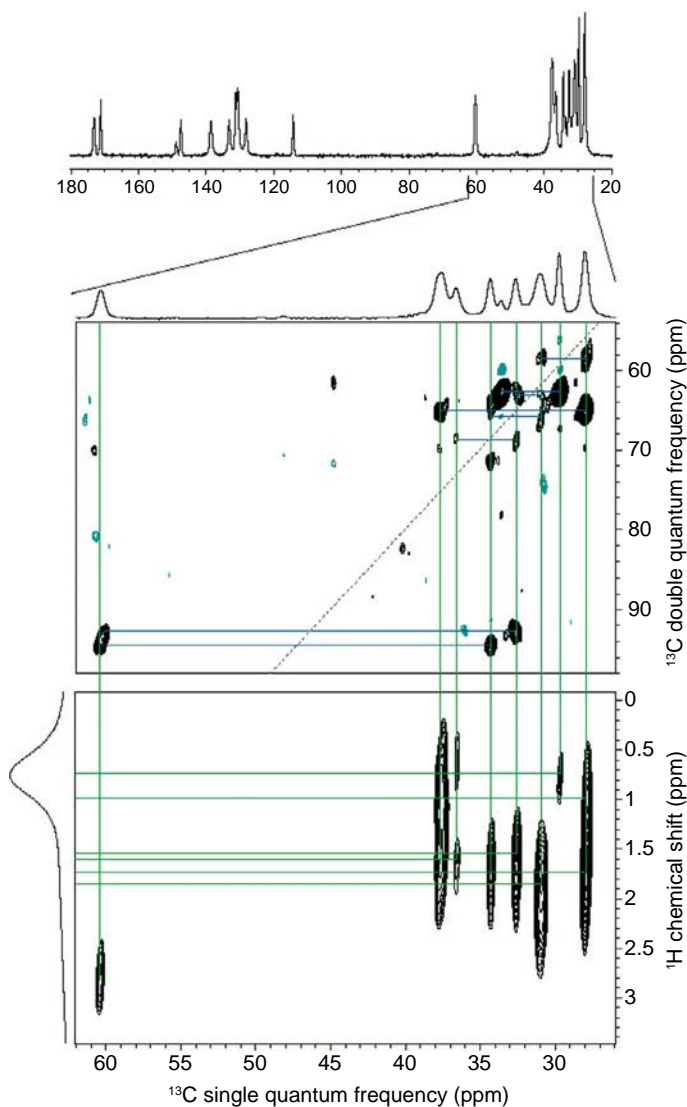


**Fig. 23** Stacked NMR spectra of AZD8329 Form 4.  $^{13}\text{C}$  CP/MAS spectrum of AZD8329 Form 4 (Top).  $^{13}\text{C}$ - $^{13}\text{C}$  INADEQUATE spectrum showing the aliphatic region of AZD8329 (middle) with the corresponding  $^1\text{H}$ - $^{13}\text{C}$  HETCOR spectrum shown below (bottom). Cross peaks in the INADEQUATE spectrum are indicated by blue lines, while the green lines show  $^1\text{H}$ - $^{13}\text{C}$  correlations. Reprinted with permission from M. Baías, J.-N. Dumez, P.H. Svensson, S. Schantz, G.M. Day, L. Emsley, De Novo determination of the crystal structure of a large drug molecule by crystal structure prediction-based powder NMR crystallography, *J. Am. Chem. Soc.* 135 (2013) 17501–17507. <https://doi.org/10.1021/ja4088874>. Copyright 2013 American Chemical Society.

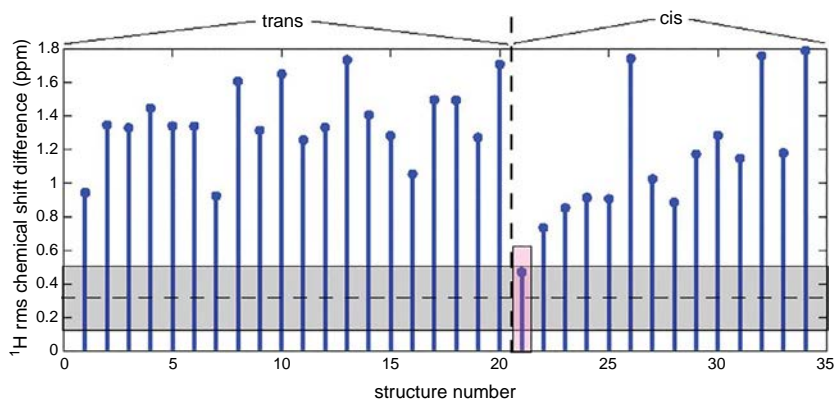


**Fig. 24** Comparison between experimental  $^1\text{H}$  chemical shifts for AZD8329 form 4 to calculated shifts for the predicted structures, represented as the RMS shift difference. The red box represents the predicted structure, which yields the NMR results closest to the experimental spectrum. The grey box represents an acceptable range of RMS chemical shift differences. Reprinted with permission from M. Baías, J.-N. Dumez, P.H. Svensson, S. Schantz, G.M. Day, L. Emsley, *De Novo determination of the crystal structure of a large drug molecule by crystal structure prediction-based powder NMR crystallography*, *J. Am. Chem. Soc.* 135 (2013) 17501–17507. <https://doi.org/10.1021/ja4088874>. Copyright 2013 American Chemical Society.

adequately guide the prediction process. For example, in a  $^1\text{H}$ - $^{13}\text{C}$  HETCOR spectrum, the presence or absence of cross-peaks indicates which atoms are close together in space. The lack of a cross peak will show that two atoms are further than a certain distance apart, where that distance can be assessed by varying the cross-polarization contact time. The approach is successfully applied to the crystal structure determination of ampicillin.  $^1\text{H}$ - $^{13}\text{C}$  HETCOR was used to determine geometric constraints that matched the determined gas-phase conformations. This information ruled out 9 of the original 16 structures that could be considered, meaning it subjected only 7 conformers to crystal structure prediction, lowering the computational cost by  $\sim 55\%$ . From this point, GIPAW DFT calculated  $^1\text{H}$  chemical shift values were compared to the experimental spectrum to determine the crystal structure candidates. The experimentally predicted crystal structure shows excellent agreement with the known crystal structure of ampicillin.

Crystal structure prediction in NMR crystallography has also been successfully applied to the design of metal-sulphur batteries. Mali et al. showed that crystal structure prediction in combination with solid-state

NMR, *ab initio* calculations could be used to determine the stable crystal structures of sodium polysulfides [254]. In their study, the formation energies of the known crystal structures of the series of Na-polysulphides were calculated using GIPAW DFT approaches to determine the stability of the crystal structures. Convex-hull plots show that the  $\text{Na}_2\text{S}$ ,  $\beta\text{-Na}_2\text{S}_2$ , and  $\text{Na}_2\text{S}_4$  structures were thermodynamically stable, while the others lay above the curve, indicating that they are not thermodynamically stable. This is corroborated because at high temperatures, they undergo a phase change to the lower energy crystal structures, or elemental S. The question, in this case, is whether crystal structure prediction could predict the lowest energy structures without any *a priori* knowledge of these polymorphs. To that end, the USPEX evolutionary-based algorithm [255–257] was used to predict crystal structures that could be in agreement with the experimental results. The results show that  $\text{Na}_2\text{Sn}$  polysulphides are expected to be the most stable, and the lowest energy forms are predicted to be  $\text{Na}_2\text{S}$ ,  $\text{Na}_2\text{S}_2$ ,  $\text{Na}_2\text{S}_3$ ,  $\text{Na}_2\text{S}_4$ ,  $\text{Na}_2\text{S}_5$ , and  $\text{Na}_2\text{S}_6$ . Before the crystal structure prediction,  $^{23}\text{Na}$  MAS experiments were performed on a series of Na-polysulphides, which are readily available and stable at room temperature:  $\text{Na}_2\text{S}$ ,  $\beta\text{-Na}_2\text{S}_2$ ,  $\text{Na}_2\text{S}_3$ ,  $\text{Na}_2\text{S}_4$ ,  $\alpha\text{-Na}_2\text{S}_5$  and  $\epsilon\text{-Na}_2\text{S}_5$ . The experimental data shows distinct chemical shift and quadrupolar coupling constant differences between the  $^{23}\text{Na}$  sites in the different Na-polysulphides, and in each case, these results are in agreement with the NMR data obtained using GIPAW DFT. A first ‘database’ of  $^{23}\text{Na}$  MAS NMR spectra for Na-polysulfides is shown in Fig. 25 and was proposed by the authors as a tool to study the reaction mechanisms in metal-sulphur batteries involving  $^{23}\text{Na}$  environments because this is a nucleus that is extremely sensitive to changes in its chemical environment. In summary, this proof-of-principle study showed that crystal structure prediction can predict the lowest energy crystal structures of metal-sulphides and is proposed to be used in combination with solid-state NMR to determine the identity of crystal structures present in dynamic processes.

A similar approach was demonstrated in 2017 when Mali described the crystal structure prediction of magnesium (poly) sulphides [258]. Here, the  $^{25}\text{Mg}$  NMR parameters were calculated and could serve as a reference to experimentally determined  $^{25}\text{Mg}$  parameters in the identification of metal-sulphides.

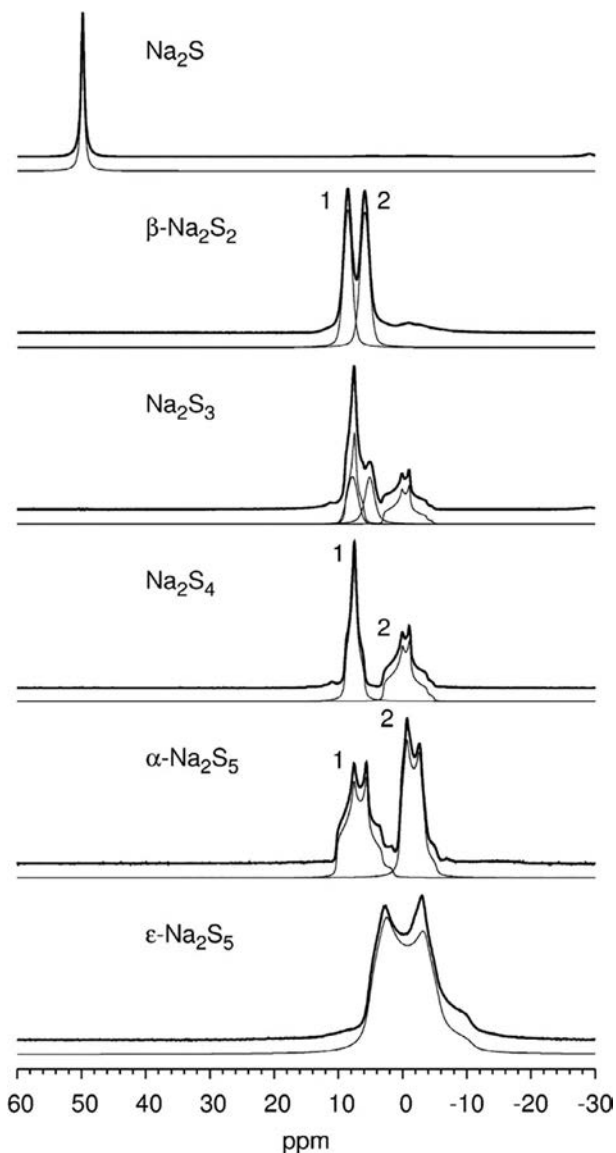


**Fig. 25**  $^{23}\text{Na}$  MAS NMR of a series of Na-polysulfides. From G. Mali, M.U.M. Patel, M. Mazaj, R. Dominko, *Stable crystalline forms of Na polysulfides: experiment versus Ab initio computational prediction*, *Chem. A Eur. J.* 22 (2016) 3355–3360. <https://doi.org/10.1002/chem.201504242>. Used with permission.



## 4. Concluding remarks

There have been many recent advances in the field of NMR crystallography and in applications of solid-state NMR to study polymorphism. We have provided an overview of the methodology that has been developed and applied to problems related to polymorphism in both organic and inorganic systems, and other topics related to NMR crystallography, including non-covalent interactions and dynamic processes in the solid state. As time goes on, more and more techniques are being used alongside solid-state NMR spectroscopy, expanding the scope of NMR crystallography and its capabilities. We highlight that dynamic nuclear polarization is becoming regularly used to solve many problems that were previously unsuitable for solid-state NMR. Also, as computational resources become more powerful than in the past, crystal structure prediction will continue to be exploited in ways that were not previously possible. We expect the field of NMR crystallography to continue to grow into a rich field of study and application.

## Acknowledgements

We thank the Natural Sciences and Engineering Research Council of Canada for funding, and all members of our laboratory for proofreading the manuscript.

## References

- [1] K.M.N. Burgess, C.M. Widdifield, Y. Xu, C. Leroy, D.L. Bryce, Structural insights from  $^{59}\text{Co}$  solid-state NMR experiments on organocobalt(II) catalysts, *ChemPhysChem* 19 (2018) 227–236. <https://doi.org/10.1002/cphc.201700990>.
- [2] P. Crewdson, D.L. Bryce, F. Rominger, P. Hofmann, Application of ultrahigh-field  $^{59}\text{Co}$  solid-state NMR spectroscopy in the investigation of the 1,2-polybutadiene catalyst  $[\text{Co}(\text{C}_8\text{H}_{13})(\text{C}_4\text{H}_6)]$ , *Angew. Chem. Int. Ed.* 47 (2008) 3454–3457. <https://doi.org/10.1002/anie.200705204>.
- [3] P.M.J. Szell, S. Zablotny, D.L. Bryce, Halogen bonding as a supramolecular dynamics catalyst, *Nat. Commun.* 10 (2019) 916. <https://doi.org/10.1038/s41467-019-08878-8>.
- [4] J.A.M. Lummiss, F.A. Perras, R. McDonald, D.L. Bryce, D.E. Fogg, Sterically driven olefin metathesis: the impact of alkylidene substitution on catalyst activity, *Organometallics* 35 (2016) 691–698. <https://doi.org/10.1021/acs.organomet.5b00984>.
- [5] D. Zanolli, D. Hasa, M. Arhangelskis, G. Schneider-Rauber, M.R. Chierotti, J. Keiser, D. Voinovich, W. Jones, B. Perissutti, Mechanochemical formation of racemic praziquantel hemihydrate with improved biopharmaceutical properties, *Pharmaceutics* 12 (2020) 289. <https://doi.org/10.3390/pharmaceutics12030289>.
- [6] P. Hodgkinson, NMR crystallography of molecular organics, *Prog. Nucl. Magn. Reson. Spectrosc.* 118–119 (2020) 10–53. <https://doi.org/10.1016/j.pnmrs.2020.03.001>.
- [7] R.K. Harris, E.D. Becker, S.M.C.D. Menezes, P. Granger, R.E. Hoffman, K.W. Zilm, Further conventions for NMR shielding and chemical shifts: (IUPAC recommendations 2008), *Pure Appl. Chem.* 80 (2008) 59–84. <https://doi.org/10.1515/iupac.80.0001>.

- [8] J. Herzfeld, A.E. Berger, Sideband intensities in NMR spectra of samples spinning at the magic angle, *J. Chem. Phys.* 73 (1980) 6021–6030. <https://doi.org/10.1063/1.440136>.
- [9] U. Haeberlen, *High Resolution NMR in Solids Selective Averaging*, Supplement to *Advances in Magnetic Resonance*, Academic Press, Inc., New York, 1976. <https://doi.org/10.1016/B978-0-12-025561-0.X5001-1>.
- [10] R.P. Young, C.R. Lewis, C. Yang, L. Wang, J.K. Harper, L.J. Mueller, TensorView: a software tool for displaying NMR tensors, *Magn. Reson. Chem.* 57 (2019) 211–223. <https://doi.org/10.1002/mrc.4793>.
- [11] A. Samoson, Satellite transition high-resolution NMR of quadrupolar nuclei in powders, *Chem. Phys. Lett.* 119 (1985) 29–32.
- [12] C.M. Widdifield, D.L. Bryce, Solid-state  $^{127}\text{I}$  NMR and GIPAW DFT study of metal iodides and their hydrates: structure, symmetry, and higher-order quadrupole-induced effects, *J. Phys. Chem. A* 114 (2010) 10810–10823. <https://doi.org/10.1021/jp108237x>.
- [13] C.M. Widdifield, A.D. Bain, D.L. Bryce, Definitive solid-state  $^{185/187}\text{Re}$  NMR spectral evidence for and analysis of the origin of high-order quadrupole-induced effects for  $I = 5/2$ , *Phys. Chem. Chem. Phys.* 13 (2011) 12413–12420. <https://doi.org/10.1039/C1CP20572B>.
- [14] A.D. Bain, Exact calculation, using angular momentum, of combined Zeeman and quadrupolar interactions in NMR, *Mol. Phys.* 101 (2003) 3163–3175. <https://doi.org/10.1080/00268970310001626298>.
- [15] F.A. Perras, C.M. Widdifield, D.L. Bryce, QUEST—QUadrupolar Exact SofTware: a fast graphical program for the exact simulation of NMR and NQR spectra for quadrupolar nuclei, *Solid State Nucl. Magn. Reson.* 45–46 (2012) 36–44. <https://doi.org/10.1016/j.snmr.2012.05.002>.
- [16] D. Massiot, F. Fayon, M. Deschamps, S. Cadars, P. Florian, V. Montouillout, N. Pellerin, J. Hiet, A. Rakhmatullin, C. Bessada, Detection and use of small  $J$  couplings in solid state NMR experiments, *C. R. Chim.* 13 (2010) 117–129. <https://doi.org/10.1016/j.crci.2009.05.001>.
- [17] G.J. Rees, S.P. Day, K.E. Barnsley, D. Iuga, J.R. Yates, J.D. Wallis, J.V. Hanna, Measuring multiple  $^{17}\text{O}$ – $^{13}\text{C}$   $J$ -couplings in naphthalaldehydic acid: a combined solid state NMR and density functional theory approach, *Phys. Chem. Chem. Phys.* 22 (2020) 3400–3413. <https://doi.org/10.1039/C9CP03977E>.
- [18] S.L. Carnahan, B.J. Lampkin, P. Naik, M.P. Hanrahan, I.I. Slowing, B. VanVeller, G. Wu, A.J. Rossini, Probing O–H bonding through proton detected  $^1\text{H}$ – $^{17}\text{O}$  double resonance solid-state NMR spectroscopy, *J. Am. Chem. Soc.* 141 (2019) 441–450. <https://doi.org/10.1021/jacs.8b10878>.
- [19] J. Viger-Gravel, J.E. Meyer, I. Korobkov, D.L. Bryce, Probing halogen bonds with solid-state NMR spectroscopy: observation and interpretation of  $J(^{77}\text{Se}, ^{31}\text{P})$  coupling in halogen-bonded  $\text{P} = \text{Se} \cdots \text{I}$  motifs, *CrystEngComm* 16 (2014) 7285–7297. <https://doi.org/10.1039/C4CE00345D>.
- [20] L. Kobera, S.A. Southern, G.K. Rao, D.S. Richeson, D.L. Bryce, New experimental insight into the nature of metal–metal bonds in digallium compounds:  $J$  coupling between quadrupolar nuclei, *Chem. A Eur. J.* 22 (2016) 9565–9573. <https://doi.org/10.1002/chem.201600999>.
- [21] Y.T.A. Wong, J. Landmann, M. Finze, D.L. Bryce, Dynamic disorder and electronic structures of electron-precise dianionic diboranes: insights from solid-state multi-nuclear magnetic resonance spectroscopy, *J. Am. Chem. Soc.* 139 (2017) 8200–8211. <https://doi.org/10.1021/jacs.7b01783>.
- [22] S. Penzel, A. Oss, M.-L. Org, A. Samoson, A. Böckmann, M. Ernst, B.H. Meier, Spinning faster: protein NMR at MAS frequencies up to 126 kHz, *J. Biomol. NMR* 73 (2019) 19–29. <https://doi.org/10.1007/s10858-018-0219-9>.

- [23] Y.-L. Lin, Y.-S. Cheng, C.-I. Ho, Z.-H. Guo, S.-J. Huang, M.-L. Org, A. Oss, A. Samoson, J.C.C. Chan, Preparation of fibril nuclei of beta-amyloid peptides in reverse micelles, *Chem. Commun.* 54 (2018) 10459–10462. <https://doi.org/10.1039/C8CC05882B>.
- [24] M. Schledorn, A.A. Malär, A. Torosyan, S. Penzel, D. Klose, A. Oss, M.-L. Org, S. Wang, L. Lecoq, R. Cadalbert, A. Samoson, A. Böckmann, B.H. Meier, Protein NMR spectroscopy at 150 kHz magic-angle spinning continues to improve resolution and mass sensitivity, *ChemBioChem* 21 (2020) 2540–2548. n/a <https://doi.org/10.1002/cbic.202000341>.
- [25] W.I. Goldburg, M. Lee, Nuclear magnetic resonance line narrowing by a rotating rf field, *Phys. Rev. Lett.* 11 (1963) 255–258. <https://doi.org/10.1103/PhysRevLett.11.255>.
- [26] M. Lee, W.I. Goldburg, Nuclear-magnetic-resonance line narrowing by a rotating rf field, *Phys. Rev.* 140 (1965) A1261–A1271. <https://doi.org/10.1103/PhysRev.140.A1261>.
- [27] E. Vinogradov, P.K. Madhu, S. Vega, High-resolution proton solid-state NMR spectroscopy by phase-modulated Lee–Goldburg experiment, *Chem. Phys. Lett.* 314 (1999) 443–450. [https://doi.org/10.1016/S0009-2614\(99\)01174-4](https://doi.org/10.1016/S0009-2614(99)01174-4).
- [28] A. Bielecki, A.C. Kolbert, M.H. Levitt, Frequency-switched pulse sequences: homonuclear decoupling and dilute spin NMR in solids, *Chem. Phys. Lett.* 155 (1989) 341–346. [https://doi.org/10.1016/0009-2614\(89\)87166-0](https://doi.org/10.1016/0009-2614(89)87166-0).
- [29] J.S. Waugh, L.M. Huber, U. Haeberlen, Approach to high-resolution nmr in solids, *Phys. Rev. Lett.* 20 (1968) 180–182. <https://doi.org/10.1103/PhysRevLett.20.180>.
- [30] P. Mansfield, Symmetrized pulse sequences in high resolution NMR in solids, *J. Phys. C Solid State Phys.* 4 (1971) 1444–1452. <https://doi.org/10.1088/0022-3719/4/11/020>.
- [31] W.-K. Rhim, D.D. Elleman, R.W. Vaughan, Analysis of multiple pulse NMR in solids, *J. Chem. Phys.* 59 (1973) 3740–3749. <https://doi.org/10.1063/1.1680545>.
- [32] D.P. Burum, W.-K. Rhim, Analysis of multiple pulse NMR in solids. III, *J. Chem. Phys.* 71 (1979) 944–956. <https://doi.org/10.1063/1.438385>.
- [33] D. Sakellariou, A. Lesage, P. Hodgkinson, L. Emsley, Homonuclear dipolar decoupling in solid-state NMR using continuous phase modulation, *Chem. Phys. Lett.* 319 (2000) 253–260. [https://doi.org/10.1016/S0009-2614\(00\)00127-5](https://doi.org/10.1016/S0009-2614(00)00127-5).
- [34] B. Elena, G. de Paëpe, L. Emsley, Direct spectral optimisation of proton–proton homonuclear dipolar decoupling in solid-state NMR, *Chem. Phys. Lett.* 398 (2004) 532–538. <https://doi.org/10.1016/j.cplett.2004.09.122>.
- [35] F.M. Paruzzo, L. Emsley, High-resolution  $^1\text{H}$  NMR of powdered solids by homonuclear dipolar decoupling, *J. Magn. Reson.* 309 (2019) 106598. <https://doi.org/10.1016/j.jmr.2019.106598>.
- [36] E. Salager, G.M. Day, R.S. Stein, C.J. Pickard, B. Elena, L. Emsley, Powder crystallography by combined crystal structure prediction and high-resolution  $^1\text{H}$  solid-state NMR spectroscopy, *J. Am. Chem. Soc.* 132 (2010) 2564–2566. <https://doi.org/10.1021/ja909449k>.
- [37] M. Baías, C.M. Widdifield, J.-N. Dumez, H.P.G. Thompson, T.G. Cooper, E. Salager, S. Bassil, R.S. Stein, A. Lesage, G.M. Day, L. Emsley, Powder crystallography of pharmaceutical materials by combined crystal structure prediction and solid-state  $^1\text{H}$  NMR spectroscopy, *Phys. Chem. Chem. Phys.* 15 (2013) 8069–8080. <https://doi.org/10.1039/C3CP41095A>.
- [38] L.B. Andreas, K. Jaudzems, J. Stanek, D. Lalli, A. Bertarello, T.L. Marchand, D.C.-D. Paepe, S. Kotelovica, I. Akopjana, B. Knott, S. Wegner, F. Engelke, A. Lesage, L. Emsley, K. Tars, T. Herrmann, G. Pintacuda, Structure of fully protonated proteins by proton-detected magic-angle spinning NMR, *Proc. Natl. Acad. Sci.* 113 (2016) 9187–9192. <https://doi.org/10.1073/pnas.1602248113>.



- [39] R. Zhang, K.H. Mroue, A. Ramamoorthy, Proton-based ultrafast magic angle spinning solid-state NMR spectroscopy, *Acc. Chem. Res.* 50 (2017) 1105–1113. <https://doi.org/10.1021/acs.accounts.7b00082>.
- [40] J. Struppe, C.M. Quinn, M. Lu, M. Wang, G. Hou, X. Lu, J. Kraus, L.B. Andreas, J. Stanek, D. Lalli, A. Lesage, G. Pintacuda, W. Maas, A.M. Gronenborn, T. Polenova, Expanding the horizons for structural analysis of fully protonated protein assemblies by NMR spectroscopy at MAS frequencies above 100 kHz, *Solid State Nucl. Magn. Reson.* 87 (2017) 117–125. <https://doi.org/10.1016/j.ssnmr.2017.07.001>.
- [41] B.-J. van Rossum, C.P. de Groot, V. Ladizhansky, S. Vega, H.J.M. de Groot, A method for measuring heteronuclear ( $^1\text{H}$ – $^{13}\text{C}$ ) distances in high speed MAS NMR, *J. Am. Chem. Soc.* 122 (2000) 3465–3472. <https://doi.org/10.1021/ja992714j>.
- [42] J.M. Griffin, D.R. Martin, S.P. Brown, Distinguishing anhydrous and hydrous forms of an active pharmaceutical ingredient in a tablet formulation using solid-state NMR spectroscopy, *Angew. Chem. Int. Ed.* 46 (2007) 8036–8038. <https://doi.org/10.1002/anie.200702582>.
- [43] A.J. Vega, MAS NMR spin locking of half-integer quadrupolar nuclei, *J. Magn. Reson.* 1969 96 (1992) 50–68. [https://doi.org/10.1016/0022-2364\(92\)90287-H](https://doi.org/10.1016/0022-2364(92)90287-H).
- [44] Z. Gan, Measuring amide nitrogen quadrupolar coupling by high-resolution  $^{14}\text{N}/^{13}\text{C}$  NMR correlation under magic-angle spinning, *J. Am. Chem. Soc.* 128 (2006) 6040–6041. <https://doi.org/10.1021/ja0578597>.
- [45] S. Cavadini, A. Lupulescu, S. Antonijevic, G. Bodenhausen, Nitrogen-14 NMR spectroscopy using residual dipolar splittings in solids, *J. Am. Chem. Soc.* 128 (2006) 7706–7707. <https://doi.org/10.1021/ja0618898>.
- [46] J. Trébosc, O. Lafon, B. Hu, J.-P. Amoureux, Indirect high-resolution detection for quadrupolar spin-3/2 nuclei in dipolar HMQC solid-state NMR experiments, *Chem. Phys. Lett.* 496 (2010) 201–207. <https://doi.org/10.1016/j.cplett.2010.07.037>.
- [47] Y. Nishiyama, Y. Endo, T. Nemoto, H. Utsumi, K. Yamauchi, K. Hioka, T. Asakura, Very fast magic angle spinning  $^1\text{H}$ – $^{14}\text{N}$  2D solid-state NMR: sub-micro-liter sample data collection in a few minutes, *J. Magn. Reson.* 208 (2011) 44–48. <https://doi.org/10.1016/j.jmr.2010.10.001>.
- [48] M.K. Pandey, H. Kato, Y. Ishii, Y. Nishiyama, Two-dimensional proton-detected  $^{35}\text{Cl}/^1\text{H}$  correlation solid-state NMR experiment under fast magic angle sample spinning: application to pharmaceutical compounds, *Phys. Chem. Chem. Phys.* 18 (2016) 6209–6216. <https://doi.org/10.1039/C5CP06042G>.
- [49] S. Cavadini, S. Antonijevic, A. Lupulescu, G. Bodenhausen, indirect detection of nitrogen-14 in solid-state NMR spectroscopy, *ChemPhysChem* 8 (2007) 1363–1374. <https://doi.org/10.1002/cphc.200700049>.
- [50] A. Venkatesh, X. Luan, F. Perras, I. Hung, W. Huang, A. Rossini, t1-noise eliminated dipolar heteronuclear multiple-quantum coherence solid-state nmr spectroscopy, *Phys. Chem. Chem. Phys.* 22 (2020) 20815–20828. <https://doi.org/10.26434/chemrxiv.12591629.v1>.
- [51] J.P. Amoureux, J. Trebosc, J. Wiench, M. Pruski, HMQC and refocused-INEPT experiments involving half-integer quadrupolar nuclei in solids, *J. Magn. Reson.* 184 (2007) 1–14. <https://doi.org/10.1016/j.jmr.2006.09.009>.
- [52] A.S. Tatton, T.N. Pham, F.G. Vogt, D. Iuga, A.J. Edwards, S.P. Brown, Probing hydrogen bonding in cocrystals and amorphous dispersions using  $^{14}\text{N}$ – $^1\text{H}$  HMQC solid-state NMR, *Mol. Pharm.* 10 (2013) 999–1007. <https://doi.org/10.1021/mp300423r>.
- [53] A.J. Rossini, M.P. Hanrahan, M. Thuvo, Rapid acquisition of wideline MAS solid-state NMR spectra with fast MAS, proton detection, and dipolar HMQC pulse sequences, *Phys. Chem. Chem. Phys.* 18 (2016) 25284–25295. <https://doi.org/10.1039/C6CP04279A>.

- [54] A. Venkatesh, M.P. Hanrahan, A.J. Rossini, Proton detection of MAS solid-state NMR spectra of half-integer quadrupolar nuclei, *Solid State Nucl. Magn. Reson.* 84 (2017) 171–181. <https://doi.org/10.1016/j.ssnmr.2017.03.005>.
- [55] Z. Gan,  $^{13}\text{C}/^{14}\text{N}$  heteronuclear multiple-quantum correlation with rotary resonance and REDOR dipolar recoupling, *J. Magn. Reson.* 184 (2007) 39–43. <https://doi.org/10.1016/j.jmr.2006.09.016>.
- [56] A. Goldbourt, S. Vega, T. Gullion, A.J. Vega, Interatomic distance measurement in solid-state NMR between a Spin-1/2 and a Spin-5/2 using a universal REAPDOR curve, *J. Am. Chem. Soc.* 125 (2003) 11194–11195. <https://doi.org/10.1021/ja0360642>.
- [57] T. Gullion, A.J. Vega, Measuring heteronuclear dipolar couplings for  $I = 1/2$ ,  $S > 1/2$  spin pairs by REDOR and REAPDOR NMR, *Prog. Nucl. Magn. Reson. Spectrosc.* 47 (2005) 123–136. <https://doi.org/10.1016/j.pnmrs.2005.08.004>.
- [58] F.A. Perras, A. Venkatesh, M.P. Hanrahan, T.W. Goh, W. Huang, A.J. Rossini, M. Pruski, Indirect detection of infinite-speed MAS solid-state NMR spectra, *J. Magn. Reson.* 276 (2017) 95–102. <https://doi.org/10.1016/j.jmr.2017.01.010>.
- [59] L.A. O'Dell, R.W. Schurko, QCPMG using adiabatic pulses for faster acquisition of ultra-wideline NMR spectra, *Chem. Phys. Lett.* 464 (2008) 97–102. <https://doi.org/10.1016/j.cplett.2008.08.095>.
- [60] L.A. O'Dell, The WURST kind of pulses in solid-state NMR, *Solid State Nucl. Magn. Reson.* 55–56 (2013) 28–41. <https://doi.org/10.1016/j.ssnmr.2013.10.003>.
- [61] J. Koppe, M.R. Hansen, Minimizing lineshape distortions in static ultra-wideline nuclear magnetic resonance of half-integer spin quadrupolar nuclei, *J. Phys. Chem. A* 124 (2020) 4314–4321. <https://doi.org/10.1021/acs.jpca.0c03658>.
- [62] R. Bhattacharyya, L. Frydman, Quadrupolar nuclear magnetic resonance spectroscopy in solids using frequency-swept echoing pulses, *J. Chem. Phys.* 127 (2007) 194503. <https://doi.org/10.1063/1.2793783>.
- [63] E. Kupce, R. Freeman, Adiabatic pulses for wideband inversion and broadband decoupling, *J. Magn. Reson. A* 115 (1995) 273–276. <https://doi.org/10.1006/jmra.1995.1179>.
- [64] K.J. Harris, A. Lupulescu, B.E.G. Lucier, L. Frydman, R.W. Schurko, Broadband adiabatic inversion pulses for cross polarization in wideline solid-state NMR spectroscopy, *J. Magn. Reson.* 224 (2012) 38–47. <https://doi.org/10.1016/j.jmr.2012.08.015>.
- [65] C. Leroy, D.L. Bryce, Recent advances in solid-state nuclear magnetic resonance spectroscopy of exotic nuclei, *Prog. Nucl. Magn. Reson. Spectrosc.* 109 (2018) 160–199. <https://doi.org/10.1016/j.pnmrs.2018.08.002>.
- [66] L. Frydman, J.S. Harwood, Isotropic spectra of half-integer quadrupolar spins from bidimensional magic-angle spinning NMR, *J. Am. Chem. Soc.* 117 (1995) 5367–5368. <https://doi.org/10.1021/ja00124a023>.
- [67] A. Deshkar, J. Marcial, S.A. Southern, L. Kobera, D.L. Bryce, J.S. McCloy, A. Goel, Understanding the structural origin of crystalline phase transformations in nepheline ( $\text{NaAlSi}_3\text{O}_8$ )-based glass-ceramics, *J. Am. Ceram. Soc.* 100 (2017) 2859–2878. <https://doi.org/10.1111/jace.14845>.
- [68] S.E. Ashbrook, D. McKay, Combining solid-state NMR spectroscopy with first-principles calculations—a guide to NMR crystallography, *Chem. Commun.* 52 (2016) 7186–7204. <https://doi.org/10.1039/C6CC02542K>.
- [69] D.L. Bryce, G.D. Sward, Chlorine-35/37 NMR spectroscopy of solid amino acid hydrochlorides: refinement of hydrogen-bonded proton positions using experiment and theory, *J. Phys. Chem. B* 110 (2006) 26461–26470. <https://doi.org/10.1021/jp065878c>.

- [70] J. Cui, D.L. Olmsted, A.K. Mehta, M. Asta, S.E. Hayes, NMR crystallography: evaluation of hydrogen positions in hydromagnesite by  $^{13}\text{C}\{^1\text{H}\}$  REDOR solid-state NMR and density functional theory calculation of chemical shielding tensors, *Angew. Chem. Int. Ed.* 58 (2019) 4210–4216. <https://doi.org/10.1002/anie.201813306>.
- [71] R.K. Harris, P.Y. Ghi, R.B. Hammond, C.-Y. Ma, K.J. Roberts, Refinement of hydrogen atomic position in a hydrogen bond using a combination of solid-state NMR and computation, *Chem. Commun.* (2003) 2834–2835. <https://doi.org/10.1039/B309302F>.
- [72] C.M. Widdifield, D.L. Bryce, Crystallographic structure refinement with quadrupolar nuclei: a combined solid-state NMR and GIPAW DFT example using  $\text{MgBr}_2$ , *Phys. Chem. Chem. Phys.* 11 (2009) 7120–7122. <https://doi.org/10.1039/B911448N>.
- [73] S.A. Joyce, J.R. Yates, C.J. Pickard, F. Mauri, A first principles theory of nuclear magnetic resonance J-coupling in solid-state systems, *J. Chem. Phys.* 127 (2007) 204107. <https://doi.org/10.1063/1.2801984>.
- [74] M. Profeta, F. Mauri, C.J. Pickard, Accurate first principles prediction of  $^{17}\text{O}$  NMR parameters in  $\text{SiO}_2$ : assignment of the zeolite ferrierite spectrum, *J. Am. Chem. Soc.* 125 (2003) 541–548. <https://doi.org/10.1021/ja027124r>.
- [75] C.J. Pickard, F. Mauri, All-electron magnetic response with pseudopotentials: NMR chemical shifts, *Phys. Rev. B* 63 (2001) 245101. <https://doi.org/10.1103/PhysRevB.63.245101>.
- [76] J.R. Yates, C.J. Pickard, F. Mauri, Calculation of NMR chemical shifts for extended systems using ultrasoft pseudopotentials, *Phys. Rev. B* 76 (2007), 024401. <https://doi.org/10.1103/PhysRevB.76.024401>.
- [77] S.J. Clark, M.D. Segall, C.J. Pickard, P.J. Hasnip, M.I.J. Probert, K. Refson, M.C. Payne, First principles methods using CASTEP, *Z. Für Krist.—Cryst. Mater.* 220 (2005) 567–570. <https://doi.org/10.1524/zkri.220.5.567.65075>.
- [78] T.F.G. Green, J.R. Yates, Relativistic nuclear magnetic resonance J-coupling with ultrasoft pseudopotentials and the zeroth-order regular approximation, *J. Chem. Phys.* 140 (2014) 234106. <https://doi.org/10.1063/1.4882678>.
- [79] K. Refson, P.R. Tulip, S.J. Clark, Variational density-functional perturbation theory for dielectrics and lattice dynamics, *Phys. Rev. B* 73 (2006) 155114. <https://doi.org/10.1103/PhysRevB.73.155114>.
- [80] P. Giannozzi, S. Baroni, N. Bonini, M. Calandra, R. Car, C. Cavazzoni, D. Ceresoli, G.L. Chiarotti, M. Cococcioni, I. Dabo, A.D. Corso, S. de Gironcoli, S. Fabris, G. Fratesi, R. Gebauer, U. Gerstmann, C. Gougoussis, A. Kokalj, M. Lazzeri, L. Martin-Samos, N. Marzari, F. Mauri, R. Mazzarello, S. Paolini, A. Pasquarello, L. Paulatto, C. Sbraccia, S. Scandolo, G. Sclauzero, A.P. Seitsonen, A. Smogunov, P. Umari, R.M. Wentzcovitch, QUANTUM ESPRESSO: a modular and open-source software project for quantum simulations of materials, *J. Phys. Condens. Matter* 21 (2009) 395502. <https://doi.org/10.1088/0953-8984/21/39/395502>.
- [81] P. Giannozzi, O. Andreussi, T. Brumme, O. Bunau, M.B. Nardelli, M. Calandra, R. Car, C. Cavazzoni, D. Ceresoli, M. Cococcioni, N. Colonna, I. Carnimeo, A.D. Corso, S. de Gironcoli, P. Delugas, R.A. DiStasio, A. Ferretti, A. Floris, G. Fratesi, G. Fugallo, R. Gebauer, U. Gerstmann, F. Giustino, T. Gorni, J. Jia, M. Kawamura, H.-Y. Ko, A. Kokalj, E. Küçükbenli, M. Lazzeri, M. Marsili, N. Marzari, F. Mauri, N.L. Nguyen, H.-V. Nguyen, A. Otero-de-la-Roza, L. Paulatto, S. Poncé, D. Rocca, R. Sabatini, B. Santra, M. Schlipf, A.P. Seitsonen, A. Smogunov, I. Timrov, T. Thonhauser, P. Umari, N. Vast, X. Wu, S. Baroni, Advanced capabilities for materials modelling with Quantum ESPRESSO, *J. Phys. Condens. Matter* 29 (2017) 465901. <https://doi.org/10.1088/1361-648X/aa8f79>.

- [82] G. te Velde, F.M. Bickelhaupt, E.J. Baerends, C. Fonseca Guerra, S.J.A. van Gisbergen, J.G. Snijders, T. Ziegler, Chemistry with ADF, *J. Comput. Chem.* 22 (2001) 931–967. <https://doi.org/10.1002/jcc.1056>.
- [83] J. Autschbach, Analyzing NMR shielding tensors calculated with two-component relativistic methods using spin-free localized molecular orbitals, *J. Chem. Phys.* 128 (2008) 164112. <https://doi.org/10.1063/1.2905235>.
- [84] J. Autschbach, S. Zheng, Analyzing Pt chemical shifts calculated from relativistic density functional theory using localized orbitals: the role of Pt 5d lone pairs, *Magn. Reson. Chem.* 46 (2008) S45–S55. <https://doi.org/10.1002/mrc.2289>.
- [85] J. Autschbach, T. Ziegler, Nuclear spin–spin coupling constants from regular approximate relativistic density functional calculations. I. Formalism and scalar relativistic results for heavy metal compounds, *J. Chem. Phys.* 113 (2000) 936–947. <https://doi.org/10.1063/1.481874>.
- [86] J. Autschbach, T. Ziegler, Nuclear spin–spin coupling constants from regular approximate relativistic density functional calculations. II. Spin–orbit coupling effects and anisotropies, *J. Chem. Phys.* 113 (2000) 9410–9418. <https://doi.org/10.1063/1.1321310>.
- [87] E. van Lenthe, A. Ehlers, E.-J. Baerends, Geometry optimizations in the zero order regular approximation for relativistic effects, *J. Chem. Phys.* 110 (1999) 8943–8953. <https://doi.org/10.1063/1.478813>.
- [88] E. van Lenthe, E.J. Baerends, J.G. Snijders, Relativistic regular two-component Hamiltonians, *J. Chem. Phys.* 99 (1993) 4597–4610. <https://doi.org/10.1063/1.466059>.
- [89] E. van Lenthe, E.J. Baerends, J.G. Snijders, Relativistic total energy using regular approximations, *J. Chem. Phys.* 101 (1994) 9783–9792. <https://doi.org/10.1063/1.467943>.
- [90] X. Gonze, B. Amadon, G. Antonius, F. Arnardi, L. Baguet, J.-M. Beuken, J. Bieder, F. Bottin, J. Bouchet, E. Bousquet, N. Brouwer, F. Bruneval, G. Brunin, T. Cavignac, J.-B. Charraud, W. Chen, M. Côté, S. Cottenier, J. Denier, G. Geneste, P. Ghosez, M. Giantomassi, Y. Gillet, O. Gingras, D.R. Hamann, G. Hautier, X. He, N. Helbig, N. Holzwarth, Y. Jia, F. Jollet, W. Lafargue-Dit-Hauret, K. Lejaeghere, M.A.L. Marques, A. Martin, C. Martins, H.P.C. Miranda, F. Naccarato, K. Persson, G. Petretto, V. Planes, Y. Pouillon, S. Prokhorenko, F. Ricci, G.-M. Rignanese, A.H. Romero, M.M. Schmitt, M. Torrent, M.J. van Setten, B. Van Troeye, M.J. Verstraete, G. Zerah, J.W. Zwanziger, The abinitproject: impact, environment and recent developments, *Comput. Phys. Commun.* 248 (2020) 107042. <https://doi.org/10.1016/j.cpc.2019.107042>.
- [91] R. Censi, P. Di Martino, Polymorph impact on the bioavailability and stability of poorly soluble drugs, *Molecules* 20 (2015) 18759–18776. <https://doi.org/10.3390/molecules201018759>.
- [92] Ł. Szeleszczuk, D.M. Pisklak, T. Gubica, K. Matjakowska, S. Kaźmierski, M. Zielińska-Pisklak, Application of combined solid-state NMR and DFT calculations for the study of piracetam polymorphism, *Solid State Nucl. Magn. Reson.* 97 (2019) 17–24. <https://doi.org/10.1016/j.ssnmr.2018.11.002>.
- [93] Y. Tian, W.D. Wang, W.-B. Zou, J.-Q. Qian, C.-Q. Hu, Application of solid-state NMR to reveal structural differences in cefazolin sodium pentahydrate from different manufacturing processes, *Front. Chem.* 6 (2018) 113. <https://doi.org/10.3389/fchem.2018.00113>.
- [94] J.E. Pacilio, J.T. Tokarski, R. Quiñones, R.J. Iuliucci, High-resolution solid-state NMR spectroscopy: characterization of polymorphism in cimetidine, a pharmaceutical compound, *J. Chem. Educ.* 91 (2014) 1236–1239. <https://doi.org/10.1021/ed400353w>.

- [95] R.W. Brimblecombe, W.A.M. Duncan, G.J. Durant, J.C. Emmett, C.R. Ganellin, M.E. Parsons, Cimetidine—a non-thiourea H<sub>2</sub>-receptor antagonist, *J. Int. Med. Res.* 3 (1975) 86–92. <https://doi.org/10.1177/030006057500300205>.
- [96] B. Hegedüs, S. Görög, The polymorphism of cimetidine, *J. Pharm. Biomed. Anal.* 3 (1985) 303–313. [https://doi.org/10.1016/0731-7085\(85\)80037-6](https://doi.org/10.1016/0731-7085(85)80037-6).
- [97] Patent, Polymorph of Cimetidine, GB1543238A, UK, 1979.
- [98] D.A. Middleton, C.S. Le Duff, F. Berst, D.G. Reid, A cross-polarization magic-angle spinning <sup>13</sup>C NMR characterization of the stable solid-state forms of cimetidine, *J. Pharm. Sci.* 86 (1997) 1400–1402. <https://doi.org/10.1021/js970139g>.
- [99] D.A. Middleton, C.S. Le Duff, X. Peng, D.G. Reid, D. Saunders, Molecular conformations of the polymorphic forms of cimetidine from <sup>13</sup>C solid-state NMR distance and angle measurements, *J. Am. Chem. Soc.* 122 (2000) 1161–1170. <https://doi.org/10.1021/ja993067z>.
- [100] D.A. Middleton, X. Peng, D. Saunders, K. Shankland, W.I.F. David, A.J. Markvardsen, Conformational analysis by solid-state NMR and its application to restrained structure determination from powder diffraction data, *Chem. Commun.* (2002) 1976–1977. <https://doi.org/10.1039/B204289D>.
- [101] J. Madine, D.A. Middleton, An NMR strategy for obtaining multiple conformational constraints for <sup>15</sup>N–<sup>13</sup>C spin-pair labelled organic solids, *Phys. Chem. Chem. Phys.* 8 (2006) 5223–5228. <https://doi.org/10.1039/B610014G>.
- [102] A.S. Tatton, T.N. Pham, F.G. Vogt, D. Iuga, A.J. Edwards, S.P. Brown, Probing intermolecular interactions and nitrogen protonation in pharmaceuticals by novel <sup>15</sup>N-edited and 2D <sup>14</sup>N–<sup>1</sup>H solid-state NMR, *CrstEngComm* 14 (2012) 2654–2659. <https://doi.org/10.1039/C2CE06547A>.
- [103] K. Maruyoshi, D. Iuga, A.E. Watts, C.E. Hughes, K.D.M. Harris, S.P. Brown, Assessing the detection limit of a minority solid-state form of a pharmaceutical by <sup>1</sup>H double-quantum magic-angle spinning nuclear magnetic resonance spectroscopy, *J. Pharm. Sci.* 106 (2017) 3372–3377. <https://doi.org/10.1016/j.xphs.2017.07.014>.
- [104] Y.-L. Hong, G.N. Manjunatha Reddy, Y. Nishiyama, Selective detection of active pharmaceutical ingredients in tablet formulations using solid-state NMR spectroscopy, *Solid State Nucl. Magn. Reson.* 106 (2020) 101651. <https://doi.org/10.1016/j.ssnmr.2020.101651>.
- [105] S.T. Holmes, O.G. Engl, M.N. Srnc, J.D. Madura, R. Quiñones, J.K. Harper, R.W. Schurko, R.J. Iulucci, Chemical shift tensors of cimetidine form a modeled with density functional theory calculations: implications for NMR crystallography, *J. Phys. Chem. A* 124 (2020) 3109–3119. <https://doi.org/10.1021/acs.jpca.0c00421>.
- [106] D.W. Alderman, G. McGeorge, J.Z. Hu, R.J. Pugmire, D.M. Grant, A sensitive, high resolution magic angle turning experiment for measuring chemical shift tensor principal values, *Mol. Phys.* 95 (1998) 1113–1126. <https://doi.org/10.1080/00268979809483243>.
- [107] S. Sturniolo, T.F.G. Green, R.M. Hanson, M. Zilka, K. Refson, P. Hodgkinson, S.P. Brown, J.R. Yates, Visualization and processing of computed solid-state NMR parameters: MagresView and MagresPython, *Solid State Nucl. Magn. Reson.* 78 (2016) 64–70. <https://doi.org/10.1016/j.ssnmr.2016.05.004>.
- [108] J. Czernek, J. Brus, Theoretical predictions of the two-dimensional solid-state NMR spectra: a case study of the <sup>13</sup>C–<sup>1</sup>H correlations in metergoline, *Chem. Phys. Lett.* 586 (2013) 56–60. <https://doi.org/10.1016/j.cplett.2013.09.015>.
- [109] J. Czernek, M. Urbanova, J. Brus, NMR crystallography of the polymorphs of metergoline, *Crystals* 8 (2018) 378. <https://doi.org/10.3390/cryst8100378>.

- [110] M. Hušák, A. Jegorov, J. Brus, W. van Beek, P. Pattison, M. Christensen, V. Favre-Nicolin, J. Maixner, Metergoline II: structure solution from powder diffraction data with preferred orientation and from microcrystal, *Struct. Chem.* 19 (2008) 517–525. <https://doi.org/10.1007/s11224-008-9312-0>.
- [111] J. Czernek, J. Brus, The covariance of the differences between experimental and theoretical chemical shifts as an aid for assigning two-dimensional heteronuclear correlation solid-state NMR spectra, *Chem. Phys. Lett.* 608 (2014) 334–339. <https://doi.org/10.1016/j.cplett.2014.05.099>.
- [112] M. Zilka, J.R. Yates, S.P. Brown, An NMR crystallography investigation of furose-mide, *Magn. Reson. Chem.* 57 (2018) 191–199. <https://doi.org/10.1002/mrc.4789>.
- [113] M. Zilka, S. Sturniolo, S.P. Brown, J.R. Yates, Visualising crystal packing interactions in solid-state NMR: concepts and applications, *J. Chem. Phys.* 147 (2017) 144203. <https://doi.org/10.1063/1.4996750>.
- [114] S. Sene, D. Berthomieu, B. Donnadiou, S. Richeter, J. Vezzani, D. Granier, S. Bégu, H. Mutin, C. Gervais, D. Laurencin, A combined experimental–computational study of benzoxaborole crystal structures, *CrstEngComm* 16 (2014) 4999–5011. <https://doi.org/10.1039/C4CE00313F>.
- [115] L. Mendez, G. Henriquez, S. Sirimulla, M. Narayan, Looking back, looking forward at halogen bonding in drug discovery, *Molecules* 22 (2017) 1397. <https://doi.org/10.3390/molecules22091397>.
- [116] Y. Lu, Y. Liu, Z. Xu, H. Li, H. Liu, W. Zhu, Halogen bonding for rational drug design and new drug discovery, *Expert Opin. Drug Discovery* 7 (2012) 375–383. <https://doi.org/10.1517/17460441.2012.678829>.
- [117] Z. Xu, Z. Yang, Y. Liu, Y. Lu, K. Chen, W. Zhu, Halogen bond: its role beyond drug–target binding affinity for drug discovery and development, *J. Chem. Inf. Model.* 54 (2014) 69–78. <https://doi.org/10.1021/ci400539q>.
- [118] Z. Xu, Z. Liu, T. Chen, T. Chen, Z. Wang, G. Tian, J. Shi, X. Wang, Y. Lu, X. Yan, G. Wang, H. Jiang, K. Chen, S. Wang, Y. Xu, J. Shen, W. Zhu, Utilization of halogen bond in lead optimization: a case study of rational design of potent phosphodiesterase type 5 (PDE5) inhibitors, *J. Med. Chem.* 54 (2011) 5607–5611. <https://doi.org/10.1021/jm200644r>.
- [119] S. Jiang, L. Zhang, D. Cui, Z. Yao, B. Gao, J. Lin, D. Wei, The important role of halogen bond in substrate selectivity of enzymatic catalysis, *Sci. Rep.* 6 (2016) 34750. <https://doi.org/10.1038/srep34750>.
- [120] J. Heidrich, L.E. Sperl, F.M. Boeckler, Embracing the diversity of halogen bonding motifs in fragment-based drug discovery—construction of a diversity-optimized halogen-enriched fragment library, *Front. Chem.* 7 (2019) 9. <https://doi.org/10.3389/fchem.2019.00009>.
- [121] M. Marín-Luna, R.M. Claramunt, C.I. Nieto, I. Alkorta, J. Elguero, F. Reviriego, A theoretical NMR study of polymorphism in crystal structures of azoles and benzazoles, *Magn. Reson. Chem.* 57 (2019) 275–284. <https://doi.org/10.1002/mrc.4824>.
- [122] J. Frelek, M. Górecki, A. Dziedzic, E. Jabłońska, B. Kamiński, R.K. Wojcieszczyk, R. Luboradzki, W.J. Szczepke, Comprehensive spectroscopic characterization of finasteride polymorphic forms. Does the form X exist? *J. Pharm. Sci.* 104 (2015) 1650–1657. <https://doi.org/10.1002/jps.24369>.
- [123] A. Othman, J.S.O. Evans, I.R. Evans, R.K. Harris, P. Hodgkinson, Structural study of polymorphs and solvates of finasteride, *J. Pharm. Sci.* 96 (2007) 1380–1397. <https://doi.org/10.1002/jps.20940>.
- [124] J. Bernstein, A.T. Hagler, Conformational polymorphism. The influence of crystal structure on molecular conformation, *J. Am. Chem. Soc.* 100 (1978) 673–681, <https://doi.org/10.1021/ja00471a001>.



- [125] A. Nangia, Conformational polymorphism in organic crystals, *Acc. Chem. Res.* 41 (2008) 595–604. <https://doi.org/10.1021/ar700203k>.
- [126] A.J. Cruz-Cabeza, J. Bernstein, Conformational polymorphism, *Chem. Rev.* 114 (2014) 2170–2191. <https://doi.org/10.1021/cr400249d>.
- [127] S. Millan, J. Nasir, B. Gil-Hernández, T.-O. Knedel, B. Moll, I. Boldog, O. Weingart, J.S.a. der Günsse, C. Janiak, Solid-state landscape of 4,4'-Azobis(3,5-dimethyl-1H-pyrazole) with the isolation of conformer-dependent polymorphs, *Cryst. Growth Des.* 20 (2020) 2721–2733. <https://doi.org/10.1021/acs.cgd.0c00118>.
- [128] C.A. Rezende, R.A.S. San Gil, L.B. Borré, J.R. Pires, V.S. Vaiss, J.A.L.C. Resende, A.A. Leitão, R.B. De Alencastro, K.Z. Leal, Combining nuclear magnetic resonance spectroscopy and density functional theory calculations to characterize carvedilol polymorphs, *J. Pharm. Sci.* 105 (2016) 2648–2655. <https://doi.org/10.1002/jps.24641>.
- [129] M. Zielińska-pisklak, D.M. Pisklak, I. Wawer, Application of  $^{13}\text{C}$  CPMAS NMR for qualitative and quantitative characterization of carvedilol and its commercial formulations, *J. Pharm. Sci.* 101 (2012) 1763–1772. <https://doi.org/10.1002/jps.23062>.
- [130] L.D. Prado, H.V.A. Rocha, J.A.L.C. Resende, G.B. Ferreira, A.M.R. de F. Teixeira, An insight into carvedilol solid forms: effect of supramolecular interactions on the dissolution profiles, *CrystEngComm* 16 (2014) 3168–3179. <https://doi.org/10.1039/C3CE42403K>.
- [131] E. Pindelska, L. Szeleszczuk, D.M. Pisklak, A. Mazurek, W. Kolodziejski, Solid-state NMR as an effective method of polymorphic analysis: solid dosage forms of clopidogrel hydrogensulfate, *J. Pharm. Sci.* 104 (2015) 106–113. <https://doi.org/10.1002/jps.24249>.
- [132] R.K. Harris, S. Cadars, L. Emsley, J.R. Yates, C.J. Pickard, R.K.R. Jetti, U.J. Griesser, NMR Crystallography of oxybuprocaine hydrochloride, modification II<sup>o</sup>, *Phys. Chem. Chem. Phys.* 9 (2007) 360–368. <https://doi.org/10.1039/B614318K>.
- [133] G.A. Facey, T.J. Connolly, C. Bensimon, T. Durst, A solid state NMR and X-ray crystallographic investigation of dynamic disorder in solid tetrahydronaphthalene derivatives, *Can. J. Chem.* 74 (1996) 1844–1851. <https://doi.org/10.1139/v96-206>.
- [134] L. Rajput, M. Banik, J.R. Yarava, S. Joseph, M.K. Pandey, Y. Nishiyama, G.R. Desiraju, Exploring the salt–cocrystal continuum with solid-state NMR using natural-abundance samples: implications for crystal engineering, *IUCrJ* 4 (2017) 466–475. <https://doi.org/10.1107/S205225251700687X>.
- [135] E.A. Losev, E.V. Boldyreva, A salt or a co-crystal—when crystallization protocol matters, *CrystEngComm* 20 (2018) 2299–2305. <https://doi.org/10.1039/C7CE02204B>.
- [136] P. Stainton, T. Grecu, J. McCabe, T. Munshi, E. Nauha, I.J. Scowen, N. Blagden, First comparative study of the three polymorphs of bis(isonicotinamide) citric acid cocrystals and the concomitant salt 4-carbamoylpyridinium citrate isonicotinamide, *Cryst. Growth Des.* 18 (2018) 4150–4159. <https://doi.org/10.1021/acs.cgd.8b00597>.
- [137] C.L. Jones, J.M. Skelton, S.C. Parker, P.R. Raithby, A. Walsh, C.C. Wilson, L.H. Thomas, Living in the salt–cocrystal continuum: indecisive organic complexes with thermochromic behaviour, *CrystEngComm* 21 (2019) 1626–1634. <https://doi.org/10.1039/C8CE02066C>.
- [138] S.R. Perumalla, C. Wang, Y. Guo, L. Shi, C.C. Sun, Robust bulk preparation and characterization of sulfamethazine and saccharine salt and cocrystal polymorphs, *CrystEngComm* 21 (2019) 2089–2096. <https://doi.org/10.1039/C8CE01076E>.
- [139] D. Bernasconi, S. Bordignon, F. Rossi, E. Priola, C. Nervi, R. Gobetto, D. Voinovich, D. Hasa, N.T. Duong, Y. Nishiyama, M.R. Chierotti, Selective synthesis of a salt and a cocrystal of the ethionamide–salicylic acid system, *Cryst. Growth Des.* 20 (2020) 906–915. <https://doi.org/10.1021/acs.cgd.9b01299>.

- [140] M.R. Chierotti, R. Gobetto, Solid-state NMR studies of weak interactions in supramolecular systems, *Chem. Commun.* (2008) 1621–1634. <https://doi.org/10.1039/B711551B>.
- [141] C.P. Romao, F.A. Perras, U. Werner-Zwanziger, J.A. Lussier, K.J. Miller, C.M. Calahoo, J.W. Zwanziger, M. Bieringer, B.A. Marinkovic, D.L. Bryce, M.A. White, Zero thermal expansion in  $\text{ZrMgMo}_3\text{O}_{12}$ : NMR crystallography reveals origins of thermoelastic properties, *Chem. Mater.* 27 (2015) 2633–2646. <https://doi.org/10.1021/acs.chemmater.5b00429>.
- [142] C.M. Widdifield, I. Moudrakovski, D.L. Bryce, Calcium-43 chemical shift and electric field gradient tensor interplay: a sensitive probe of structure, polymorphism, and hydration, *Phys. Chem. Chem. Phys.* 16 (2014) 13340–13359. <https://doi.org/10.1039/C4CP01180E>.
- [143] D. Laurencin, A. Wong, J.V. Hanna, R. Dupree, M.E. Smith, A high-resolution  $^{43}\text{Ca}$  solid-state NMR study of the calcium sites of hydroxyapatite, *J. Am. Chem. Soc.* 130 (2008) 2412–2413. <https://doi.org/10.1021/ja710557t>.
- [144] D. Laurencin, C. Gervais, A. Wong, C. Coelho, F. Mauri, D. Massiot, M.E. Smith, C. Bonhomme, Implementation of high resolution  $^{43}\text{Ca}$  solid state NMR spectroscopy: toward the elucidation of calcium sites in biological materials, *J. Am. Chem. Soc.* 131 (2009) 13430–13440. <https://doi.org/10.1021/ja904553q>.
- [145] K.M.N. Burgess, D.L. Bryce, On the crystal structure of the vaterite polymorph of  $\text{CaCO}_3$ : a calcium-43 solid-state NMR and computational assessment, *Solid State Nucl. Magn. Reson.* 65 (2015) 75–83. <https://doi.org/10.1016/j.ssnmr.2014.08.003>.
- [146] W.D. Wang, X. Gao, M. Strohmeier, W. Wang, S. Bai, C. Dybowski, Solid-state NMR studies of form I of atorvastatin calcium, *J. Phys. Chem. B* 116 (2012) 3641–3649. <https://doi.org/10.1021/jp212074a>.
- [147] C.M. Widdifield, Chapter five—applications of solid-state  $^{43}\text{Ca}$  nuclear magnetic resonance: superconductors, glasses, biomaterials, and NMR crystallography, in: G.A. Webb (Ed.), *Annu. Rep. NMR Spectrosc.* 2017, pp. 227–363. <https://doi.org/10.1016/bs.arnmr.2017.04.006>.
- [148] H. Colas, L. Bonhomme-Courry, C.C. Diogo, F. Tielens, F. Babonneau, C. Gervais, D. Bazin, D. Laurencin, M.E. Smith, J.V. Hanna, M. Daudon, C. Bonhomme, Whewellite,  $\text{CaC}_2\text{O}_4 \cdot \text{H}_2\text{O}$ : structural study by a combined NMR, crystallography and modelling approach, *CrystEngComm* 15 (2013) 8840–8847. <https://doi.org/10.1039/C3CE41201F>.
- [149] S.T. Holmes, W.D. Wang, G. Hou, C. Dybowski, W. Wang, S. Bai, A new NMR crystallographic approach to reveal the calcium local structure of atorvastatin calcium, *Phys. Chem. Chem. Phys.* 21 (2019) 6319–6326. <https://doi.org/10.1039/C8CP07673A>.
- [150] T. Bataille, A. Bouhali, C. Kouvatas, C. Trifa, N. Audebrand, C. Boudaren, Hydrates and polymorphs of lead squarate  $\text{Pb}(\text{C}_4\text{O}_4)$ : structural transformations studied by *in situ* X-ray powder diffraction and solid state NMR, *Polyhedron* 164 (2019) 123–131. <https://doi.org/10.1016/j.poly.2019.02.047>.
- [151] S.A. Southern, D. Errulat, J.M. Frost, B. Gabidullin, D.L. Bryce, Prospects for  $^{207}\text{Pb}$  solid-state NMR studies of lead tetrel bonds, *Faraday Discuss.* 203 (2017) 165–186. <https://doi.org/10.1039/C7FD00087A>.
- [152] Y. Xu, S.A. Southern, P.M.J. Szell, D.L. Bryce, The role of solid-state nuclear magnetic resonance in crystal engineering, *CrystEngComm* 18 (2016) 5236–5252. <https://doi.org/10.1039/C6CE01206J>.
- [153] Y. Xu, P.M.J. Szell, V. Kumar, D.L. Bryce, Solid-state NMR spectroscopy for the analysis of element-based non-covalent interactions, *Coord. Chem. Rev.* 411 (2020) 213237. <https://doi.org/10.1016/j.ccr.2020.213237>.



- [154] E. Arunan, G.R. Desiraju, R.A. Klein, J. Sadlej, S. Scheiner, I. Alkorta, D.C. Clary, R.H. Crabtree, J.J. Dannenberg, P. Hobza, H.G. Kjaergaard, A.C. Legon, B. Mennucci, D.J. Nesbitt, Definition of the hydrogen bond (IUPAC Recommendations 2011), *Pure Appl. Chem.* 83 (2011) 1637–1641. <https://doi.org/10.1351/PAC-REC-10-01-02>.
- [155] R. Thakuria, N.K. Nath, B.K. Saha,  $\pi$ - $\pi$  stacking in crystal engineering: fundamentals and applications, *Cryst. Growth Des.* 19 (2019) 523–528. <https://doi.org/10.1021/cgdefu>. [http://web.archive.org/web/20200705142102/https://pubs.acs.org/page/cgdefu/vi/20.html?ref=vi\\_collection](http://web.archive.org/web/20200705142102/https://pubs.acs.org/page/cgdefu/vi/20.html?ref=vi_collection).
- [156] S. Grzesiek, F. Cordier, A.J. Dingley, Hydrogen bond scalar couplings—a new tool in biomolecular NMR, in: N.R. Krishna, L.J. Berliner (Eds.), *Protein NMR* Millenn, Springer, Boston, MA, 2002, pp. 255–283. [https://doi.org/10.1007/0-306-47936-2\\_9](https://doi.org/10.1007/0-306-47936-2_9).
- [157] S. Grzesiek, E.D. Becker, Hydrogen bonding, in: R.K. Harris, R.E. Wasylishen (Eds.), *EMagRes*, 2011. <https://doi.org/10.1002/9780470034590.emrstm0216.pub2>.
- [158] G.J. Korinek, W.G. Schneider, On the proton magnetic resonance shift due to hydrogen bonding, *Can. J. Chem.* 35 (1957) 1157–1163. <https://doi.org/10.1139/v57-156>.
- [159] S.P. Brown, Hydrogen bonding in crystalline organic solids, in: R.K. Harris, R.E. Wasylishen (Eds.), *EMagRes*, 2008. <https://doi.org/10.1002/9780470034590.emrstm1006>.
- [160] T. Clark, M. Hennemann, J.S. Murray, P. Politzer, Halogen bonding: the  $\sigma$ -hole, *J. Mol. Model.* 13 (2007) 291–296. <https://doi.org/10.1007/s00894-006-0130-2>.
- [161] G. Cavallo, P. Metrangolo, T. Pilati, G. Resnati, G. Terraneo, Naming interactions from the electrophilic site, *Cryst. Growth Des.* 14 (2014) 2697–2702. <https://doi.org/10.1021/cg5001717>.
- [162] G.R. Desiraju, P.S. Ho, L. Kloo, A.C. Legon, R. Marquardt, P. Metrangolo, P. Politzer, G. Resnati, K. Rissanen, Definition of the halogen bond (IUPAC recommendations 2013), *Pure Appl. Chem.* 85 (2013) 1711–1713. <https://doi.org/10.1351/PAC-REC-12-05-10>.
- [163] C.B. Aakeroy, D.L. Bryce, G.R. Desiraju, A. Frontera, A.C. Legon, F. Nicotra, K. Rissanen, S. Scheiner, G. Terraneo, P. Metrangolo, G. Resnati, Definition of the chalcogen bond (IUPAC recommendations 2019), *Pure Appl. Chem.* 91 (2019) 1889–1892. <https://doi.org/10.1515/pac-2018-0713>.
- [164] S. Zahn, R. Frank, E. Hey-Hawkins, B. Kirchner, Pnictogen bonds: a new molecular linker? *Chem. A Eur. J.* 17 (2011) 6034–6038. <https://doi.org/10.1002/chem.201002146>.
- [165] A. Bauzá, T.J. Mooibroek, A. Frontera, Tetrel-bonding interaction: rediscovered supramolecular force? *Angew. Chem. Int. Ed.* 52 (2013) 12317–12321. <https://doi.org/10.1002/anie.201306501>.
- [166] A. Bauzá, A. Frontera, Aerogen bonding interaction: a new supramolecular force? *Angew. Chem. Int. Ed.* 54 (2015) 7340–7343. <https://doi.org/10.1002/anie.201502571>.
- [167] J. Lu, S. Scheiner, Effects of halogen, chalcogen, pnictogen, and tetrel bonds on IR and NMR spectra, *Molecules* 24 (2019) 2822. <https://doi.org/10.3390/molecules24152822>.
- [168] V. Kumar, Y. Xu, C. Leroy, D.L. Bryce, Direct investigation of chalcogen bonds by multinuclear solid-state magnetic resonance and vibrational spectroscopy, *Phys. Chem. Chem. Phys.* 22 (2020) 3817–3824. <https://doi.org/10.1039/C9CP06267J>.
- [169] V. Kumar, Y. Xu, D.L. Bryce, Double chalcogen bonds: crystal engineering stratagems via diffraction and multinuclear solid-state magnetic resonance spectroscopy, *Chem. A Eur. J.* 26 (2020) 3275–3286. <https://doi.org/10.1002/chem.201904795>.

- [170] R. Mokrai, J. Barrett, D.C. Apperley, A.S. Batsanov, Z. Benkő, D. Heift, Weak pnictogen bond with bismuth: experimental evidence based on Bi–P through-space coupling, *Chem. A Eur. J.* 25 (2019) 4017–4024. <https://doi.org/10.1002/chem.201900266>.
- [171] A.J. Horsewill, A. Ikram, Experimental investigations of the quantum dynamics of the hydrogen bond using single crystal NMR, *Phys. B Condens. Matter* 226 (1996) 202–206. [https://doi.org/10.1016/0921-4526\(96\)00303-1](https://doi.org/10.1016/0921-4526(96)00303-1).
- [172] A. Detken, H. Zimmermann, U. Haeberlen, Z. Luz, Dynamic hydrogen disorder in solid tropolone. a single-crystal NMR study of the hydroxyl deuterons, *J. Magn. Reson.* 126 (1997) 95–102. <https://doi.org/10.1006/jmre.1997.1147>.
- [173] R. Gerald II, T. Bernhard, U. Haeberlen, J. Rendell, S. Opella, Chemical shift and electric field gradient tensors for the amide and carboxyl hydrogens in the model peptide N-acetyl-D,L-valine. Single-crystal deuterium NMR study, *J. Am. Chem. Soc.* 115 (1993) 777–782. <https://doi.org/10.1021/ja00055a058>.
- [174] N. Takeda, S. Kuroki, H. Kurosu, I. Ando,  $^{13}\text{C}$ -NMR chemical shift tensor and hydrogen-bonded structure of glycine-containing peptides in a single crystal, *Biopolymers* 50 (1999) 61–69. [https://doi.org/10.1002/\(SICI\)1097-0282\(199907\)50:1<61::AID-BIP6>3.0.CO;2-9](https://doi.org/10.1002/(SICI)1097-0282(199907)50:1<61::AID-BIP6>3.0.CO;2-9).
- [175] K. Takegoshi, A. Naito, C.A. McDowell, Intermolecular hydrogen-bonding effects on the  $^{13}\text{C}$  NMR shielding tensor of the carbonyl carbon nucleus in a single crystal of dimedone, *J. Magn. Reson.* 1969 (65) (1985) 34–42. [https://doi.org/10.1016/0022-2364\(85\)90373-7](https://doi.org/10.1016/0022-2364(85)90373-7).
- [176] G.S. Harbison, L.W. Jelinsiu, R.E. Stark, D.A. Torchia, J. Herzfeld, R.G. Griffin,  $^{15}\text{N}$  chemical shift and  $^{15}\text{N}$ – $^{13}\text{C}$  dipolar tensors for the peptide bond in [ $^{13}\text{C}$ ]Glycyl[ $^{15}\text{N}$ ] glycine hydrochloride monohydrate, *J. Magn. Reson.* 60 (1984) 79–82. [https://doi.org/10.1016/0022-2364\(84\)90027-1](https://doi.org/10.1016/0022-2364(84)90027-1).
- [177] Y. Xu, B. Gabidullin, D.L. Bryce, Single-crystal NMR characterization of halogen bonds, *J. Phys. Chem. A* 123 (2019) 6194–6209. <https://doi.org/10.1021/acs.jpca.9b03587>.
- [178] D. Gołowicz, P. Kasprzak, V. Orekhov, K. Kazimierczuk, Fast time-resolved NMR with non-uniform sampling, *Prog. Nucl. Magn. Reson. Spectrosc.* 116 (2020) 40–55. <https://doi.org/10.1016/j.pnmrs.2019.09.003>.
- [179] I. Halasz, S.A.J. Kimber, P.J. Beldon, A.M. Belenguer, F. Adams, V. Honkimäki, R.C. Nightingale, R.E. Dinnebier, T. Friščić, *In situ* and real-time monitoring of mechanochemical milling reactions using synchrotron X-ray diffraction, *Nat. Protoc.* 8 (2013) 1718–1729. <https://doi.org/10.1038/nprot.2013.100>.
- [180] P.A. Julien, K. Užarević, A.D. Katsenis, S.A.J. Kimber, T. Wang, O.K. Farha, Y. Zhang, J. Casaban, L.S. Germann, M. Etter, R.E. Dinnebier, S.L. James, I. Halasz, T. Friščić, *In Situ* monitoring and mechanism of the mechanochemical formation of a microporous MOF-74 framework, *J. Am. Chem. Soc.* 138 (2016) 2929–2932. <https://doi.org/10.1021/jacs.5b13038>.
- [181] T. Stolar, L. Batzdorf, S. Lukin, D. Žilić, C. Motillo, T. Friščić, F. Emmerling, I. Halasz, K. Užarević, *In situ* monitoring of the mechanosynthesis of the archetypal metal–organic framework HKUST-1: effect of liquid additives on the milling reactivity, *Inorg. Chem.* 56 (2017) 6599–6608. <https://doi.org/10.1021/acs.inorgchem.7b00707>.
- [182] A.D. Katsenis, A. Puškarić, V. Štrukil, C. Mottillo, P.A. Julien, K. Užarević, M.-H. Pham, T.-O. Do, S.A.J. Kimber, P. Lazić, O. Magdysyuk, R.E. Dinnebier, I. Halasz, T. Friščić, *In situ* X-ray diffraction monitoring of a mechanochemical reaction reveals a unique topology metal–organic framework, *Nat. Commun.* 6 (2015) 6662. <https://doi.org/10.1038/ncomms7662>.

- [183] I. Halasz, T. Friščić, S.A.J. Kimber, K. Užarević, A. Puškarić, C. Mottillo, P. Julien, V. Štrukil, V. Honkimäki, R.E. Dinnebier, Quantitative *in situ* and real-time monitoring of mechanochemical reactions, *Faraday Discuss.* 170 (2014) 203–221. <https://doi.org/10.1039/C4FD00013G>.
- [184] L.S. Germann, A.D. Katsenis, I. Huskić, P.A. Julien, K. Užarević, M. Etter, O.K. Farha, T. Friščić, R.E. Dinnebier, Real-time *in situ* monitoring of particle and structure evolution in the mechanochemical synthesis of UiO-66 metal–organic frameworks, *Cryst. Growth Des.* 20 (2020) 49–54. <https://doi.org/10.1021/acs.cgd.9b01477>.
- [185] I. Halasz, A. Puškarić, S.A.J. Kimber, P.J. Beldon, A.M. Belenguer, F. Adams, V. Honkimäki, R.E. Dinnebier, B. Patel, W. Jones, V. Štrukil, T. Friščić, Real-time *in situ* powder X-ray diffraction monitoring of mechanochemical synthesis of pharmaceutical cocrystals, *Angew. Chem. Int. Ed.* 52 (2013) 11538–11541. <https://doi.org/10.1002/anie.201305928>.
- [186] P.A. Julien, I. Malvestiti, T. Friščić, The effect of milling frequency on a mechanochemical organic reaction monitored by *in situ* Raman spectroscopy, *Beilstein J. Org. Chem.* 13 (2017) 2160–2168. <https://doi.org/10.3762/bjoc.13.216>.
- [187] D. Gracin, V. Štrukil, T. Friščić, I. Halasz, K. Užarević, Laboratory real-time and *in situ* monitoring of mechanochemical milling reactions by Raman spectroscopy, *Angew. Chem. Int. Ed.* 53 (2014) 6193–6197. <https://doi.org/10.1002/anie.201402334>.
- [188] L. Batzdorf, F. Fischer, M. Wilke, K.-J. Wenzel, F. Emmerling, Direct *in situ* investigation of milling reactions using combined x-ray diffraction and Raman spectroscopy, *Angew. Chem. Int. Ed.* 54 (2015) 1799–1802. <https://doi.org/10.1002/anie.201409834>.
- [189] V.S. Mandala, S.J. Loewus, M.A. Mehta, Monitoring cocrystal formation via *in situ* solid-state NMR, *J. Phys. Chem. Lett.* 5 (2014) 3340–3344. <https://doi.org/10.1021/jz501699h>.
- [190] C.E. Hughes, P.A. Williams, T.R. Peskett, K.D.M. Harris, Exploiting *in situ* solid-state NMR for the discovery of new polymorphs during crystallization processes, *J. Phys. Chem. Lett.* 3 (2012) 3176–3181. <https://doi.org/10.1021/jz301252u>.
- [191] C.E. Hughes, P.A. Williams, K.D.M. Harris, “CLASSIC NMR”: an *in-situ* NMR strategy for mapping the time-evolution of crystallization processes by combined liquid-state and solid-state measurements, *Angew. Chem. Int. Ed.* 53 (2014) 8939–8943. <https://doi.org/10.1002/anie.201404266>.
- [192] C.E. Hughes, P.A. Williams, V.L. Keast, V.G. Charalampopoulos, G.R. Edwards-Gau, K.D.M. Harris, New *in situ* solid-state NMR techniques for probing the evolution of crystallization processes: pre-nucleation, nucleation and growth, *Faraday Discuss.* 179 (2015) 115–140. <https://doi.org/10.1039/C4FD00215F>.
- [193] K.D.M. Harris, C.E. Hughes, P.A. Williams, Monitoring the evolution of crystallization processes by *in-situ* solid-state NMR spectroscopy, *Solid State Nucl. Magn. Reson.* 65 (2015) 107–113. <https://doi.org/10.1016/j.ssnmr.2014.11.004>.
- [194] W. Xu, Q. Zhu, C. Hu, The structure of glycine dihydrate: implications for the crystallization of glycine from solution and its structure in outer space, *Angew. Chem. Int. Ed.* 56 (2017) 2030–2034. <https://doi.org/10.1002/anie.201610977>.
- [195] P. Cerreia Vioglio, G. Mollica, M. Juramy, C.E. Hughes, P.A. Williams, F. Ziarelli, S. Viel, P. Thureau, K.D.M. Harris, Insights into the crystallization and structural evolution of glycine dihydrate by *in situ* solid-state NMR spectroscopy, *Angew. Chem. Int. Ed.* 57 (2018) 6619–6623. <https://doi.org/10.1002/anie.201801114>.
- [196] Y. Xu, L. Champion, B. Gabidullin, D.L. Bryce, A kinetic study of mechanochemical halogen bond formation by *in situ*  $^{31}\text{P}$  solid-state NMR spectroscopy, *Chem. Commun.* 53 (2017) 9930–9933. <https://doi.org/10.1039/C7CC05051H>.

- [197] I.I. Ivanova, Y.G. Kolyagin, I.A. Kasyanov, A.V. Yakimov, T.O. Bok, D.N. Zarubin, Time-resolved in situ MAS NMR monitoring of the nucleation and growth of zeolite BEA catalysts under hydrothermal conditions, *Angew. Chem. Int. Ed.* 56 (2017) 15344–15347. <https://doi.org/10.1002/anie.201709039>.
- [198] Y. Xu, J. Viger-Gravel, I. Korobkov, D.L. Bryce, Mechanochemical production of halogen-bonded solids featuring  $P=O\cdots I-C$  motifs and characterization via X-ray diffraction, solid-state multinuclear magnetic resonance, and density functional theory, *J. Phys. Chem. C* 119 (2015) 27104–27117. <https://doi.org/10.1021/acs.jpcc.5b09737>.
- [199] A.A. Peach, D.A. Hirsh, S.T. Holmes, R.W. Schurko, Mechanochemical syntheses and  $^{35}\text{Cl}$  solid-state NMR characterization of fluoxetine HCl cocrystals, *CrystEngComm* 20 (2018) 2780–2792. <https://doi.org/10.1039/C8CE00378E>.
- [200] T.-X. Métro, C. Gervais, A. Martinez, C. Bonhomme, D. Laurencin, Unleashing the potential of  $^{17}\text{O}$  NMR spectroscopy using mechanochemistry, *Angew. Chem. Int. Ed.* 56 (2017) 6803–6807. <https://doi.org/10.1002/anie.201702251>.
- [201] C.-H. Chen, E. Gaillard, F. Mentink-Vigier, K. Chen, Z. Gan, P. Gaveau, B. Rebière, R. Berthelot, P. Florian, C. Bonhomme, M.E. Smith, T.-X. Métro, B. Alonso, D. Laurencin, Direct  $^{17}\text{O}$  isotopic labeling of oxides using mechanochemistry, *Inorg. Chem.* 59 (2020) 13050–13066. <https://doi.org/10.1021/acs.inorgchem.0c00208>.
- [202] M. Schröder (Ed.), *Functional Metal-Organic Frameworks: Gas Storage, Separation and Catalysis*, Springer-Verlag, Berlin Heidelberg, 2010.
- [203] D. Farrusseng (Ed.), *Metal-Organic Frameworks: Applications from Catalysis to Gas Storage*, Wiley-VCH Verlag & Co. KGaA, Weinheim, 2011.
- [204] H. Furukawa, K.E. Cordova, M. O’Keeffe, O.M. Yaghi, The chemistry and applications of metal-organic frameworks, *Science* 341 (2013), 1230444. <https://doi.org/10.1126/science.1230444>.
- [205] U. Mueller, M. Schubert, F. Teich, H. Puetter, K. Schierle-Arndt, J. Pastré, Metal-organic frameworks—prospective industrial applications, *J. Mater. Chem.* 16 (2006) 626–636. <https://doi.org/10.1039/B511962F>.
- [206] A.U. Czaja, N. Trukhan, U. Müller, Industrial applications of metal-organic frameworks, *Chem. Soc. Rev.* 38 (2009) 1284–1293. <https://doi.org/10.1039/B804680H>.
- [207] L. Jiao, Y. Wang, H.-L. Jiang, Q. Xu, Metal-organic frameworks as platforms for catalytic applications, *Adv. Mater.* 30 (2018) 1703663. <https://doi.org/10.1002/adma.201703663>.
- [208] J. Liu, L. Chen, H. Cui, J. Zhang, L. Zhang, C.-Y. Su, Applications of metal-organic frameworks in heterogeneous supramolecular catalysis, *Chem. Soc. Rev.* 43 (2014) 6011–6061. <https://doi.org/10.1039/C4CS00094C>.
- [209] M. Gaab, N. Trukhan, S. Maurer, R. Gummaraju, U. Müller, The progression of Al-based metal-organic frameworks—from academic research to industrial production and applications, *Microporous Mesoporous Mater.* 157 (2012) 131–136. <https://doi.org/10.1016/j.micromeso.2011.08.016>.
- [210] P.A. Julien, C. Mottillo, T. Frišćić, Metal-organic frameworks meet scalable and sustainable synthesis, *Green Chem.* 19 (2017) 2729–2747. <https://doi.org/10.1039/C7GC01078H>.
- [211] C.A. O’Keefe, C. Mottillo, J. Vainauskas, L. Fábíán, T. Frišćić, R.W. Schurko, NMR-enhanced crystallography aids open metal-organic framework discovery using solvent-free accelerated aging, *Chem. Mater.* 32 (2020) 4273–4281. <https://doi.org/10.1021/acs.chemmater.0c00894>.
- [212] M.R. Chierotti, R. Gobetto, L. Pellegrino, L. Milone, P. Venturello, Mechanically induced phase change in barbituric acid, *Cryst. Growth Des.* 8 (2008) 1454–1457. <https://doi.org/10.1021/cg701214k>.

- [213] M.R. Chierotti, L. Ferrero, N. Garino, R. Gobetto, L. Pellegrino, D. Braga, F. Grepioni, L. Maini, The richest collection of tautomeric polymorphs: the case of 2-thiobarbituric acid, *Chem. A Eur. J.* 16 (2010) 4347–4358. <https://doi.org/10.1002/chem.200902485>.
- [214] N. Zencirci, U.J. Griesser, T. Gelbrich, D.C. Apperley, R.K. Harris, Crystal polymorphs of barbitol: news about a classic polymorphic system, *Mol. Pharm.* 11 (2014) 338–350. <https://doi.org/10.1021/mp400515f>.
- [215] F.A. Perras, D.L. Bryce, Symmetry-amplified J splittings for quadrupolar spin pairs: a solid-state NMR probe of homoatomic covalent bonds, *J. Am. Chem. Soc.* 135 (2013) 12596–12599. <https://doi.org/10.1021/ja407138b>.
- [216] F.A. Perras, D.L. Bryce, Direct characterization of metal–metal bonds between nuclei with strong quadrupolar interactions via NMR spectroscopy, *J. Phys. Chem. Lett.* 5 (2014) 4049–4054. <https://doi.org/10.1021/jz5023448>.
- [217] S. d'Agostino, L. Fornasari, F. Grepioni, D. Braga, F. Rossi, M.R. Chierotti, R. Gobetto, Precessional motion in crystalline solid solutions of ionic rotors, *Chem. A Eur. J.* 24 (2018) 15059–15066. <https://doi.org/10.1002/chem.201803071>.
- [218] T. Apih, V. Žagar, J. Seliger, NMR and NQR study of polymorphism in carbamazepine, *Solid State Nucl. Magn. Reson.* 107 (2020) 101653. <https://doi.org/10.1016/j.ssnmr.2020.101653>.
- [219] P.A. Beckmann, K.S. Burbank, K.M. Clemons, E.N. Slonaker, K. Averill, C. Dybowski, J.S. Figueroa, A. Glatfelter, S. Koch, L.M. Liable-Sands, A.L. Rheingold,  $^1\text{H}$  nuclear magnetic resonance spin–lattice relaxation,  $^{13}\text{C}$  magic-angle-spinning nuclear magnetic resonance spectroscopy, differential scanning calorimetry, and x-ray diffraction of two polymorphs of 2,6-di-*tert*-butylnaphthalene, *J. Chem. Phys.* 113 (2000) 1958–1965. <https://doi.org/10.1063/1.482000>.
- [220] A.L. Rheingold, J.S. Figueroa, C. Dybowski, P.A. Beckmann, Superlattices, polymorphs and solid-state NMR spin–lattice relaxation ( $T_1$ ) measurements of 2,6-di-*tert*-butylnaphthalene, *Chem. Commun.* (2000) 651–652. <https://doi.org/10.1039/A909449K>.
- [221] P.A. Beckmann, J. Ford, W.P. Malachowski, A.R. McGhie, C.E. Moore, A.L. Rheingold, G.J. Sloan, S.T. Szewczyk, Proton spin–lattice relaxation in organic molecular solids: polymorphism and the dependence on sample preparation, *ChemPhysChem* 19 (2018) 2423–2436. <https://doi.org/10.1002/cphc.201800237>.
- [222] J. Bernstein, R.J. Davey, J.-O. Henck, Concomitant polymorphs, *Angew. Chem. Int. Ed.* 38 (1999) 3440–3461. [https://doi.org/10.1002/\(SICI\)1521-3773\(19991203\)38:23<3440::AID-ANIE3440>3.0.CO;2-%23](https://doi.org/10.1002/(SICI)1521-3773(19991203)38:23<3440::AID-ANIE3440>3.0.CO;2-%23).
- [223] P.A. Beckmann, P.R. Rablen, J. Schmink, S.T. Szewczyk, A.L. Rheingold, Concomitant polymorphism in an organic solid: molecular and crystal structure and intra- and intermolecular potential contributions to *tert*-butyl and methyl group rotation, *ChemPhysChem* 20 (2019) 2887–2894. <https://doi.org/10.1002/cphc.201900436>.
- [224] R. Quinones, R.J. Iulucci, G. Behnke, R. Brown, D. Shoup, T.M. Riedel, C. Playchak, B.E. Lininger, J.M. Spehar, Moving towards fast characterization of polymorphic drugs by solid-state NMR spectroscopy, *J. Pharm. Biomed. Anal.* 148 (2018) 163–169. <https://doi.org/10.1016/j.jpba.2017.09.027>.
- [225] S. Jayanthi, A. Lupulescu, Sensitivity enhancement in 2D double cross polarization experiments under fast MAS by recycling unused protons, *Solid State Nucl. Magn. Reson.* 107 (2020) 101652. <https://doi.org/10.1016/j.ssnmr.2020.101652>.
- [226] C. Yan, F. Kayser, R. Dieden, Sensitivity enhancement via multiple contacts in the  $\{^1\text{H}-^{29}\text{Si}\}-^1\text{H}$  cross polarization experiment: a case study of modified silica nanoparticle surfaces, *RSC Adv.* 10 (2020) 23016–23023. <https://doi.org/10.1039/D0RA04995F>.

- [227] Z. Gan, Perspectives on high-field and solid-state NMR methods of quadrupole nuclei, *J. Magn. Reson.* 306 (2019) 86–90. <https://doi.org/10.1016/j.jmr.2019.07.028>.
- [228] L. Zhao, A.C. Pinon, L. Emsley, A.J. Rossini, DNP-enhanced solid-state NMR spectroscopy of active pharmaceutical ingredients, *Magn. Reson. Chem.* 56 (2018) 583–609. <https://doi.org/10.1002/mrc.4688>.
- [229] T. Maly, G.T. Debelouchina, V.S. Bajaj, K.-N. Hu, C.-G. Joo, M.L. Mak-Jurkauskas, J.R. Sirigiri, P.C.A. van der Wel, J. Herzfeld, R.J. Temkin, R.G. Griffin, Dynamic nuclear polarization at high magnetic fields, *J. Chem. Phys.* 128 (2008), 052211. <https://doi.org/10.1063/1.2833582>.
- [230] R.G. Griffin, T.F. Prisner, High field dynamic nuclear polarization—the renaissance, *Phys. Chem. Chem. Phys.* 12 (2010) 5737–5740. <https://doi.org/10.1039/C0CP90019B>.
- [231] Q.Z. Ni, E. Daviso, T.V. Can, E. Markhasin, S.K. Jawla, T.M. Swager, R.J. Temkin, J. Herzfeld, R.G. Griffin, High frequency dynamic nuclear polarization, *Acc. Chem. Res.* 46 (2013) 1933–1941. <https://doi.org/10.1021/ar300348n>.
- [232] A.J. Rossini, A. Zagdoun, M. Lelli, A. Lesage, C. Copéret, L. Emsley, Dynamic nuclear polarization surface enhanced NMR spectroscopy, *Acc. Chem. Res.* 46 (2013) 1942–1951. <https://doi.org/10.1021/ar300322x>.
- [233] L. Zhao, M.P. Hanrahan, P. Chakravarty, A.G. DiPasquale, L.E. Sirois, K. Nagapudi, J.W. Lubach, A.J. Rossini, Characterization of pharmaceutical cocrystals and salts by dynamic nuclear polarization-enhanced solid-state NMR spectroscopy, *Cryst. Growth Des.* 18 (2018) 2588–2601. <https://doi.org/10.1021/acs.cgd.8b00203>.
- [234] J. Viger-Gravel, C.E. Avalos, D.J. Kubicki, D. Gajan, M. Lelli, O. Ouari, A. Lesage, L. Emsley,  $^{19}\text{F}$  magic angle spinning dynamic nuclear polarization enhanced NMR spectroscopy, *Angew. Chem. Int. Ed.* 58 (2019) 7249–7253. <https://doi.org/10.1002/anie.201814416>.
- [235] P.M.J. Szell, D.L. Bryce, Solid-state nuclear magnetic resonance and nuclear quadrupole resonance as complementary tools to study quadrupolar nuclei in solids, *Concepts Magn. Reson. Part A* 45A (2016), e21412. <https://doi.org/10.1002/cmr.a.21412>.
- [236] J. Lužnik, J. Pirnat, V. Jazbinšek, Z. Lavrič, V. Žagar, S. Srčič, J. Seliger, Z. Trontelj,  $^{14}\text{N}$  nuclear quadrupole resonance study of polymorphism in famotidine, *J. Pharm. Sci.* 103 (2014) 2704–2709. <https://doi.org/10.1002/jps.23956>.
- [237] R.K. Harris, P.Y. Ghi, H. Puschmann, D.C. Apperley, U.J. Griesser, R.B. Hammond, C. Ma, K.J. Roberts, G.J. Pearce, J.R. Yates, C.J. Pickard, Structural studies of the polymorphs of carbamazepine, its dihydrate, and two solvates, *Org. Process Res. Dev.* 9 (2005) 902–910. <https://doi.org/10.1021/op0500990>.
- [238] R.K. Harris, P.Y. Ghi, H. Puschmann, D.C. Apperley, U.J. Griesser, R.B. Hammond, C. Ma, K.J. Roberts, G.J. Pearce, J.R. Yates, C.J. Pickard, Structural studies of the polymorphs of carbamazepine, its dihydrate, and two solvates, *Org. Process Res. Dev.* 10 (2006) 165. <https://doi.org/10.1021/op068000s>.
- [239] M.K. Dudek, P. Paluch, E. Pindelska, Crystal structures of two furazidin polymorphs revealed by a joint effort of crystal structure prediction and NMR crystallography, *Acta Crystallogr. Sect. B: Struct. Sci. Cryst. Eng. Mater.* B76 (2020) 322–335. <https://doi.org/10.1107/S205252062000373X>.
- [240] G.M. Day, W.D.S. Motherwell, W. Jones, A strategy for predicting the crystal structures of flexible molecules: the polymorphism of phenobarbital, *Phys. Chem. Chem. Phys.* 9 (2007) 1693–1704. <https://doi.org/10.1039/B612190J>.
- [241] G.M. Day, T.G. Cooper, Crystal packing predictions of the alpha-amino acids: methods assessment and structural observations, *CrystEngComm* 12 (2010) 2443–2453. <https://doi.org/10.1039/C002213F>.
- [242] R. Mathew, K.A. Uchman, L. Gkoura, C.J. Pickard, M. Baias, Identifying aspirin polymorphs from combined DFT-based crystal structure prediction and solid-state NMR, *Magn. Reson. Chem.* (2020) 1–8. <https://doi.org/10.1002/mrc.4987>.



- [243] J.P.M. Lommerse, W.D.S. Motherwell, H.L. Ammon, J.D. Dunitz, A. Gavezzotti, D.W.M. Hofmann, F.J.J. Leusen, W.T.M. Mooij, S.L. Price, B. Schweizer, M.U. Schmidt, B.P. van Eijck, P. Verwer, D.E. Williams, A test of crystal structure prediction of small organic molecules, *Acta Crystallogr. B* B56 (2000) 697–714. <https://doi.org/10.1107/S0108768100004584>.
- [244] W.D.S. Motherwell, H.L. Ammon, J.D. Dunitz, A. Dzyabchenko, P. Erk, A. Gavezzotti, D.W.M. Hofmann, F.J.J. Leusen, J.P.M. Lommerse, W.T.M. Mooij, S.L. Price, H. Scheraga, B. Schweizer, M.U. Schmidt, B.P. van Eijck, P. Verwer, D.E. Williams, Crystal structure prediction of small organic molecules: a second blind test, *Acta Crystallogr. B* B58 (2002) 647–661. <https://doi.org/10.1107/S0108768102005669>.
- [245] G.M. Day, W.D.S. Motherwell, H.L. Ammon, S.X.M. Boerrigter, R.G.D. Valle, E. Venuti, A. Dzyabchenko, J.D. Dunitz, B. Schweizer, B.P. van Eijck, P. Erk, J.C. Facelli, V.E. Bazterra, M.B. Ferraro, D.W.M. Hofmann, F.J.J. Leusen, C. Liang, C.C. Pantelides, P.G. Karamertzanis, S.L. Price, T.C. Lewis, H. Nowell, A. Torrisi, H.A. Scheraga, Y.A. Arnautova, M.U. Schmidt, P. Verwer, A third blind test of crystal structure prediction, *Acta Crystallogr. B* B61 (2005) 511–527. <https://doi.org/10.1107/S0108768105016563>.
- [246] G.M. Day, T.G. Cooper, A.J. Cruz-Cabeza, K.E. Hejczyk, H.L. Ammon, S.X.M. Boerrigter, J.S. Tan, R.G.D. Valle, E. Venuti, J. Jose, S.R. Gadre, G.R. Desiraju, T.S. Thakur, B.P. van Eijck, J.C. Facelli, V.E. Bazterra, M.B. Ferraro, D.W.M. Hofmann, M.A. Neumann, F.J.J. Leusen, J. Kendrick, S.L. Price, A.J. Misquitta, P.G. Karamertzanis, G.W.A. Welch, H.A. Scheraga, Y.A. Arnautova, M.U. Schmidt, J. van de Streek, A.K. Wolf, B. Schweizer, Significant progress in predicting the crystal structures of small organic molecules—a report on the fourth blind test, *Acta Crystallogr. B* B65 (2009) 107–125. <https://doi.org/10.1107/S0108768109004066>.
- [247] D.A. Bardwell, C.S. Adjiman, Y.A. Arnautova, E. Bartashevich, S.X.M. Boerrigter, D.E. Braun, A.J. Cruz-Cabeza, G.M. Day, R.G.D. Valle, G.R. Desiraju, B.P. van Eijck, J.C. Facelli, M.B. Ferraro, D. Grillo, M. Habgood, D.W.M. Hofmann, F. Hofmann, K.V.J. Jose, P.G. Karamertzanis, A.V. Kazantsev, J. Kendrick, L.N. Kuleshova, F.J.J. Leusen, A.V. Maleev, A.J. Misquitta, S. Mohamed, R.J. Needs, M.A. Neumann, D. Nikylov, A.M. Orendt, R. Pal, C.C. Pantelides, C.J. Pickard, L.S. Price, S.L. Price, H.A. Scheraga, J. van de Streek, T.S. Thakur, S. Tiwari, E. Venuti, I.K. Zhitkov, Towards crystal structure prediction of complex organic compounds—a report on the fifth blind test, *Acta Crystallogr. B* B67 (2011) 535–551. <https://doi.org/10.1107/S0108768111042868>.
- [248] A.M. Reilly, R.I. Cooper, C.S. Adjiman, S. Bhattacharya, A.D. Boese, J.G. Brandenburg, P.J. Bygrave, R. Bylsma, J.E. Campbell, R. Car, D.H. Case, R. Chadha, J.C. Cole, K. Cosburn, H.M. Cuppen, F. Curtis, G.M. Day, R.A. DiStasio Jr., A. Dzyabchenko, B.P. van Eijck, D.M. Elking, J.A. van den Ende, J.C. Facelli, M.B. Ferraro, L. Fusti-Molnar, C.-A. Gatsiou, T.S. Gee, R. de Gelder, L.M. Ghiringhelli, H. Goto, S. Grimme, R. Guo, D.W.M. Hofmann, J. Hoja, R.K. Hylton, L. Iuzzolino, W. Jankiewicz, D.T. de Jong, J. Kendrick, N.J.J. de Klerk, H.-Y. Ko, L.N. Kuleshova, X. Li, S. Lohani, F.J.J. Leusen, A.M. Lund, J. Lv, Y. Ma, N. Marom, A.E. Masunov, P. McCabe, D.P. McMahon, H. Meekes, M.P. Metz, A.J. Misquitta, S. Mohamed, B. Monserrat, R.J. Needs, M.A. Neumann, J. Nyman, S. Obata, H. Oberhofer, A.R. Oganov, A.M. Orendt, G.I. Pagola, C.C. Pantelides, C.J. Pickard, R. Podeszwa, L.S. Price, S.L. Price, A. Pulido, M.G. Read, K. Reuter, E. Schneider, C. Schober, G.P. Shields, P. Singh, I.J. Sugden, K. Szalewicz, C.R. Taylor, A. Tkatchenko, M.E. Tuckerman, F. Vacarro, M. Vasileiadis, A. Vazquez-Mayagoitia, L. Vogt, Y. Wang, R.E. Watson, G.A. de Wijs, J. Yang, Q. Zhu, C.R. Groom, Report on the sixth blind test of organic crystal structure

- prediction methods, *Acta Crystallogr. Sect. B: Struct. Sci. Cryst. Eng. Mater.* B72 (2016) 439–459. <https://doi.org/10.1107/S2052520616007447>.
- [249] J.K. Harper, D.M. Grant, Enhancing crystal-structure prediction with NMR tensor data, *Cryst. Growth Des.* 6 (2006) 2315–2321. <https://doi.org/10.1021/cg060244g>.
- [250] M.K. Dudek, A. Jeziorna, M.J. Potrzebowski, Computational and experimental study of reversible hydration/dehydration processes in molecular crystals of natural products—a case of catechin, *CrystEngComm* 18 (2016) 5267–5277. <https://doi.org/10.1039/C6CE00932H>.
- [251] M.K. Dudek, G. Bujacz, M.J. Potrzebowski, Experimental tests for quality validation of computationally predicted crystal structures—a case of a conformationally flexible procyanidin A-2 dihydrate, *CrystEngComm* 19 (2017) 2903–2913. <https://doi.org/10.1039/C7CE00618G>.
- [252] M. Baias, J.-N. Dumez, P.H. Svensson, S. Schantz, G.M. Day, L. Emsley, De Novo determination of the crystal structure of a large drug molecule by crystal structure prediction-based powder NMR crystallography, *J. Am. Chem. Soc.* 135 (2013) 17501–17507. <https://doi.org/10.1021/ja4088874>.
- [253] A. Hofstetter, M. Balodis, F.M. Paruzzo, C.M. Widdifield, G. Stevanato, A.C. Pinon, P.J. Bygrave, G.M. Day, L. Emsley, Rapid structure determination of molecular solids using chemical shifts directed by unambiguous prior constraints, *J. Am. Chem. Soc.* 141 (2019) 16624–16634. <https://doi.org/10.1021/jacs.9b03908>.
- [254] G. Mali, M.U.M. Patel, M. Mazaj, R. Dominko, Stable crystalline forms of Na polysulfides: experiment versus Ab initio computational prediction, *Chem. A Eur. J.* 22 (2016) 3355–3360. <https://doi.org/10.1002/chem.201504242>.
- [255] A.R. Oganov, C.W. Glass, Evolutionary crystal structure prediction as a tool in materials design, *J. Phys. Condens. Matter* 20 (2008), 064210. <https://doi.org/10.1088/0953-8984/20/6/064210>.
- [256] A.O. Lyakhov, A.R. Oganov, H.T. Stokes, Q. Zhu, New developments in evolutionary structure prediction algorithm USPEX, *Comput. Phys. Commun.* 184 (2013) 1172–1182. <https://doi.org/10.1016/j.cpc.2012.12.009>.
- [257] C.W. Glass, A.R. Oganov, N. Hansen, USPEX—evolutionary crystal structure prediction, *Comput. Phys. Commun.* 175 (2006) 713–720. <https://doi.org/10.1016/j.cpc.2006.07.020>.
- [258] G. Mali, Ab initio crystal structure prediction of magnesium (poly)sulfides and calculation of their NMR parameters, *Acta Crystallogr. Sect. C Struct. Chem.* C73 (2017) 229–233. <https://doi.org/10.1107/S2053229617000687>.
- [259] V.M. Morin, P.M.J. Szell, E. Caron-Poulin, B. Gabidullin, D.L. Bryce, Mechanochemical preparations of anion coordinated architectures based on 3-Iodoethynylpyridine and 3-Iodoethynylbenzoic acid, *ChemistryOpen* 8 (2019) 1328–1336. <https://doi.org/10.1002/open.201900194>.